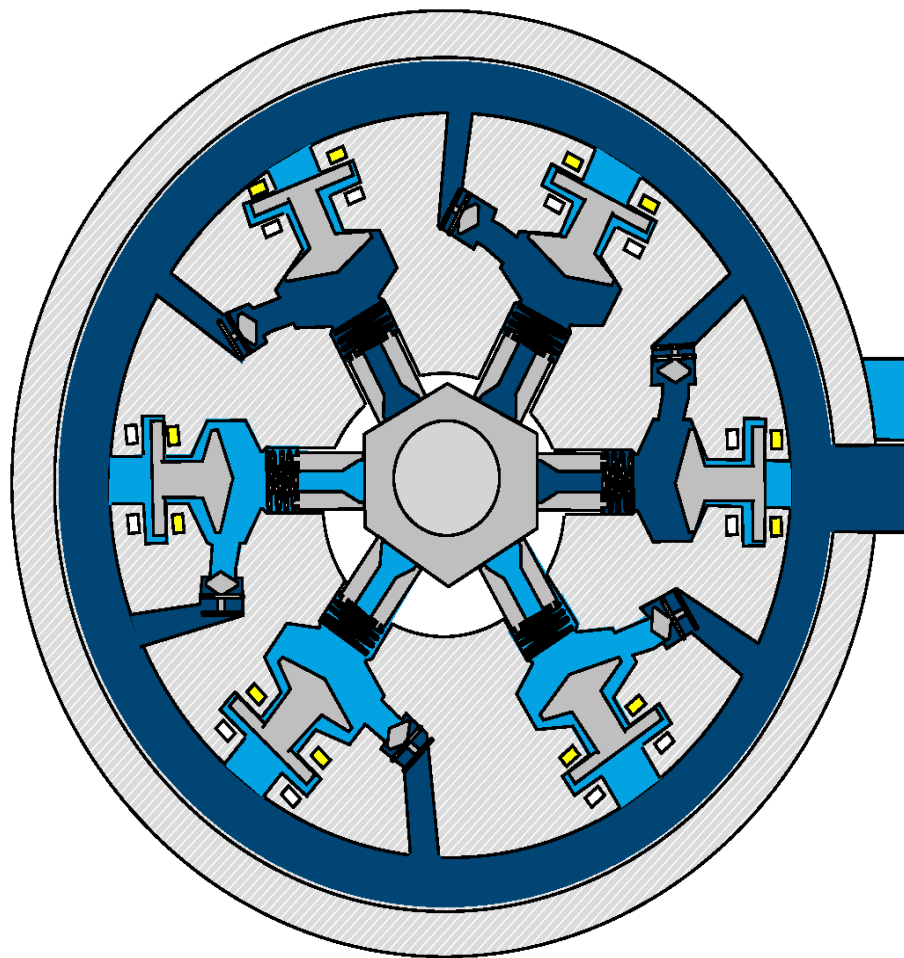


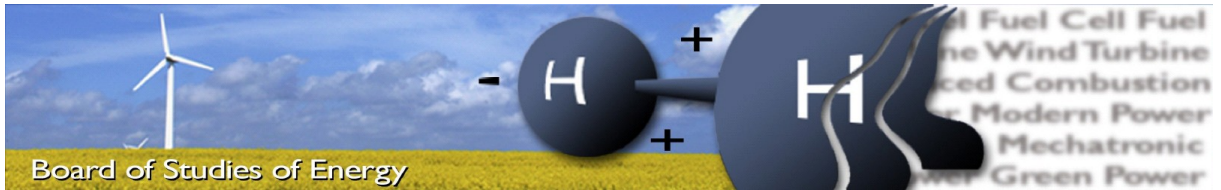
CONTROL OF A DIGITAL DISPLACEMENT PUMP



Cemre Yigen

Master Thesis
Spring 2012


AALBORG UNIVERSITET
Department of Energy Technology
Mechatronic Control Engineering



Title: Control of a Digital Displacement Pump
Semester: 10th
Semester Theme: Master Thesis
Project period: 01.02.12 to 31.05.12
ECTS: 30
Supervisors: Henrik Clemmensen Pedersen
Per Johansen
Project group: MCE4-1022

Cemre Yigen

Copies: 4
Pages, total: 82 pages
Appendix: 15 pages
Supplements: 1 CD

By signing this document, each member of the group confirms that all participated in the project work and thereby all members are collectively liable for the content of the report.

SYNOPSIS:

The purpose of this report has been to design a flow controller for a Digital Displacement Pump (DDP). To achieve this result, a nonlinear model of the pump has been developed and implemented in MATLAB Simulink. The nonlinear model has been validated by using measurement data from a source at Aalborg University. At the same time, the model has been analysed to identify the sensitivity of the pump's output flow for changing oil temperature. A flow filter and flow estimator has been developed in order to estimate the output flow from the pump and to obtain its average value. Furthermore, an Internal Model Controller has been designed utilising a Smith Predictor to account for the time-delayed DDP response. The proposed controller applied on the nonlinear model showed promising results. Polynomial regression is utilised to construct an input-output map based on the nonlinear model. Additionally, two methods have been proposed to adapt the map for changing oil temperatures; an offset method and a method based on convex optimisation. Both methods utilise the predicted error to adjust the polynomial coefficients and better results were achieved by using the optimisation method on the nonlinear DDP model.

Preface

This report is a documentation of a master project written by Cemre Yigen at Aalborg University to complete the Master of Science programme in Energy Engineering with specialization in Mechatronic Control Engineering. The project period spans from 1st of February 2012 till 31st of May 2012. Associate Professor Henrik Clemmensen Pedersen and PhD fellow Per Johansen has been supervising during the project period.

The Harvard method is used for literature references where the surname of the author and year of publication is enclosed in brackets, i.e. [Andersen, 2003]. Figures, tables and equation are numbered with two digits separated by a period, i.e. equation 2.1. The first digit refers to the chapter and the second digit refers to the number of the figure, table or equation. Appendix references are stated with letters.

SI-units are used throughout the report. Vectors are marked with arrows and matrices with underlines, i.e. \vec{v} and \underline{M} accordingly. The first order time derivative is denoted by a dot above the symbol \dot{x} , consequently the second order time derivative by two dots.

The attached DVD-ROM contains MATLAB scripts and SIMULINK models developed to support the report. A digital copy of the report and paper references are also included in the DVD.

Aalborg University, 2012

Cemre Yigen

Summary

This report deals with the control design of a Digital Displacement Pump (DDP) that is characterized by multiple cylinder outlets. This technology gives the possibility of controlling the output flow from the pump energy efficiently.

A comprehensive nonlinear model of the six cylindered DDP is built that predicts the dynamics of the pump. The model consists of a hydraulic and mechanical part. The hydraulic model includes temperature variational effect on the oil parameters that affects the performance of the pump. The mechanical part predicts the dynamic behaviour of the moving elements in the pump. The DDP model is verified using data collected from a prototype by an external source and the parameters are tuned accordingly.

The DDP model is intensively analysed to identify possible patterns and characteristics for control design purposes. The pump speed and the input signal to the pump is determined based on considering the energy efficiency and the output power of the pump. A time-delay analysis is carried out to determine the delay between an input signal and the resulting output flow. This information is used to build a simplified model of the DDP with the intention of applying linear control theory. The output-flow is examined as well in order to determine its characteristics and its sensitivity towards oil temperature changes.

A method to measure the output flow is proposed based on the output flow response from the DDP and the available transducers at the prototype. The intention of utilising a flow measurement device is to use it in a negative feedback loop for closed loop control design. The method consists of an output flow estimator and filter to obtain the average value of the output flow. The sensitivity of the flow estimator towards uncertain parameters are assessed in order to verify utility.

A simplified model of the nonlinear DDP model is completed using step response analysis. The model is deliberately made linear in order to apply linear control analysis. A control structure is proposed consisting of a Feedforward Gain, Feedback Controller and an Internal Model Controller that utilises a Smith Predictor. The Feedforward gain utilises a map between the input and the output of the DDP. The Smith Predictor accounts for the time-delay present in the DDP. The closed loop controller is build based on worst-case-scenario in order to make the control strategy stable for all operation points.

Possible methods of adapting the DDPs input/output-map is specified based on sparse sample considerations. Firstly, polynomial regression is utilised relating the output flow, load pressure and the input signal for a fixed oil temperature. When a deviation is observed between the map and the measurement, an offset of the map is executed. Finally, the map is formulated as a convex optimisation problem which is solved using a normalised steepest descent algorithm.

Contents

Preface	v
Summary	vii
Nomenclature	xi
1 Introduction	1
1.1 Background	1
1.2 Basics of the technology	3
1.3 State of the art control	4
1.4 Motivation	6
1.5 Problem Statement	6
1.6 Report Structure	7
2 Nonlinear Model of a Digital Displacement Pump	9
2.1 System overview	9
2.2 Theoretical background to model a hydraulic system	10
2.3 Hydraulic system model	12
2.4 Mechanical system model	19
2.5 Verification of DDP model	26
3 Analysis of the Digital Displacement Pump Model	33
3.1 Preliminaries	34
3.2 System input	34
3.3 Time delay	38
3.4 System output	41
4 Flow Measurement on a Digital Displacement Pump	45
4.1 System overview	45
4.2 Frequency spectrum	47

4.3	Flow estimator	49
4.4	Flow filter	51
5	Control of a Digital Displacement Pump	59
5.1	Method outline	59
5.2	Simplified DDP model	60
5.3	Controller Structure	64
5.4	Controller design	66
6	Mapping function	71
6.1	Polynomial regression	71
6.2	Adaptation of the mapping function	73
6.3	Comparison of adaptation methods	77
7	Conclusion	81
7.1	Future Work	82
	Appendix	83
A	Model Theories	83
A.1	Orifice Equation	83
A.2	Euler Lagrange Derivations	85
A.3	Fluid viscosity	88
A.4	Oil parameter variation	89
A.5	Optimal coefficients for the vogel equation	90
B	Filters and Controllers	91
B.1	Filters	91
B.2	Controllers	93
C	DDP Flow Response	95
C.1	Maximum flow rate	96
C.2	Simplified pump response	97
	Bibliography	99

Nomenclature

Term	Description	SI-unit
A	Area	$[m^2]$
B_D	Drag coefficient	$[\frac{N \cdot s^2}{m^2}]$
β	Effective bulk modulus of oil	$[Pa]$
C_D	Discharge coefficient	[.]
c	Correction coefficient	[.]
d_H	Hydraulic diameter	$[m]$
F	Force	$[N]$
f	Frequency	$[Hz]$
J	Moment of inertia	$[kg \cdot m^2]$
k	Spring stiffness	$[\frac{N}{m}]$
m	Mass	$[kg]$
M	Torque	$[N \cdot m]$
Q	Hydraulic flow rate	$[\frac{m^3}{s}]$
Re	Reynolds number	[.]
r	Radius	$[m]$
ρ	Density of the fluid	$[\frac{kg}{m^3}]$
T_{oil}	Oil temperature	$[^\circ C]$
\mathcal{T}	Kinetic energy	$[J]$
τ	Time constant	$[\frac{s}{rad}]$
θ	Angle	$[\frac{rad}{s}]$
μ	Dynamic viscosity of oil	$[\frac{kg}{m \cdot s}]$
V	Volume	$[m^3]$
\mathcal{V}	Potential energy	$[J]$
v	Fluid velocity	$[\frac{m}{s}]$
x	Position of valves/piston/nut	$[m]$

Introduction

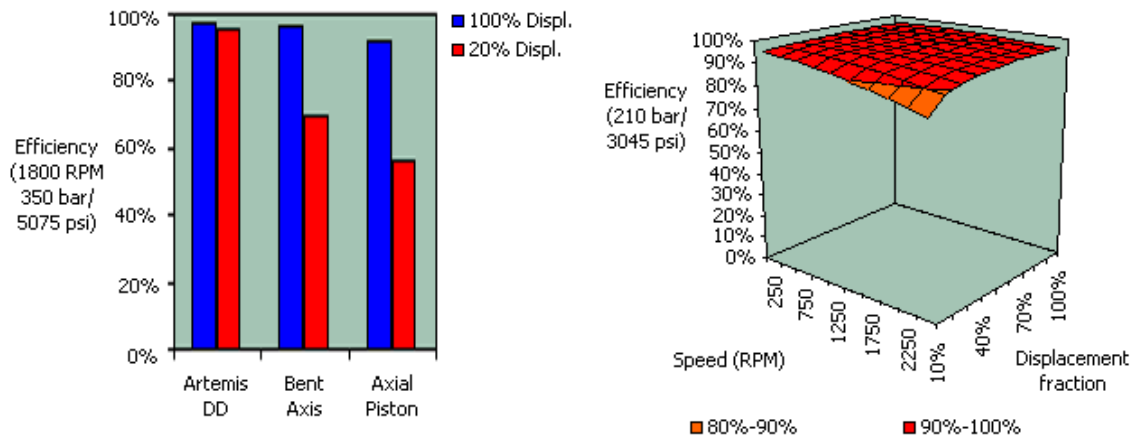
1

This chapter is intended to give the reader an introduction of a Digital Displacement Pump. Section 1.1 gives a background of the technology and explores application areas. In section 1.2, the working principles of the pump are introduced along with an overview of how its control mechanism works. Section 1.3 briefly introduces the current state of the pump's technology based on a review of the available literature. The motivation for working with this pump and identifying the areas of further improvement is discussed in section 1.4. A description of the problem covered in the report is described in section 1.5 together with the project goals and limitations. Finally, section 1.6 presents an overview of the chapters in the report.

1.1 Background

The Digital Displacement Pump (DDP) and Motor (DDM) was invented by Artemis Intelligent Power LTD. The company started as a derivative from a fluid-power and renewable energy research at University of Edinburg in 1994 with the intention of reducing power-losses in hydraulic transmission systems. The technology has exceptional controllability especially in synchronized applications and it also comes with high efficiency at part-load conditions.

The efficiency of the technology at full displacement is to some extent similar to the efficiency of a Bent Axis Pump and an Axial Piston Pump as seen in figure 1.1a. However, none of the other pump technologies can match the efficiency of a DDP at partial displacement. This is one of the key properties of the pump, which is also evident in figure 1.1b. The figure shows an almost uniform efficiency plot of an Artemis DDP obtained at 210[Bar] load pressure at various rotor speeds and displacement fractions.



(a) Artemis DDP efficiency comparison

(b) Artemis DDP efficiency at different operating points.

Figure 1.1: The efficiency of (a) an Artemis DDP compared to different pump technologies for two different displacement fractions and (b) an Artemis DDP for different operating points. [Artemis Intelligent Power LTD]

The company has identified a number of applications where a DDP or DDM can be beneficial. The technology has been and currently is being implemented to demonstrate the energy efficiency of the system compared to prevalent technology. The most well-known application is a Digital Displacement Hybrid Transmission system for automotive application where an hydraulic power transmission system is used to replace the gearbox of a vehicle. A conventional combustion engine that runs at maximum efficiency drives a DDP which is hydraulically coupled to a DDM. The DDM is directly connected to the wheels. The gear ratio between the motor and the pump can be chosen arbitrarily, and the change of gear-ratio is much faster than a normal gearbox. On top of this, the application can make use of regenerative braking energy by placing a hydraulic accumulator between the motor and the pump. The company demonstrated the effects of the technology on a BMW 530i in 2008 where up to 30% reduction of CO_2 emissions was obtained in a combination of city and highway driving. Another application that receives a lot of attention from the company is a Wind Turbine Transmission system for offshore wind turbines. A 7[MW] wind turbine prototype, SeaAngel, with 165[m] rotor diameter is currently under development which is expected to be ready in 2013. A hydraulic transmission system is used to decouple the rotor and the generator, thus making the gearbox redundant. The synchronous generator is driven in steady state by the DDM independently of the rotor speed. This makes the power converter surplus, which is the usual source of error for wind turbines. Since the gearbox and the power converter together are a considerable weight contribution for the nacelle, the requirements for load capacity of the tower is reduced NewScientist [2009]. This means that the total cost of the tower of such a wind turbine is lowered and also the need for maintenance is less frequent.

1.2 Basics of the technology

A Digital Displacement Pump is similar to an axial piston pump in functionality. Both are capable of adjusting the flow rate during a revolution. The axial piston pump uses a swash plate to adjust the stroke length. The DDP uses two on-off valves to adjust the flow rate because the DDP's stroke length is fixed. At least one of the on-off valves has to be active in order to work as a pump.

The use of on-off valves gives access to rapid change in flow rate on demand compared to a axial piston pump. Additionally, it expands the options for applying complex control strategies and also to support multiple applications by connecting each cylinder to a separate application.

The geometry of a DDP matches an *outside impinged radial piston pump*. The chamber of the cylinders are filled with fluid from the outside, hence the name *outside impinged*. Six cylinders are placed in a housing in radial direction around a rotational drive shaft colored yellow in figure 1.2. The number of cylinders depends on the application and chosen arbitrarily in this report. Artemis used 68 cylinders in a hydraulic transmission system prototype for wind turbines that was completed in 2009 [NewScientist, 2009].

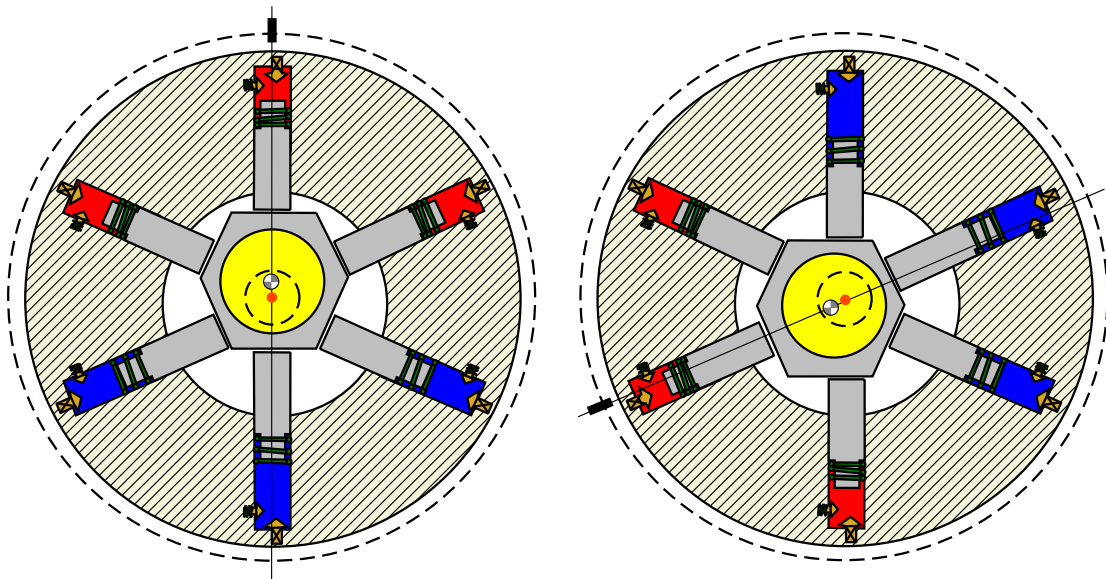


Figure 1.2: A Digital Displacement Pump with six cylinders with two different angles of the drive shaft.

Figure 1.2 is not an accurate drawing but it is used to illustrate the basics of the pump. It illustrates a counter clock wise rotation of the drive shaft and the distribution of pressure in the cylinder chambers at two different angles. A red color indicates high pressure and a blue color indicates low pressure. The angle of rotation is the difference between the black rectangles along the external dashed line. The hexagon shaped object is designed to have a cylindrical cavity that can fit an eccentric drive shaft. This means that there is a distance between the hexagons center of mass and the drive shafts rotation axis marked with an orange dot. As the shaft rotates inside the cavity, the hexagonal object is pushed in a non-rotational manner reaching every cylinder port during a revolution. The hexagon's

center of mass follows the dashed line inside in the yellow area.

The piston inside the cylinders is supported by the face of the hexagon. For one complete revolution, the piston makes a full stroke reaching the Top Dead Center (TDC) and the Bottom Dead Center (BDC). The volume of the cylinder chamber decreases if the piston is moving upward (BDC→TDC) which causes the enclosed fluid in the cylinder to pressurise and vice versa.

Throughout the report, the chambers in which the fluid is pressurised/depressurised are referred to as *the working chambers*. That is analogous to the combustion chamber of a gasoline engine where burned fuel pressurises the fluid.

The displacement from the working chamber is controlled by two valves; a high pressure (HP) valve and a low pressure (LP) valve. The LP valve is a solenoid valve that is used to control the fluid intake from the reservoir to the working chamber. The HP valve connects the load with the working chamber. It can either be chosen as a passive poppet valve that opens for discharge when the pressure difference tilts in favour of the working chamber or an active solenoid valve that makes it possible to control the time of discharge. Control strategy of a DDP deals with the switching of the solenoid valves.

A prototype of a single-cylinder DDP was developed by Johansen and Rømer [2011] at Aalborg University. The prototype contains an active solenoid LP valve and a passive HP poppet valve. This prototype will serve as the basis of this report where the number of cylinders is expanded to six.

1.3 State of the art control

Even though the technology was invented more than 15 years ago by Artemis Intelligent Power LTD, limited independent research about development and control of a DDP has been published. A review of the available literature is conducted below.

Ehsan et al. [2000] proposes a decision making algorithm to either enable or disable a cylinder for full displacement as a piston reaches its discharge stroke period BDC→TDC. A disabling decision leaves the LP valve open so fluid can enter and leave the cylinder as the piston moves up and down. Time delay is identified as a natural part of a DDP, thus a made decision is executed after a given time period. A look-ahead angle is defined which is used to predict the projected flow in the time interval between the decision-making instant and the look-ahead time. An open-loop pressure controller and a closed-loop flow controller are proposed which uses negative feedback to suppress low frequency resonance. The controllers make a decision based on the predicted displacement from already committed cylinders and the predicted load displacement. A third decision algorithm is proposed in the article which is based on a look-up table that contains sequence of decisions that matches a given output requirement, e.g. a series of specific decision would give approximately 10[L/min] load flow and 200[Bar] load pressure on average.

Armstrong and Yuan [2006] research is based on a seven chamber Gerotor in motoring mode which is somewhat similar to a DDM. As an eccentric rotor rotates the volumes of some chambers are either

increasing or decreasing. A function is given in the article that describes the rate of change of each chamber volume as the rotor rotates. The total instantaneous torque contribution to the rotor can be predicted based on the change of volume and the pressure inside the chambers. At a given rotor angle 2^7 different torque configurations exist for the gerotor, e.g. five cylinders could be connected to the supply pressure while the remaining two to the reservoir. A multi level control strategy is proposed that makes a decision based on all possible configurations of the seven chambers to obtain a desired instantaneous torque output from the motor. The control strategy uses a look-up table that gives a chamber-configuration based on a desired output torque and the current rotor angle. Since multiple configurations may give approximately the same torque levels, a torque configuration is selected that changes as little as possible during a time-step.

Heikkilä et al. [2010] shows experimental results conducted on a prototype consisting of 6 cylinders with active HP and LP valves. Due to the radial displacement around a shaft, a pair of 3 cylinders are in opposite phase. They define six decision instants and for the pair of cylinders in question one is chosen to be in pumping mode and the other in suction mode. The authors identify the possibility for having multiple outlets connected to the pump, e.g. one outlet for each cylinder. Their control strategy consists of an upper and lower threshold region around the reference load pressure. When the pressure exceeds the upper limit the cylinder in question is operated in suction mode and vice versa. Additionally, the switching time of the valves are controlled that accounts for compression time and valve delays.

Johansen and Rømer [2011] proposes two flow controllers and two pressure controllers. All controllers utilise a model based linearisation that accounts for changes in load pressure. A decision making trigger is fired as the pistons are about to enter the discharge stroke period where it is decided if the cylinder should pump or idle. Among the flow controllers, there is a Direct Cylinder Displacement (DCD) controller and a Delta Sigma Modulated Flow (DSMF) controller of which both are open-loop. The DCD controller is a partial displacement control strategy that divides the desired output flow evenly to all cylinders. The DSMF controller makes use of either full displacement operation or idle operation as the decision trigger is fired to approximate the desired output flow. The two pressure controllers are a PID pressure controller and a Volume Error Pressure (VEP) controller. The PID pressure controller uses linear control theory to apply a PID controller, as the name suggests, on a strongly simplified linear model with load pressure feedback. The VEP controller adds a partial displacement functionality to the strategy proposed in Ehsan et al. [2000] that makes use of a look-ahead time. The decision making is based on several estimations; the predicted load displacement, the displacement needed for compressing the fluid and the predicted displacement from already committed cylinders during the look-ahead time.

The common denominator for all the available publications is the use of control schemes that lose their accuracies as the oil changes its characteristic. Johansen and Rømer [2011] accounts for the changes in load pressure by applying a model based linearisation. Since the characteristic of oil is highly dependent on not only the pressure but also the temperature and the amount of free air en-

closed in the oil, an initiative is necessary to prevent loss in performance during operation.

1.4 Motivation

The scope of this report is to develop control schemes that accounts for changes in oil properties during operation. The operation conditions greatly affects the pressurising/depressurising time and the LP valve's open/close time as identified by Heikkilä et al. [2010] and Johansen and Rømer [2011]. This means that the output flow is different at different operation conditions even if the LP valves receive the same close-signal. Figure 1.3 shows an illustration of the actual displacement that takes place after the LP valve receives a close-signal.

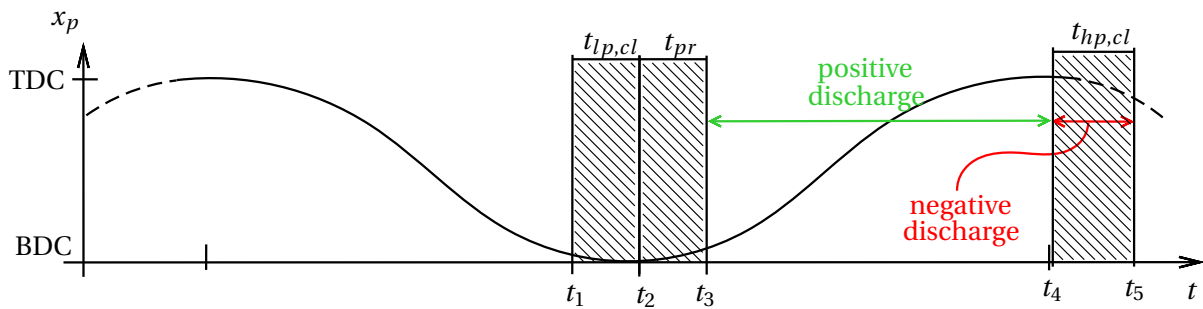


Figure 1.3: Conditions that has an impact on the actual displacement received at the load from a single cylinder.

The piston position x_p inside a cylinder is plotted for a full period (TDC→BDC→TDC). The LP valve receives a close signal at t_1 and some time $t_{lp,cl}$ elapse before the valve actually closes (t_2). At the next step, the pressure starts to build up as the piston moves from bottom to top. The pressurising delay is defined as t_{pr} . The HP valve opens for discharge at t_3 when the working chamber pressure exceeds the level of the load pressure. From t_3 till t_4 , a positive discharge takes place. The direction of the flow reverses causing back flow after t_4 because the pressure level falls below the load pressure level. The back flow continues until the pressure difference is sufficient to close the valve (t_5). This time period where negative discharge is present is labelled $t_{hp,cl}$. The actual displacement from the cylinders to the load is the difference between the positive and negative discharge.

The identified time delays have to be known by great accuracy, to precisely attain a desired displacement from the cylinders. This is not an easy task since all the delays are nonlinearly dependent on the properties of the oil. The pressurising t_{pr} delay varies for one thing with the load pressure level and the valve delays $t_{lp,cl}$, $t_{hp,cl}$ is for one thing affected by the viscosity of the oil.

1.5 Problem Statement

An accurate system model and good knowledge of parameter variation is needed in order to ensure precise displacement from the DDP. Fluid mechanics is by nature a highly nonlinear discipline that

entails a number of simplified models that are only valid when certain conditions are obeyed. As a consequence of this, modelling errors are impossible to avoid in practice.

The intention of the research conducted in the project period covered by the report is to explore areas where significant development lacks with regards to the Digital Displacement Pump. With this in mind, the report tries to answer the following main question.

How can the output flow of a Digital Displacement Pump be controlled regardless of the oil temperature and load pressure.

The output flow should be able to vary between 0% output and 100% output with arbitrary precision. 100% output flow refers to the maximum flow capability of the DDP. Also, the steady state error of the output flow should be less than 5% deviation.

The changes in operation condition refer to the load pressure and the oil temperature. In most applications, the load pressure changes rapidly while the oil temperature changes slowly.

As a consequence of this, the controller should compensate for the variation in load pressure within seconds. Additionally, the controller should tune its parameters during operation to the temperature of the oil. The convergence rate of the tuning process should be conducted within a minutes in order to yield satisfactory results.

The DDP should be able to deliver a relatively high power output as energy efficiently as possible.

The flow controller should produce as small flow ripples as possible. For this reason, the project is delimited to only consider partial displacement control strategies as this gives less flow ripples compared to a full displacement controls strategy.

The controller can directly be applied to many applications when the above mentioned requirements are fulfilled. This will guarantee the stability and approximately streamline the performance of the pump regardless of the operation condition.

1.6 Report Structure

The report consists of three chapters. These are *Nonlinear Model of Digital Displacement Pump*, *Analysis of the Digital Displacement Pump Model*, *Flow Measurement on a Digital Displacement Pump* and *Control of a Digital Displacement Pump*. Additional information supporting the chapters are attached in the *Appendix*.

In *Nonlinear Model of Digital Displacement Pump* the objective is to develop a model of the Digital Displacement Pump that will serve as a testing unit. The model is going to be validated throughout measurement data obtained from a prototype.

In *Analysis of the Digital Displacement Pump Model* the model is extensively analysed in order to determine the input signals to the pump, the time delays of the pump and the output flow from the pump. The most efficient operation mode of the DDP with high output power is going to be de-

terminated. The time delays in the system are going to be identified in order to help control design. Additionally, a study of the output flow will be conducted in order to classify methods to perform flow measurement.

Once the analysis is carried out, the design of a flow measurement device will be initiated. Through a flow filter and flow estimator, the average output flow will be obtained. A sensitivity test is going to be performed on the designed flow filter and estimator to verify its usability on the DDP.

This is followed by an initiation of control schemes research that takes advantage of the Nonlinear model in *Control of a Digital Displacement Pump*. As a consequence of the limited time frame of the project, a test of the control scheme on the prototype will not be conducted. The controller is only tested on the Nonlinear Model and evaluated based on these results.

Finally, the design of a map will be carried out in *Mapping Function* to identify the DDP's input-output map. Moreover, methods to adapt the mapping function will be explored and tested on the nonlinear model together with the designed controller.

Nonlinear Model of a Digital Displacement Pump

This chapter describes a model of the Digital Displacement Pump and a model of a simple load. Firstly, a system overview is given in this section. A brief summary of the used theories is introduced to model the hydraulic system. This is followed by a derivation of a mechanical system model. Finally, the model is verified using data obtained from a prototype at Aalborg University.

2.1 System overview

The system contains six single acting hydraulic cylinders where inflow and outflow is controlled by on/off valves. The LP valve is a 2/2 way directional valve with electric actuation connecting the working chambers to the reservoir. The HP valve is a pressure relief valve connecting the working chambers to a pressure node P_{load} . The position of the pistons are determined by an eccentric drive shaft. The load is a restrictor with an adjustable orifice. A hydraulic schematic of the system is given in figure 2.1 using standardized symbols that follows DIN ISO 1219 [Andersen and Hansen, 2007, Chap.1].

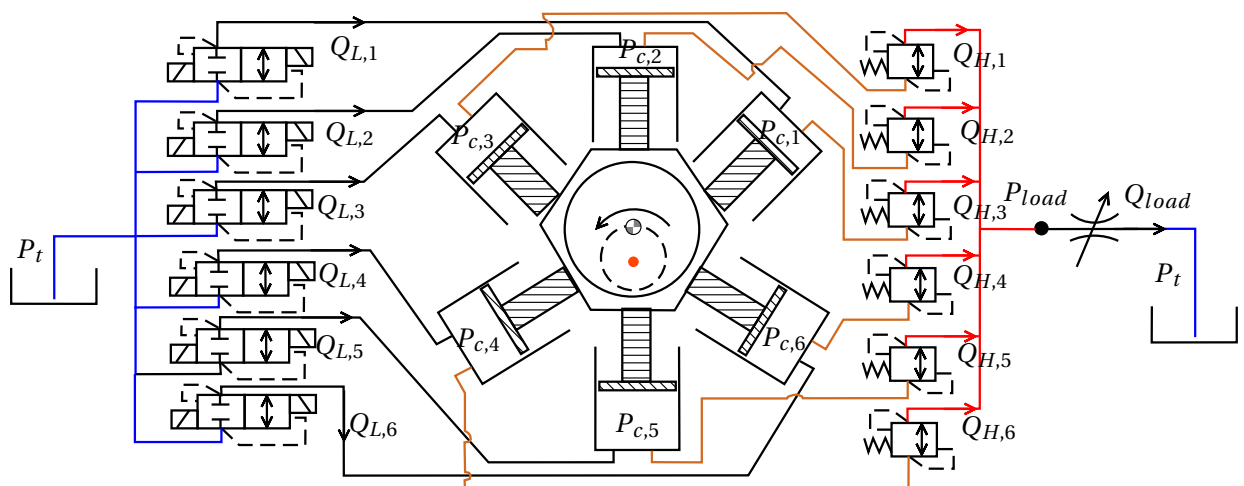


Figure 2.1: The hydraulic circuit of the DDP pump and the load using standardized symbols.

A thorough examination of the hydraulic components presented in the hydraulic circuit diagram is carried out in the following sections.

2.2 Theoretical background to model a hydraulic system

The valve openings are modelled as an annular orifice with a sharp edge that makes a sudden reduction in the flow path. Moreover, the annular orifice has a constant cross-sectional area.

Applying conservation of mass and Bernoulli's equation on a streamlined and steady fluid flow, where the fluid is incompressible and inviscid, results in the orifice equation. See appendix A.1 for derivations. The orifice equation that accounts for frictional losses is given in equation 2.1.

$$Q = C_d A_0 \sqrt{\frac{2}{\rho} (P_1 - P_2)} \quad (2.1)$$

where

Q	Flow through orifice	$[m^3/s]$
C_d	Discharge coefficient	$[.]$
A_0	Area of orifice	$[m^2]$
$P_1 - P_2$	Pressure drop from upstream to downstream	$[Pa]$

The model is not valid for low Reynold numbers Re , typically for $\sqrt{Re} < 10$. Nevertheless, it is often used under this condition by defining the discharge coefficient C_d as a function of Re [Andersen, 2003, Chap.1]. The coherence between Re and C_d entails three parts; (1) a linear relation in the laminar region, (2) a peak in the transitional region and (3) a saturation in the turbulent region. Lack of comprehensive measurement data is often the reason why the transitional region is neglected in the models. Therefore, a piecewise linear function is used to model part (1) and (3).

$$C_d = \begin{cases} \frac{C_{d,max}}{\sqrt{Re_t}} \sqrt{Re} & \text{if } 0 \leq Re \leq Re_t \\ C_{d,max} & \text{if } Re > Re_t \end{cases} \quad (2.2)$$

where

$C_{d,max}$	Saturated discharge coefficient for turbulent flow	$[.]$
Re_t	Reynolds number for transition region	$[.]$
Re	Actual Reynolds number	$[.]$

The Reynolds number is a dimensionless number that describes the ratio between the inertial forces to the and viscous forces applied on a fluid. A large number indicates large inertial forces that results in turbulent flow while a low number results in laminar flow. The Re is calculated based on the hydraulic diameter d_H of the restrictor, the density of the fluid ρ , the velocity of the fluid v and the dynamic viscosity of the fluid μ . The relations is given by $Re = \frac{\rho v d_H}{\mu}$. The mean velocity of the fluid v

relative to the orifice wall can be computed as the ratio of the flow Q and the discharge area A_0 by using the principle of continuity. This creates a conflict because Re is used to calculate the flow and the flow is used to calculate Re . To avoid this, a time-delay is introduced so that Re for the current time step k is calculated based on the flow calculations from the previous time step $k - 1$. The accuracy of this method depends on the sampling time and in general a high sampling time gives better results. The Reynolds number for the flow through an orifice is modelled as in equation 2.3.

$$Re[k] = \frac{\rho d_h |Q[k-1]|}{\mu A_0} \quad (2.3)$$

where

ρ	Density of the fluid	$[kg/m^3]$
d_H	Hydraulic diameter of the orifice	$[m]$
μ	Dynamic viscosity of the fluid	$[Ns/m^2]$

In a system with movable parts leakage is inevitable. Fittings between a piston and its housing is deliberately made with a small gap to minimise friction and wear as a result of a film of lubricating oil. In reality, the lubricating oil is leakage flow in the gap. The gap has an annular shape and therefore the leakage is modelled as laminar flow through an annular, see equation 2.4. This model is derived from the Navier-Stokes equations with the assumption that a steady, axisymmetric, incompressible and laminar flow is parallel to the wall [Munson et al., 2010, p.315-317].

$$Q_{annulus} = \frac{\pi \Delta P}{8 \mu L} \left[r_o^4 - r_i^4 - \frac{(r_o^2 - r_i^2)^2}{\ln\left(\frac{r_o}{r_i}\right)} \right] \quad (2.4)$$

where

Q_{leak}	Leakage fluid flow	$[m^3/s]$
ΔP	Pressure difference across leakage path	$[Pa]$
r_i	Annulus inner circle diameter	$[m]$
r_o	Annulus outer circle diameter	$[m]$
L	Length of leakage path	$[m]$

The pressure inside the working chamber is affected by several factors: the flow in and out of the chamber, the volume of the chamber and the stiffness of the fluid. The pressure is modelled by utilising the continuity equation [Andersen, 2003]. It is based on the principle of conservation of mass, the effective tangent bulk modulus of the fluid and the average density of the fluid entering and leaving the control volume [Andersen, 2003, Chap.3].

$$Q_{in} - Q_{out} = \frac{dV}{dt} + \frac{V}{\beta} \frac{dP}{dt} \quad (2.5)$$

where

Q	The inlet and outlet fluid flow to the chamber	$[m^3/s]$
V	Volume of the work chamber	$[m^3]$
P	Pressure of the work chamber	$[Pa]$
β	Stiffness of fluid	$[Pa]$

2.3 Hydraulic system model

The model of the hydraulic system is separated into three parts. The first part explores how the characteristics of the hydraulic fluid changes mainly as a function of oil temperature and oil pressure. The next part deals with a hydraulic model of the DDPs working chamber, i.e. flow equations and pressure gradients. Lastly, a model of a simple load is given to function as a framework where control strategies, developed in chapter 5, can be tested.

2.3.1 Hydraulic fluid

Oil is used as the hydraulic fluid in the DDP. The oil parameters are highly sensitive towards changes in oil temperature and oil pressure. The parameters that describes the characteristics of the oil is the dynamic viscosity of the oil μ , the effective bulk modulus of the oil β and the density of the oil ρ . When these oil parameters changes as a result of for instance a higher temperature, the performance of the DDP alters. As a result, the variation in the oil parameters can be designated as a disturbance to the model. In order to account for these disturbances in the control design, it is important have a model that predicts the variation in the oils parameters.

Oil density

A mineral oil that comply with the ISO VG 46 standard, with the brand name Shell Tello 46, is used in the hydraulic system. The mineral oil base is assumed to be categorised as a HM type, because it is the most common mineral-oil-based hydraulic fluid [Gilani]. The density of this oil is calculated using the Dow and Fink equation given in equation 2.7.

$$\rho(T, P) = \rho_0(T) (1 + A_\beta(T) \cdot P - B_\beta(T) \cdot P^2) \quad (2.6)$$

where

T	Oil temperature	$[^\circ C]$
P	Oil pressure	$[Pa]$
α_t	Thermal expansion coefficient $\alpha_t = 0.007$	$[1/^\circ C]$
$\rho_0(T)$	Density at atmospheric pressure for given temperature T	$[kg/m^3]$
A_β	The Dow and Fink temperature coefficient	$[1/Pa]$
B_β	The Dow and Fink temperature coefficient	$[1/Pa^2]$

This is an empirical model that predicts the density for any temperature and pressure as long as the oil density at atmospheric pressure ρ_0 and a thermal expansion coefficient $\alpha_t \in [0.0065 : 0.007]$ is known. The thermal expansion coefficient is independent on oil temperature and pressure. The coefficients

to the Dow and Fink equation is calculated based on equation 2.8-2.10 where ρ_0 is a function of a reference density defined at 15°C and atmospheric pressure [Andersen, 2003, Chap.2]. The reference density for the Shell Tello 46 oil is defined at 15°C as $\rho_{15} = 879[kg/m^3]$ [Shell, 2008].

$$\rho(T, P) = \rho_0(T) (1 + A_\beta(T) \cdot P - B_\beta(T) \cdot P^2) \quad (2.7)$$

$$\rho_0(T) = \frac{\rho_{15}}{1 + \alpha_t \cdot (T - 15)} \quad (2.8)$$

$$A_\beta(T) = (-6.72 \cdot 10^{-4} \cdot T^2 + 0.53 \cdot T - 36.02) \cdot 10^{-11} \quad (2.9)$$

$$B_\beta(T) = (2.82 \cdot 10^{-4} \cdot T^2 - 0.24 \cdot T + 57.17) \cdot 10^{-19} \quad (2.10)$$

Oil viscosity

The dynamic viscosity of the mineral oil μ describes the resistance of the fluid towards laminar motion. It is calculated based on the Vogel equation at atmospheric pressure levels for a specific temperature, see equation 2.11.

$$\mu_0(T) = K_{vo,a} \cdot exp\left(\frac{K_{vo,b}}{(T + 273.15) - K_{vo,c}}\right) \quad (2.11)$$

where

$K_{vo,a}$	Dynamic viscosity constant $K_{vo,a} = 0.000020096463$	$[kg/(m \cdot s)]$
$K_{vo,b}$	Absolute temperature constant $K_{vo,b} = 1050.325917381536$	$[K]$
$K_{vo,c}$	Absolute temperature constant $K_{vo,c} = 172.732548744080$	$[K]$

According to Knezevic and Savic [2006] this is the most accurate model of the oil viscosity among three other models; Reynolds Equation, Slotte Equation and Walther Equation. The coefficients $K_{vo,a}, K_{vo,b}$ and $K_{vo,c}$ is obtained based on a data from a viscosity-temperature plot given in appendix A.3. Based on readings from the plot, a convex optimisation problem is defined in order to obtain the optimal coefficients of equation 2.11. The problem is solved using the simplex method in appendix A.5.

The viscosity-pressure relation is given by the Barus Equation, see equation 2.12. It uses a coefficient α which is stated in equation 2.13. This coefficient is based on the Modulus Equation and its coefficients has to be obtained from measurements. In Knezevic and Savic [2006], these coefficients are computed for an oil that complies with the ISO VG 46 standard.

$$\mu(T, P) = \mu_0(T) \cdot e^{\alpha(T,P) \cdot P} \quad (2.12)$$

$$\alpha(T, P) = (K_{pv,a1} + K_{pv,a2} \cdot T + (K_{pv,b1} + K_{pv,b2} \cdot T) P)^{-1} \quad (2.13)$$

where

$\alpha(P, T)$	Pressure viscosity coefficient for any temperature and pressure	[Pa]
$K_{pv,a1}$	$= 334 \cdot 10^5$	[Pa]
$K_{pv,a2}$	$= 3.2557 \cdot 10^5$	[Pa/°C]
$K_{pv,b1}$	$= 0.026266$	[.]
$K_{pv,b2}$	$= 0.000315$	[1/°C]

Oil stiffness

The free air in hydraulic system influences the stiffness of the oil strongly, since air is much more compressible than fluid. Therefore, it is important to accurately determine the amount of free air in the system. This is not an easy task because the amount of air that can be dissolved in the oil changes with the pressure. Henry-Dalton's Law describes this phenomena in steady state conditions. Due to pressure fluctuations in the working chambers caused by the pitons moving up and down, steady state conditions are never fulfilled. As a consequence of this, the Henry Dalton's law cannot be applied to the DDP. Instead, it is assumed that the air molecules does not dissolve in the oil, hence there is the same amount of free air molecules in the oil. A reference volumetric ratio of free air $\epsilon_{A,0}$ is estimated at atmospheric pressure levels from measurement data. The volume of the air changes as a function of the pressure when adiabatic conditions are assumed. This causes the volumetric ratio of free air to change as well. Using the above statements, the volumetric ratio of free air can be determined by equation 2.14 [Andersen, 2003, Chap.2].

$$\epsilon_A(P) = \frac{1.0}{\left(\frac{1.0 - \epsilon_{A,0}}{\epsilon_{A,0}}\right) \left(\frac{P_{atm}}{P}\right)^{-1/c_{ad}} + 1.0} \quad (2.14)$$

where

$\epsilon_{A,0}$	Volumetric ratio of free air in the oil at atmospheric pressure, $\epsilon_{A,0} = 0.005$	[.]
P_{atm}	Atmospheric pressure, $P_{atm} = 1 [Bar]$	[Pa]
P	Absolute chamber pressure	[Pa]

The effective oil stiffness given in equation 2.15 is a function of both the oil stiffness β_{oil} and the stiffness of the free air β_{air} . It is upper saturated at $\beta = 10000 [Bar]$ per recommendation because the effective stiffness of the oil is not measured [Andersen, 2003].

$$\beta(T, P) = \frac{1}{\frac{1}{\beta_{oil}(T, P)} + \epsilon_A(P) \left(\frac{1}{\beta_{air}(P)} - \frac{1}{\beta_{oil}(T, P)} \right)} \quad (2.15)$$

The stiffness of the oil is derived based on the oil density given in equation 2.7 and the definition of the tangential bulk modulus $\beta = \rho \frac{dP}{d\rho}$ [Andersen, 2003, Ch.2]. As a result, the stiffness of the oil can be estimated for any temperature and pressure, see equation 2.16. The stiffness of the air is calculated based on equation 2.17.

$$\beta_{oil}(T, P) = \frac{1.0 + A_\beta(T) \cdot P - B_\beta(T) \cdot P^2}{A_\beta(T) - 2 \cdot B_\beta(T) \cdot P} \quad (2.16)$$

$$\beta_{air}(P) = c_{ad} \cdot P_a \quad (2.17)$$

where

P_a Absolute pressure in a chamber [Pa]
 c_{ad} Adiabatic constant of air $c_{ad} = 1.4$ [.]

2.3.2 Working chamber model

The hydraulic model of the working chamber consists of a pressure node and three flow equations. The pressure node is influenced by the movement of the piston and the flows in/out of the chamber. The pistons are constantly moving up and down, which means that the piston is constantly affecting the pressure. As a consequence of this, first the pressure inside the working chambers is described together with an analysis of the kinematics of piston. This is followed by a description of the in and out flows to the working chamber.

Pressure in working chambers

The pressure gradient of the working chambers fluid is given by solving the continuity equation, see equation 2.18.

$$\dot{P}_{c,i} = \frac{\beta}{V_0 - A_p x_{p,i}} (Q_{L,i} - Q_{H,i} - Q_{leak,i} + A_p \dot{x}_{p,i}) \quad (2.18)$$

where

V_0 Working chamber dead volume at BDC, $V_0 = 0.5[L/min]$ [m^3]

The pressure gradient first of all depends on whether the cylinder is in enable or idle mode as this effects the in/out flow to the working chamber. A simplified schematic of the hydraulic circuit is shown in figure 2.2.c where cylinder 1, 2 and 6 are within their discharge stroke period. Their respective LP valves has received a close signal so that the entrapped fluid inside the working chambers becomes pressurised by the movement of the pistons.

The six spring-loaded pistons are forced towards each face of the hexagonal nut. This means that the pistons are radially displacement by 60° . Each pistons position $x_{p,i}$ can be described as a function of the shaft angle θ_{pump} when the pistons and the hexagon is assumed to be a single rigid body. Figure 2.2.a illustrates a stripped view of how the position of the pistons relates to the hexagons center of mass. From this figure, one can see why the pistons in figure 2.2.c are displaced as illustrated.

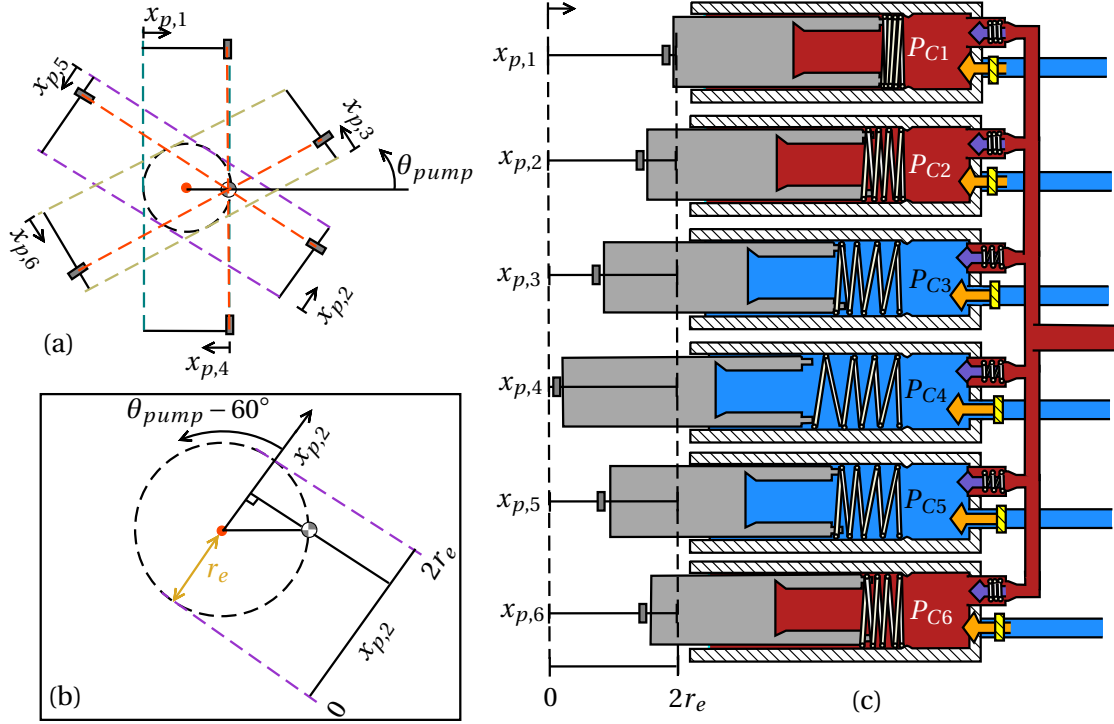


Figure 2.2: Simplified schematic of a DDP where (c) illustrates how the position of each piston is shifted at a snapshot, (b) the trigonometry that relates piston position with pump shaft angle and (a) how the position of all the pistons relates to the position of the hexagon

Using trigonometry, the position of each piston can be derived. In figure 2.2.b, piston 2 is taken as a reference. The position of piston 2 is shifted by 60° because θ_{pump} is defined with respect to TDC of piston 1. Notice, when $\theta_{pump} = 60^\circ$, piston 2 reaches its TDC. The inserted right triangle in figure 2.2 can be utilised to describe the position of piston 2 as a function of θ_{pump} . The hypotenuse is the eccentric distance r_e between the shafts center, marked by a red circle, and the hexagons center of mass. The distance a piston can travel is equivalent to the diameter of eccentricity, i.e. $2 \cdot r_e$. This means that by defining BDC at $x_{p,2} = 0$ TDC is reached at $x_{p,2} = 2 \cdot r_e$.

Above analysis shows that the position of the piston can be described using an offset of r_e and a cosine function that maps a shaft angle θ_{pump} into $\mathcal{R} \in [-r_e : r_e]$. This relation is given in equation 2.19. The velocity of the piston can be determined by taking the time-derivative of $x_{p,i}$, see equation 2.20.

$$x_{p,i} = r_e \cdot \cos\left(\theta_{pump} - \frac{(i-1)\pi}{3}\right) + r_e \quad (2.19)$$

$$\dot{x}_{p,i} = -r_e \cdot \sin\left(\theta_{pump} - \frac{(i-1)\pi}{3}\right) \dot{\theta}_{pump} \quad (2.20)$$

- i The piston number $i \in \{1, 2, 3, 4, 5, 6\}$ [.]
- r_e Radius of eccentric, $r_e = 3.75[m]$ [m]

Now, that the kinematics of the pistons are described the other variables that affects the pressure gradient can be explored.

Flow in and out of the working chamber

An illustration of *working chamber 1* is shown in figure 2.3.

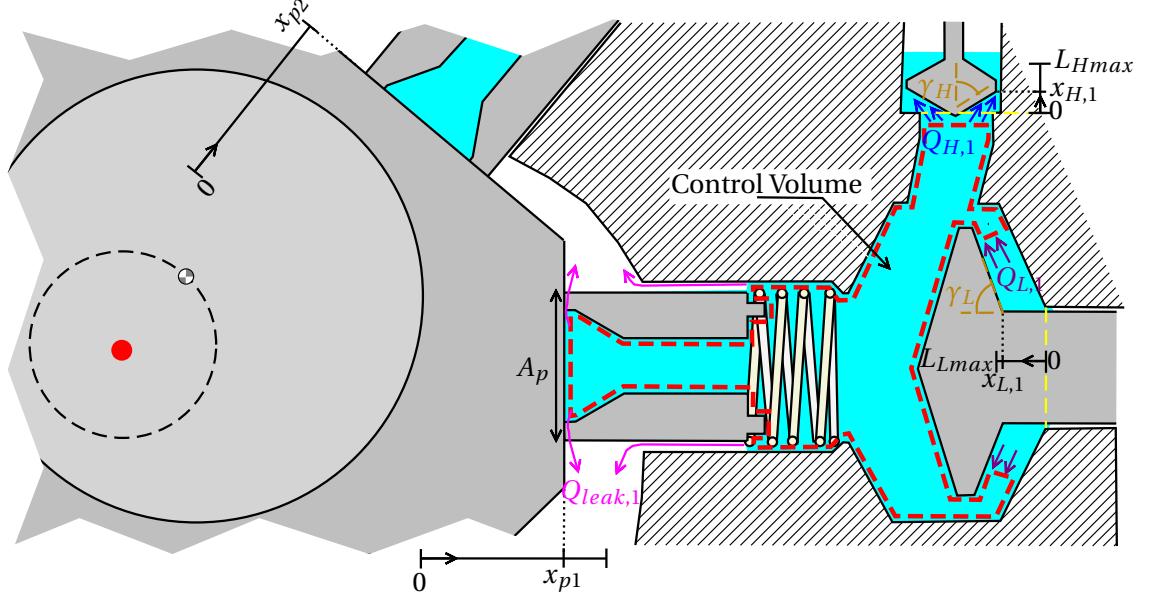


Figure 2.3: The control volume of a working chamber from a cylinder mounted radially around an eccentric shaft.

The control volume of the chamber is marked by a dashed red line. The size of the volume changes according to the position of the piston $x_{p,1}$. In this snapshot, piston 1 has just passed TDC and it is moving towards BDC. This is defined as the intake-stroke. The flow into working chamber 1 comes from the reservoir through the LP valve ($Q_{L,1}$). The flow out of the chamber goes through the high pressure valve to the load ($Q_{H,1}$). The flow equations are given in equation 2.21 and 2.22.

$$Q_{L,1} = C_{d,L}(Re) \cdot A_L(x_{L,1}) \cdot \sqrt{\frac{2}{\rho} (|P_t - P_{c,1}|) \cdot \text{sgn}(P_t - P_{c,1})} \quad (2.21)$$

$$Q_{H,1} = C_{d,H}(Re) \cdot A_H(x_{H,1}) \cdot \sqrt{\frac{2}{\rho} (|P_{c,1} - P_{load}|) \cdot \text{sgn}(P_{c,1} - P_{load})} \quad (2.22)$$

where

A_L	Discharge area of low pressure valve	$[m^2]$
A_H	Discharge area of high pressure valve	$[m^2]$
$C_{d,L}$	Calculated based on eq. 2.2 with $Re_t = 175$ and $C_{d,max} = 0.62$	[.]
$C_{d,H}$	Calculated based on eq. 2.2 with $Re_t = 100$ and $C_{d,max} = 0.50$	[.]
$\text{sgn}(\cdot)$	Signum function returns the sign of the argument	[.]

The discharge coefficients C_d and reynolds transition number Re_t for the LP valve is found based on an experiment conducted at $T = 44^\circ$ [Johansen and Rømer, 2011, p.114]. The source indicates a reference oil density of $\rho = 870[kg/m^3]$ at $T = 15^\circ$. However, it is not clear if the source compensates for the effects of higher temperatures on the oil density when $C_{d,L}$ is determined. As a result of this, the

announced discharge coefficients C_d is used in this report without modifications. The discharge coefficient and the Reynolds transition number of the HP valve is found iteratively through simulation. The discharge area A_L and hydraulic diameter $d_{h,H}/d_{h,L}$ are a function of the valve position $x_{p,i}$. These are defined in equation 2.23 and 2.24 for the LP valve and equation 2.25 and 2.26 for the HP valve [Johansen and Rømer, 2011, p.220-221].

$$A_L(x_{L,i}) = \pi \sin(\gamma_L) D_L x_{L,i} - \frac{\pi}{2} \sin(\gamma_L) \sin(2\gamma_L) x_{L,i}^2 \quad (2.23)$$

$$d_{h,L}(x_{L,i}) = \frac{4 \sin(\gamma_L) D_L x_{L,i} - 2 \sin(\gamma_L) \sin(2\gamma_L) x_{L,i}^2}{2 D_L - \sin(2\gamma_L) x_{L,i}} \quad (2.24)$$

$$A_H(x_{H,i}) = \begin{cases} D_H \pi x_{H,i} & \text{for } x_{H,i} < \frac{D_H}{4}. \\ \frac{\pi}{4} D_H^2 & \text{for } x_{H,i} \geq \frac{D_H}{4}. \end{cases} \quad (2.25)$$

$$d_{h,H}(x_{H,i}) = \begin{cases} 2x_{H,i} & \text{for } x_{H,i} < x_{H,max}. \\ D_H & \text{for } x_{H,i} \geq x_{H,max}. \end{cases} \quad (2.26)$$

where

$D_{h,L}$	LP valve hydraulic diameter where $D_L = 20.72[mm]$	[m]
$D_{h,H}$	HP valve hydraulic diameter where $D_H = 7[mm]$	[m]
x_L	LP valve displacement from 0[mm] to $L_{L,max} = 1.55[mm]$	[m]
x_H	HP valve displacement from 0[mm] to 3[mm]	[m]
γ_L	Angle of LP valve head $\gamma = \frac{\pi i}{3}$	[rad]

Leakage Q_{leak} is flowing out of the chamber symbolised by a pink flow path in figure 2.3. As the figure indicates, two main sources contributes to the leakage. One is the annular gap in between piston and cylinder housing. The other is the gap between the hexagon and the piston foot. Since each opening is a potential source of leakage, the leakage is most likely also present through the HP valve and LP valve. It is therefore difficult to determine how much each part contributes to the total leakage flow. An adjustment coefficient c_{leak} is introduced in the annular leakage model to account for the total leakage. This coefficient is determined based on measurements.

$$Q_{leak,1} = c_{leak} \frac{\pi (P_{c,1} - P_t)}{8\mu L_l} \left[r_o^4 - r_i^4 - \frac{(r_o^2 - r_i^2)^2}{\ln\left(\frac{r_o}{r_i}\right)} \right] \quad (2.27)$$

where

c_{leak}	Adjustment coefficient of leakage $c_{leak} = 300$	[.]
L_l	Leakage path $l_l = 15[mm]$	[m]
r_i	Inner annulus radius, $r_i = 11.5[mm] - 8[\mu m]$	[m]
r_o	Outer annulus radius, $r_o = 11.5[mm]$	[m]

This concludes the model of the working chamber as all the variables affecting it are described. Next, the model of the load can be described.

2.3.3 Load model

The Digital Displacement Pump can be used in various applications. It could be used to drive a hydraulic motor, to move a piston in an actuator or to keep a steady pressure level for a hydraulic system. In all cases, the load of the system boils down to become a pressure node that is disturbed by different sources. Therefore, the load used in this report is assumed to be a chamber of fixed volume V_{load} , see figure 2.4.

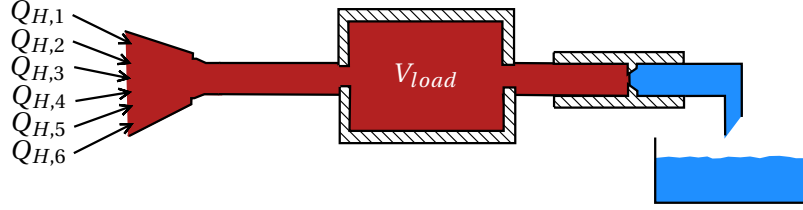


Figure 2.4: A fixed volume load with a fixed orifice that is dimensioned according to a nominal pressure and flow.

This model is chosen in order to keep the load simple to adjust, yet sufficient to challenge a flow controller. The disturbance in the pressure node is provided by an orifice flow Q_{load} from the load chamber to a reservoir. The governing equation of the chamber is given in equation 2.28. The flow equation of the load, given in equation 2.29, is calculated as a function of a nominal flow and pressure at the load. The discharge coefficient and the fixed opening area at the load is included through the nominal parameters. The volume of the chamber is chosen to be only $V = 0.5[L]$ in order to provoke large pressure gradients so the control strategy is challenged.

$$\dot{P}_{load} = \frac{\beta}{V_{load}} \left(\sum_{i=1}^6 Q_{H,i} - Q_{load} \right) \quad (2.28)$$

$$Q_{load} = \frac{Q_{nom}}{\sqrt{P_{nom}}} \cdot \sqrt{(P_{load} - P_T)} \quad (2.29)$$

where

Q_{nom}	Nominal flow at load	$[m^3/s.]$
P_{nom}	Nominal pressure at load	$[Pa]$
V_{load}	Volume of the load chamber, $V_{load} = 0.5[L]$	$[m^3]$

2.4 Mechanical system model

The mechanical system consists of three different elements; the high pressure valve, the low pressure valve and the hexagonal nut. The equation of motion of the valves are modelled by using Newtons second law. The equation of motion of the nut is derived by use of Euler-Lagrange. Euler-Lagrange simplifies the derivations when dealing with a system that is affected by forces from various direc-

tions. The gravitational forces are neglected due to the smaller masses of the valves which has an insufficient impact on the valve response.

2.4.1 High pressure valve

The high pressure valve is an industry standard passive valve component. A basic model of the valve is outlined by using evident knowledge. The pressure acting on the effective area on both sides of the valve, the spring attached to the valve and frictional forces that dampens the pistons dynamics. However, the lack of information about the valve makes it difficult to determine its parameters accurately. Therefore, the model and parameters proposed by a project group at Aalborg University is utilised and given in equation 2.30 [Johansen and Rømer, 2011, p.42,221]. The viscous damping coefficient B_H and the stiffness of the spring k_H is modified based on results from simulations.

$$m_H \ddot{x}_H = (P_{ci} - P_{load}) \cdot A_{He} - B_H \cdot \dot{x}_H - k_H \cdot (x_H + x_{H0}) - F_{flow, hp} \quad (2.30)$$

where

m_H	Mass of the high pressure valve $m_H = 0.007$	[kg]
P_{load}	Load pressure	[Pa]
A_{He}	Effective area on both sides of HP valve $A_{He} = \frac{p^i}{4} (7.0[mm])^2$	[m ²]
k_H	High pressure valve spring stiffness $k_H = 350$	[Pa/m]
B_H	Viscous damping coefficient $B_H = 13.6$	[Ns/m]
x_H	High pressure valve position	[m]
x_{H0}	Initial displacement of spring $x_{H0} = 0.001$	[m]

A flow force is added in the model and a discharge angle of $\gamma_H = 58[^\circ]$ is chosen based on simulation response. The flow force is derived by using Reynolds Transport Theorem on a control volume (CV). The rate of change of fluid momentum inside a CV contributes by a transient flow force. The net rate of efflux of momentum through a control surface contributes with a steady state flow force [Andersen and Hansen, 2007, Chap.3]. Only the steady state force contribution is modelled in this report. The steady state flow force is given in equation 2.31.

$$F_{flow, hp} = \cos(\gamma_H) Q_{H,i} \sqrt{2\rho |P_{c,i} - P_{load}|} \operatorname{sgn}(P_{c,i} - P_{load}) \quad (2.31)$$

2.4.2 Low pressure valve

The forces acting on the low pressure valve are thoroughly examined by Johansen and Rømer [2011]. These are an actuator force, a flow force, a friction force, a suction force and the pressure difference across the valve. The valve is controlled by the electro magnetic actuation force. The fluid flowing through the valves discharge area creates a flow-force acting to close the valve [Andersen, 2003, chapter 2]. A viscous and coulomb friction force with increased damping at end positions to oppose the

movement of the valve. Lastly, a suction force near end positions due to vacuum-like circumstances hinders the valve to take off. When the valve takes off from an end point, a cavity is formed which generates a force to oppose the valve movement. The purpose of this report is not to recreate a comprehensive model of the LP valve but to design a flow controller. Therefore, a simpler yet precise nonlinear model that captures the main dynamics is build. Hence, the proposed suction force is left out of the model as well as a thorough derivation of the parameters affecting the motion of the low pressure valve. The equation of motion for the LP valve is given in equation 2.32.

$$m_L \ddot{x}_{L,i} = F_{act} - F_{fric,lp} - F_{flow,lp} - A_{Le} \cdot (P_{c,i} - P_t) \quad (2.32)$$

where

m_L	Mass of the low pressure valve $m_L = 0.0385$	$[kg]$
A_{Le}	Effective area of the low pressure valve head $A_{Le} = 4.3[cm^2]$	$[m^2]$
$x_{L,i}$	LP valve position constrained to move between $0[mm]$ and $1.55[mm]$	$[m]$

The friction force is modelled as a drag force and a viscous damping force, see equation 2.33.

$$F_{fric,lp} = B_v \dot{x}_{L,i} + B_D \text{sign}(\dot{x}_{L,i}) \dot{x}_{L,i}^2 \quad (2.33)$$

where

B_v	Viscous friction model	$[Ns/m]$
B_D	Drag coefficient for LP valve $B_D = 170$	$[Ns^2/m]$

The drag coefficient B_D is iteratively determined through simulation. The model of the viscous friction B_v was derived in Johansen and Rømer [2011] and the same model with the defined coefficients are used in this report, which is given in equation 2.34. The constant viscous friction coefficient B_0 is derived considering the movement of two parallel surfaces relative to each other and the shear-stress in the lubricating oil film. The Navier-Stokes equation are used where gravitational effects are neglected and a pure steady viscous flow in one direction is assumed. The source proposes a correction coefficient for B_0 , but this is left out in this report as the simulations shows satisfying results. The constant viscous friction coefficient B_0 is given in equation 2.35.

$$B_v = B_0 + B_{near,op} e^{-\frac{l_L - x_{L,i}}{x_{0,op}}} + B_{near,cl} e^{-\frac{x_{L,i}}{x_{0,cl}}} \quad (2.34)$$

$$B_0 = \mu \cdot \left(\frac{A_{lp,b}}{l_{lp,b}} + \frac{A_{lp,se}}{l_{lp,me}} \right) = 6.5509 \left[\frac{N \cdot s^2}{m} \right] \quad (2.35)$$

where

l_L	LP valve stroke length, $l_L = 1.55[mm]$	$[m]$
$l_{lp,b}$	Distance between LP valve body surface and housing, $l_{lp,b} = 20[\mu m]$	$[m]$
$l_{lp,me}$	Distance between LP valve magnet extension surface and housing, $l_{lp,me} = 100[\mu m]$	$[m]$
$A_{lp,b}$	LP valve body surface area, $A_{lp,b} = 9.55[cm^2]$	$[m^2]$
$A_{lp,me}$	LP valve magnet extension surface area, $A_{lp,me} = 5.31[cm^2]$	$[m^2]$
$x_{0,op}$	Region of exponential damping near opening end	$[m]$
$x_{0,cl}$	Region of exponential damping near closing end	$[m]$
$B_{near,op}$	Exponential viscous friction coefficient near opening-end $B_{near,op} = 2000$	$[Ns^2/m]$
$B_{near,cl}$	Exponential viscous friction coefficient near closing-end $B_{near,cl} = 7500$	$[Ns^2/m]$
B_0	Viscous friction coefficient	$[Ns/m]$

The steady state flow forces for the LP valve is given in equation 2.36.

$$F_{flow,lp} = \cos(\gamma_L) Q_{L,i} \sqrt{2\rho|P_t - P_{c,i}|} \operatorname{sgn}(P_t - P_{c,i}) \quad (2.36)$$

The actuation force is the driving force on the LP valve. This force is created by an electro magnetic force from a conducting wire. First a comprehensive model based on electromagnetic circuit theory was derived, then a simplified fourth order transfer function approximation was proposed in [Johansen and Rømer, 2011, p.52,119] that effectively predicts the steady state value and the initial transient force response. The same simplified model is also applied in this report without any modifications.

$$\frac{F_{act,1}(s)}{F_{ref,1}(s)} = \left(\frac{\omega_{n,e}^2}{s^2 + 2\zeta_e \omega_{n,e} s + \omega_{n,e}^2} \right)^2 \quad (2.37)$$

$\omega_{n,e}$	Natural frequency of the electrical actuation system $\omega_{n,e} = 2000$	$[rad/s]$
ζ_e	Damping ratio of the actuation system $\zeta_e = 0.8$	$[.]$

2.4.3 Actuation strategies for the LP valve

The cylinders can be operated through the LP valve in three different operation modes; full displacement operation, partial displacement operation and idle operation. Each mode describes how the LP valve is operated during a 360° cycle. The position of the pistons in each cylinder is described by a local angular reference $\theta_{local,i}$ such that BDC is at $\theta_{local,i} = 180^\circ$ and TDC is at $\theta_{local,i} = 360^\circ$. The applied forces in each operation mode are estimated based on the red curve in figure 2.5.

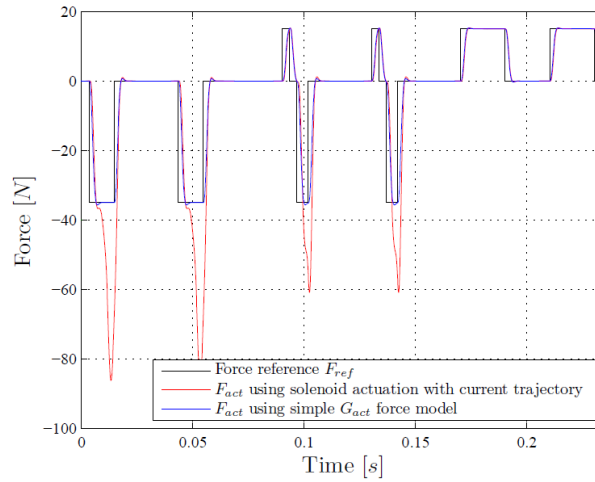


Figure 2.5: LP valve actuation force estimated from current trajectory (red) given a force reference (black). [Johansen and Rømer, 2011, p.89]

Full displacement mode takes advantage of a full stroke from BDC to TDC. The process is explained beginning from $\theta_{local,i} = 0^\circ$. The piston initiates a movement from TDC to BDC causing the pressure $P_{c,i}$ to decrease. The LP valve can be opened by an actuation force or by the pressure difference. The later happens when the pressure in the working chamber gets below the tank pressure P_t and this is also the chosen opening-actuation method for the LP valve. The opening angle $\theta_{op,i}$ is included in figure 2.6 to illustrate how it could be applied. Once the valve is open, fluid flows into the chamber. This is called the intake-stroke. A closing force is applied such that the solenoid valve closes latest at 180° . This means that the time-delay before the LP valves has opened/closed is accounted for. The closing strategy for a full displacement is given in equation 2.38 and the closing angle $\theta_{cl,i}$ can be defined individually for each valve.

$$F_{ref,i} = \begin{cases} -90[N] & \text{for } \theta_{local,i} \geq \theta_{cl,i} \\ 0[N] & \text{elsewhere} \end{cases} \quad (2.38)$$

The outlet stroke is during the piston movement from BDC at 180° to TDC at 360° . At this stroke the volume decreases and the pressure increases in the working chamber. The fluid from the chamber flows to the load when the pressure-force is high enough to open the HP valve.

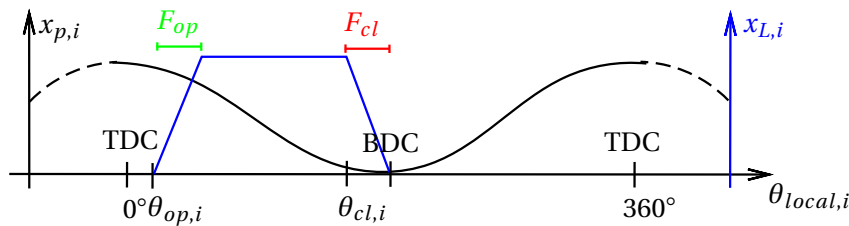


Figure 2.6: Full displacement actuation strategy illustrated with the LP valve position and the piston position

In idling mode, the LP valve is held open by actuation force, see figure 2.7. The positive actuation force is used to counteract the pressure forces experienced by the valve. The pressure in the working chamber $P_{c,i}$ increases as the piston initiates its discharge stroke. Therefore, the idle force is applied so it is effective from BDC, see equation 2.39.

$$F_{ref,i}(s) = \begin{cases} 15[N] & \text{for } \theta_{local,i} \geq 180^\circ \\ 0[N] & \text{elsewhere} \end{cases} \quad (2.39)$$

Fluid is streaming between the working chamber and the reservoir with a low pressure drop. Thus, energy efficient idle operation is obtained.

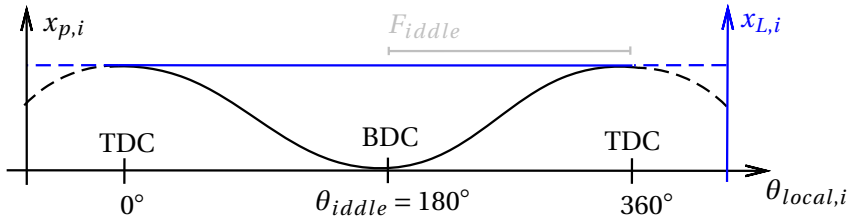


Figure 2.7: Idle operation mode illustrated with the LP valve position and the piston position

Partial displacement mode is a combination of full displacement and idling operation. It is similar to the full displacement operation mode during the intake stroke. Instead of using a fixed closing angle, the closing angle is allowed to vary in between $\theta_{cl,i} \in [0^\circ : 360^\circ]$. In order to prevent the LP valve to close during the discharge stroke if $\theta_{cl,i} > 180^\circ$, a positive actuation force is applied in the period $\theta_{idle} \in [180^\circ : \theta_{cl}]$, see the strategy in equation 2.40.

$$F_{ref,i}(s) = \begin{cases} -90[N] & \text{for } \theta_{local,i} \geq \theta_{cl,i} \\ 15[N] & \text{for } \theta_{cl,i} \geq \theta_{local,i} \geq 180^\circ \\ 0 & \text{elsewhere} \end{cases} \quad (2.40)$$

During idle mode, part of the fluid into the working chamber is pumped back into the tank. The remaining fluid in the chamber is pumped into the load, hence a partial displacement is achieved

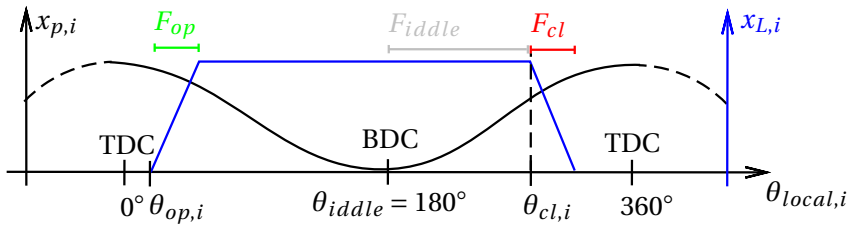


Figure 2.8: Partial displacement actuation strategy illustrated with the LP valve position and the piston position

2.4.4 Dynamics of the Hexagonal Nut

The pump shaft is driven by a motor in order to operate the DDP. The torque that is necessary to rotate the shaft has to overcome a frictional torque, torque due to forces from the working chambers and the inertia of the system. The six cylindered DDP has spring forces $F_{sp,i}$, pressure forces $F_{pr,i}$ and frictional forces $F_{f,i}$ acting from 6 different directions as illustrated on figure 2.9 on a hexagonal nut. The pistons and the hexagon is assumed to be a single rigid body. The nut is located near the cylinder inlet to piston 1,2 and 3 in this configuration. A larger force is therefore expected from these pistons, which is illustrated by the compressed springs and the longer arrows. The illustration is simplified and the forces from the referred chambers are not identical.

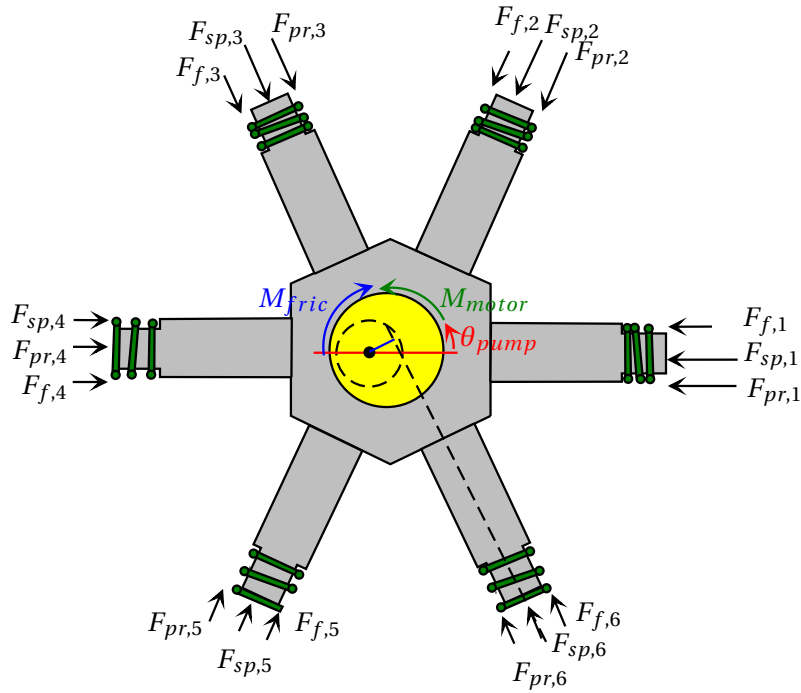


Figure 2.9: Forces acting on the hexagonal nut from multiple directions.

It is not a simple task to derive the equations of motion for the hexagon by applying Newton's second law in conventional form. Instead, the Euler-Lagrange equation from calculus of variation is used which is equivalent to Newton's second law. This approach yields the same results by use of a systematic method that starts from the potential V and kinetic T energies of the system. The Lagrangian is defined as the difference between the kinetic and potential energy $L = T - V$. The Euler-Lagrange is solved for the polar coordinate θ in order to obtain the equation of motions for the hexagonal nut.

$$\frac{d}{dt} \left(\frac{\partial L}{\partial \dot{\theta}_{pump}} \right) - \frac{\partial L}{\partial \theta_{pump}} = M_{external} \quad (2.41)$$

The external torque $M_{external}$ is a collection of torques that are not defined in the Lagrangian L .

$$M_{external} = M_{motor} - M_{pressure} - M_{friction} \quad (2.42)$$

Among these are the input torque from a driving motor M_{motor} , the frictional torque $M_{friction}$ and the torque generated by the pressure in the working chambers $M_{pressure}$. The frictional torque includes the frictional forces from the cylinder and the viscous damping between hexagon cavity and the eccentric piston. Even though the pressure torque and frictional torque are undoubtedly internal, these are collected as external torques in order to avoid inconsequential details. They are respectively given in equation 2.43 and 2.44.

$$M_{pressure} = -A_{cp}r_e \left[\sum_{i=1}^6 \sin \left(\theta_{pump} - \frac{(i-1)\pi}{3} \right) P_{c,i} \right] \quad (2.43)$$

$$M_{friction} = -B_p r_e \left[\sum_{i=1}^6 \sin \left(\theta_{pump} - \frac{(i-1)\pi}{3} \right) \dot{x}_{p,i} \right] + C_{fr} B_e \dot{\theta}_{pump} \quad (2.44)$$

The pistons are radially displaced 60° apart from each other. Their torque contribution to the hexagon is given as the the spring and pressure forces multiplied by an arm w.r.t. the center of the shaft. The arm varies with the rotation of the shaft θ and is illustrated in figure 2.9 for piston 6.

A model of the motor is not carried out in this report due the to limitations in the time frame. The resulting equation of motion for the hexagonal nut is collected in appendix A.2 in case a motor model is available.

The aim of the equation of motion is to obtain an angular velocity of the shaft θ because at a given time instant, the angle of the shaft defines the position and velocity of each piston, thus the volume of the working chambers. Therefore, the angular velocity will have a direct impact on the pressure gradient of the working chambers as seen in equation 2.18. Nowadays, even basic motor control algorithms are capable of keeping a steady state shaft speed. Changing load conditions might challenge the precision of the controllers, but it is highly unlikely that a large velocity deviation will be observed as long as the motor is dimensioned to carry the load. For this reason, it is assumed that the motor is working approximately in steady state for the remainder of the report. To account for changing loads, a pressure dependent term is added to the constant angular velocity $\dot{\theta}_{p,constant}$. This term is modelled as a linear function, so that when the pressures in the working chambers reach the load pressure level, this will reduce the angular velocity by a small amount ϵ .

$$\dot{\theta}_{pump} = \dot{\theta}_{p,constant} \left(1 - \epsilon \left[\sum_{i=1}^6 \frac{P_{c,i}}{P_{load}} \right] \right) \quad (2.45)$$

where

ϵ Change in angular velocity as a function the working chamber pressure $\epsilon = 0.02$ [.]

2.5 Verification of DDP model

A model of a Digital Displacement Technology is already verified at Aalborg University [Johansen and Rømer, 2011, p.125-132]. It is therefore considered favourable to verify the model in this report based

on the data obtained from previous work, in order to make use of existing knowledge and spend more time on research in the reports focus area. A short summary of how the verification was carried out is explained succeedingly.

2.5.1 Data acquisition and method of validation

The model was verified at 1500RPM, a load pressure of approximately 200[Bar] and for opening-closing actuation forces. The working chamber pressure P_c , the load pressure P_{load} and the position sensor for the LP valve was logged during the tests. A combination of the signal amplifier and the pressure sensor creates a bandpass filter with lower break frequency at 1[Hz] and higher break frequency at 100[kHz]. Steady state measurements could therefore not be obtained, hence no information about absolute pressure levels was obtained. The pressure levels was estimated by an accuracy of 1[Bar] based on estimated intake pressure levels. Measured pressure data is offset so that at BDC $P_{c,meas} = 0[Bar]$. The sampling rate was defined to be 10[kHz]. At 1500[RPM] this results in 0.9° difference between each sample.

The used method to validate the Digital Displacement Technology in this report is, simply, to create the same plot by using the model in this report. The plots from the source contains simulation data (Data B) and measurement data (Data C). The data obtained from the model in this report is named Data A. Once the plots are obtained, the two figures are plotted side by side to compare the results.

2.5.2 Variations in the models

The parameters in this model is mainly found from the same source and therefore similar results are expected. Furthermore, it is plausible that deviation between announced and applied parameter values exists. Most parameters are known with an accuracy of two decimals. The models are not identical and therefore deviations are expected. The main difference between the models lies in two forces that are neglected in this report; a suction force which is used to oppose a valve movement from the endpoints and a transient flow force for the LP valve. Instead, a steady state flow force is used for both the HP and LP valve in this report. A model of the change in density and viscosity as a function of both temperature and pressure is included at each chamber. Also, some of the parameters are adjusted in order to reduce the deviation between model predictions (Data A) and measurement data (Data C). The main changes is based on the fact that the LP valve dynamics are faster in the measurements than in simulations. A number of reasons for this is identified;

- the closing force is increased from $F_{cl} = -35[N]$ to $F_{cl} = -90[N]$
- the damping coefficients (viscous and drag) are reduced by more than 50%

These changes affects the output flow, hence the dynamics of the HP valve also needs to be adjusted:

- the viscous friction coefficient is changed from $B_H = 5[Ns/m]$ to $B_H = 7[Ns/m]$

- the stiffness of the spring constant is changed from $K_H = 500[N/m]$ to $K_H = 355[N/m]$
- the maximum discharge coefficient is changed from $C_{d,H,max} = 0.4$ with a transition region at $Re_{t,H} = 200$ to $C_{d,H,max} = 0.5$ and a transition region at $Re_{t,H} = 150$.

2.5.3 Comparison of simulated and measured data

Three plots are selected from the source in order to verify the model. These are respectively a flow and a pressure plot both for a closing angle $\theta_{cl} = 165^\circ$, and a plot of the output flow rate as a function of the closing angle θ_{cl} .

The first plot can be seen in figure 2.10 for the pressures. A period of 360° is from TDC to TDC, i.e. from $t = 0.02[s]$ to $t = 0.06[s]$. A closing force $F = -90[N]$ is applied at $\theta_{cl} = 165^\circ$.

The pressure gradients are similar in Data A and B, but both deviates from Data C. Data C contains non-steady pressure ripples which is not observed in the simulations. The cause for this can be explained by a phenomena called water hammering if the transducer to measure $P_{c,i}$ is not physically protected appropriately.

At takeoff from the endpoints, Data B shows curving tendencies for x_L . This gives a delay in closing and opening times. As a consequence of this, deviations in flow rates are expected between Data B and the others. The LP valve does not show the curving tendency in Data C because its position is calibrated so the valve is fully closed at $x_L = 0$. This curving tendency is neither observed in Data A. However, it is seen that the LP valve reaches bottom position slightly faster in Data A than Data C.

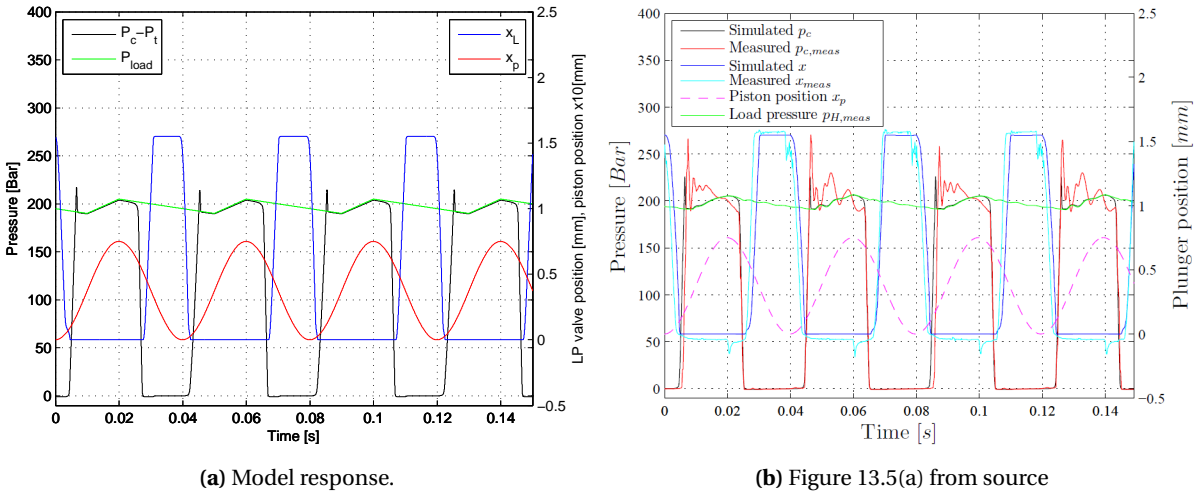


Figure 2.10: Simulated response of a working chamber pressure and an LP valve position from (a) the model and (b) from the source. A negative solenoid actuation force step is applied every $\theta_{cl} = 165^\circ$ in order to close the valve. Initial shaft angle is $\theta = 180^\circ$. The shaft takes one revolution from $t = 0.02$ to $t = 0.06$

Two plots are found from the sources to validate the flows. The first plot shows the flow through the working chamber for a closing angle of $\theta_{cl} = 160^\circ$, see figure 2.11. The internal flows such as the flow

through the LP valve and leakage is not measured. The data is obtained from the same simulation as in figure 2.10.

A deviation in the average flow rates are obtained between Data A,B and C. The back flow through HP valve is predicted to be larger in Data A than in Data B, mainly due to the increased damping coefficient B_H . The opposite is observed for the LP valve. Here, Data A shows less back flow than Data B and this is mainly because of the faster dynamics of the valve in data A. Because of this, the error in the output flow compared to measurement Data C is reduced drastically in Data A. Data A deviates by less than 2% in the whole operation range while Data B errors are more than 7%. The leakage flow in data A and B shows comparable results and also the height of the peaks for flow through the LP valve. Data A predicts a lower output flow peak than Data B, but it is not possible to determine which one is correct without high resolution measured data.

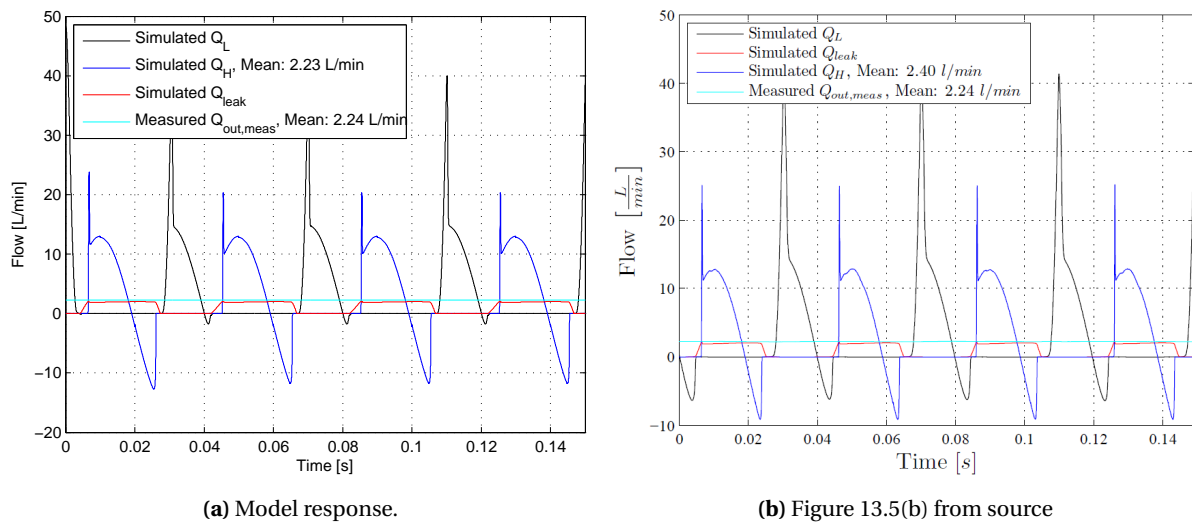
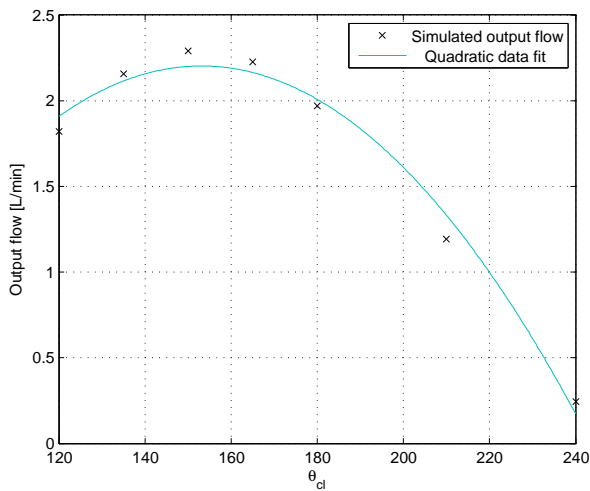
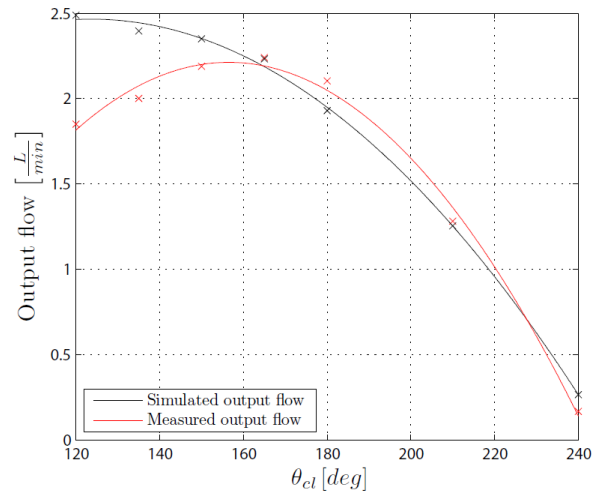


Figure 2.11: Flow simulations obtained from (a) the model and (b) the source. The flow through the LP and HP valves are simulated along with the leakage flow. An average of the measured output flow is displayed in the plot.

The second plot in figure 2.12 shows the average flow rate for different closing angles.



(a) Model response.

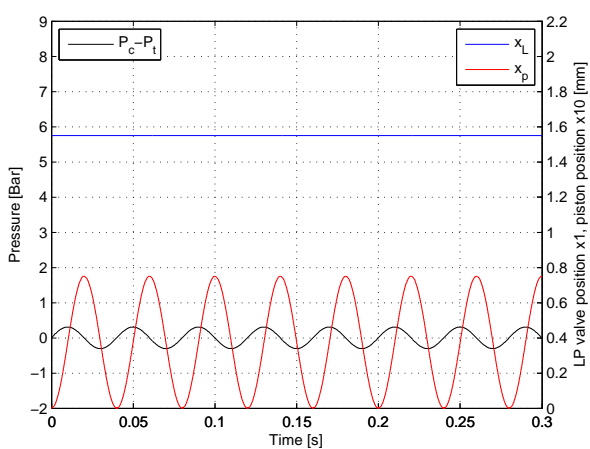


(b) Figure 13.6 from the source.

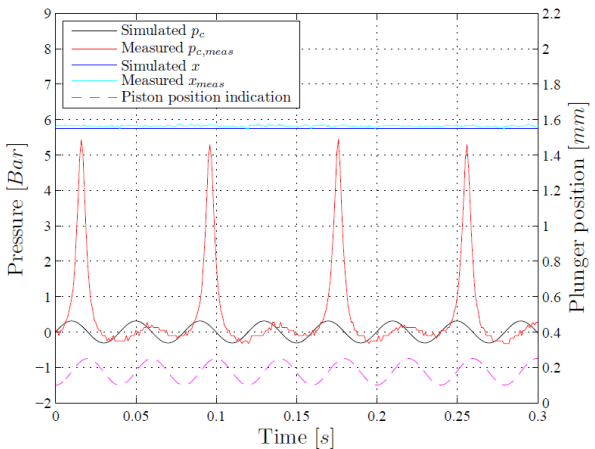
Figure 2.12: Flow as a function of the closing angle θ_{cl} from (a) the model and (b) the source.

The model in this report generally predicts similar behaviour as the measurements. There are however some minor deviations in the curves. Data C shows a peak at a closing angle $\theta_{cl} = 165^\circ$ while the peak in Data A is approximately at $\theta_{cl} = 155$. The deviation between Data A and C is kept below $0.2[L/min]$ at all data points. Data B does not capture the same tendencies as Data A and C. The peak flow is given at $\theta_{cl} \approx 120^\circ$ where a $0.6[L/min]$ output flow error is observed. Data B does give accurate estimates for $\theta_{cl} \geq 200^\circ$ even though the flow gradient deviates.

The pump in idle operation mode is plotted in figure 2.13. The model approximately predicts the same idle pressure dynamics as the simulation from the source. A fully open valve is identically located at $x_L = 1.55[mm]$ for all data. The similar behavior in the simulations validates the pressure drop over the LP valve, the discharge areas, the volume and dimensions of the working chamber.



(a) Model response.



(b) Figure 13.7 from source.

Figure 2.13: Idle operation of pump where the LP valve is fully open during 360° by use of an actuation force $F_{act,op} = 15[N]$

This model is hereby deemed to be valid for test of control strategies since the model approximately predicts the same dynamics as documented by the source at a temperature of $T_{oil} = 20^{\circ}C$. It is very conservative to believe that the pump will only operate at this temperature. A hydraulic system with movable parts is bound to loose energy as heat due to friction between the parts which causes the temperature of the oil to rise. The substantial leakage coefficient results in a very high leakage flow at increasing temperatures. This decreases the working chamber pressure and reduces the maximum pressure that the pump is capable of supplying flow. As a consequence of this, it is necessary to review the design of the pump in order to increase the temperature span that the pump can work within. A solution for the great amount of leakage between the piston foot and the hexagon face is needed. However, this is not the focus area of the project and therefore it is assumed in the following parts of the report that the leakage coefficient is $c_{leak} = 10$.

Analysis of the Digital Displacement Pump Model

This chapter contains an analysis of the nonlinear DDP model derived in section 2. The overall task is to determine the input-output relation of the DDP. The purpose of using a DDP is due to its high efficiency at a wide range of operation points. Therefore, it is adjacent to analyse the system starting from the input signals. The input signals are chosen considering energy efficiency and an acceptable output power range. Furthermore, a study of the time delays in the DDP is carried out for control design purposes. This is followed by an analysis of the output flows. Here, the goal is to reveal the sensitivity of the DDP's output flow towards changing oil temperature and load pressures. Additionally, the instantaneous output flow is examined to identify flow measurement methods. An overview of the DDP system treated in this chapter, is illustrated in figure 3.1.

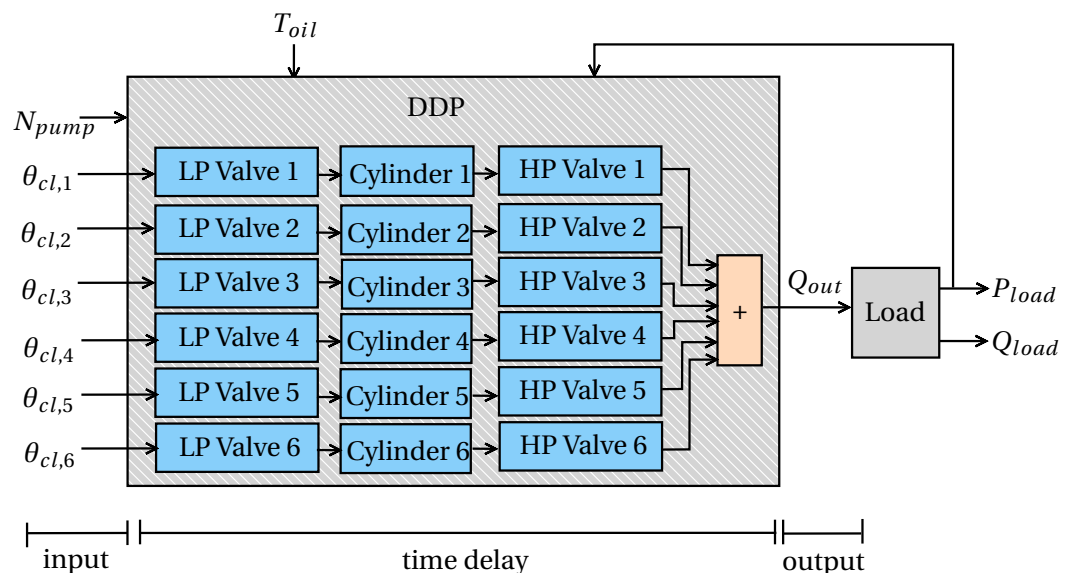


Figure 3.1: Simplified DDP system overview that illustrates the input signals, the delays and the output signal for a DDP.

The input signal to the DDP is a pump speed N_{pump} and closing angles $\theta_{cl,i}$ for each LP valve where

$i \in \{1, 2, 3, 4, 5, 6\}$. The delays in the DDP system is caused by LP valve's closing-time, the pressurising-time in working chamber of the cylinders and the HP valve's closing-time. The output flow Q_{out} from the DDP consists of the the flow through the HP valve's. The DDP system is disturbed by the oil temperature T_{oil} and the load pressure P_{load} as illustrated.

Before the analysis is carried out, a short summary of the general elements used in this chapter is presented to the reader. Here, the reader is given facts regarding oil parameter variation and information about how the simulations are performed can be read as well.

3.1 Preliminaries

The DDP model is implemented in an MATLAB Simulink environment and simulated using a third order fixed-step Bogacki-Shampine solver. The states of the model in the next time step is explicitly computed based on the current state and state derivatives. The order of the solver determines the accuracy, i.e. a fourth order solver would be more accurate. The increased accuracy comes at the expense of longer simulation times. However, simulations showed that the difference between the results from a third order and fourth order solver was merely noticeable. The chosen step size is iteratively determined as $T = 1[\mu s]$ in order to obtain a large data resolution.

The reader is encouraged to review figures in appendix A.4 before reading this chapter to brush up on how changes in oil temperature and pressure variations effects the bulk modulus, dynamic viscosity and the density of the oil. To shortly summarise the main points:

- The dynamic viscosity increases with increasing pressure and decreasing oil temperature.
- The effective bulk modulus increases with increasing pressure. However, it is saturated at pressure levels above approximately $100[Bar]$ to $\beta = 10000[Bar]$.
- The density of the oil changes mainly as a function of oil temperature. The density increases as oil temperature decreases. Additionally, the density increases vaguely with increasing pressure.

3.2 System input

The key property of a DDP is its ability to operate energy efficiently under variable displacement conditions. First, the volumetric efficiency of the DDP is calculated using simulation data in order to define a pump speed N_{pump} . A higher volumetric efficiency indicates that the DDP can operate under higher pump speeds and still maintain a high output power. Next, a volumetric efficiency study is conducted at two different oil temperatures. Using this analysis, the closing angles $\theta_{cl,i}$ are constrained to avoid redundancy in the input/output relation so two different θ_{cl} does not give the same Q_{out} (for fixed P_{load} and T_{oil}). This is used in chapter 5 to simplify the control design. Finally,

a total system efficiency of the DDP is computed to explore the energy efficiency of the pump. Here, $\theta_{cl,i}$ are identified that gives higher system efficiency.

3.2.1 Pump speed

The definition of volumetric efficiency is the ratio between actual pump flow over the theoretical pump flow, see equation 3.1 [Andersen and Hansen, 2007, Chap.2].

$$\eta_{vol} = \frac{Q_{out}}{Q_{t,out}} \quad (3.1)$$

The available theoretical pump flow, given in equation 3.2, is a function of the LP valves actual closing angle and the velocity of the piston.

$$Q_{t,out} = A_{c,p} \cdot \int_{\theta_{cl,actual}}^{360^\circ} \dot{x}_{c,i}(\theta_{pump}) d\theta_{pump} \quad (3.2)$$

The average output flow rate from a single cylinder is integrated over one period of the pumping cycle $[0 : 360^\circ]$. Likewise, the velocity of the piston is measured in the interval $[\theta_{cl,actual} : 360^\circ]$.

Figure 3.2a shows the volumetric efficiency of the DDP for a range of pump speeds N_{pump} and load pressures P_{load} . The closing angle is defined as $\theta_{cl} = 155$ and the oil temperature as $T = 40^\circ C$.

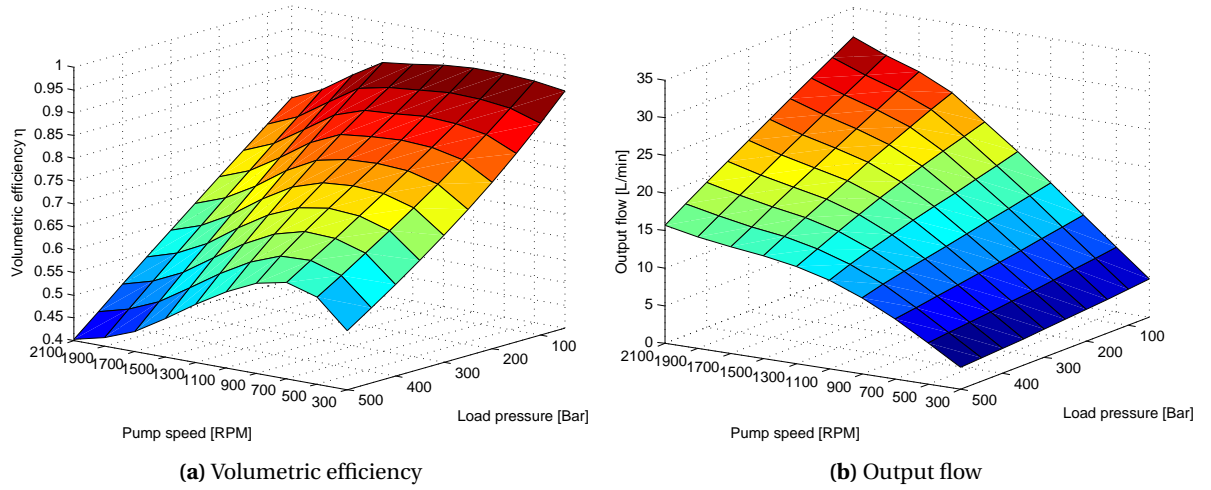


Figure 3.2: Data obtained from simulations at $40^\circ C$, a closing angle of $\theta_{cl} = 155^\circ$ and various load pressures and pump speeds where (a) shows the volumetric efficiency and (b) shows the total output flow from six cylinders.

The difference between the volumetric efficiency curves are due to a nonlinear increase in the dynamic viscosity at low temperatures. When the viscosity increases, it increases the damping coefficients of the valves causing a larger response time. Ultimately, it affects the amount of oil that can enter the working chamber and the amount of back-flow there is. This is the reason why at lower temperatures, the volumetric efficiency suddenly decreases.

At lower pressure levels the volumetric efficiency curve is merely flat around 900[RPM]. At higher pressure levels the volumetric efficiency curve crumbles around 900[RPM]. Figure 3.2b shows the corresponding output flow at the mentioned operation points. Here, it is seen that for fixed P_{load} the output flow Q_{out} increases linearly with N_{pump} . It is also known that the frictional torques increases with N_{pump} , see equation 2.44. If the increased Q_{out} caused by higher N_{pump} does not make up for the increased frictional torques, it is not desirable to increase the pump speed further. At $P_{load} = 50[Bar]$ the rate of increase in Q_{load} attenuates for $N_{pump} > 1700[RPM]$ and at $P_{load} = 500[Bar]$ it attenuates for $N_{pump} > 1300[RPM]$. Without utilising a profound analysis, a compromise between these two is chosen. Hence, the pump speed in the remainder of this report is defined as $N_{pump} = 1500[RPM]$. The output power at this pump speed ranges from 2.15[kW] to 11.4[kW] depending on the load pressure level.

3.2.2 Closing angle

The closing angle θ_{cl} to the LP valves can in reality take any real number for $\mathcal{R} \in [0^\circ : 360^\circ]$. Due to a back-flow phenomena, which is described in section 1.4 and identified in section 3.3.3, the pressure in the working chamber is not necessarily decreased sufficiently when $\theta_{local,i} = 0^\circ$. This means that the suction period can not be initiated before the back-flow stops. Nevertheless, when the piston in the cylinder moves down from TDC at some point the suction period starts. Additionally, when the piston in the cylinder moves up from BDC the discharge period starts. This causes the size of the working chamber volume to change. The size of the working chamber volume is symmetric around the point where the piston is at BDC. This is also evident from the volumetric efficiency plot of the DDP, which is given in figure 3.3a and 3.3b for $T_{oil} = 20^\circ$ and $T_{oil} = 40^\circ$ respectively.

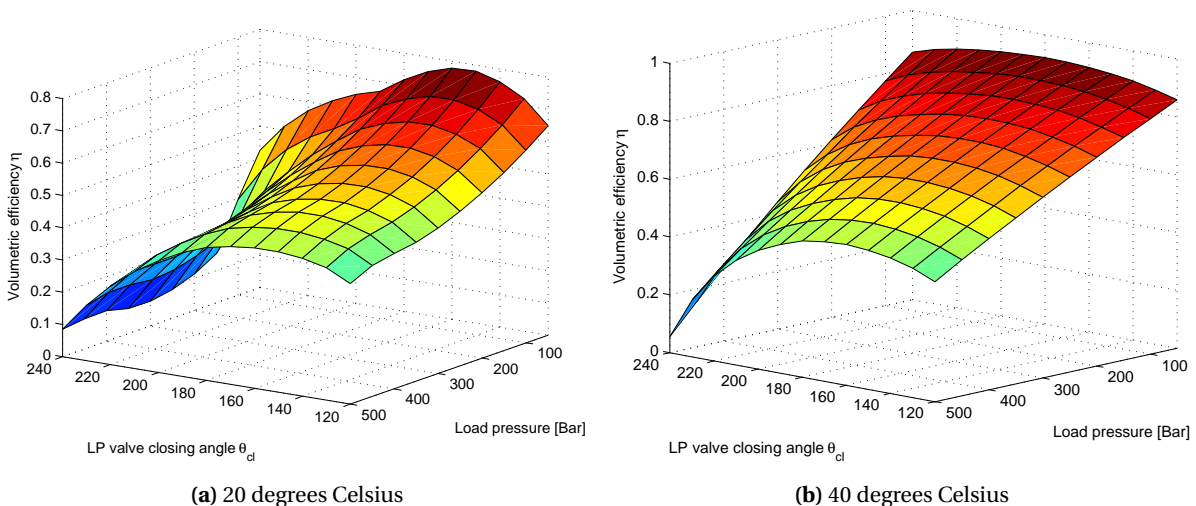


Figure 3.3: Volumetric efficiency at 20 and 40 degrees Celsius for different load pressures and closing angles at 1500[RPM].

Both plots of figure 3.3 shows that the volumetric efficiency is to some extent symmetric in a region around $\theta_{cl,i} = 155^\circ$. The piston reaches BDC at $\theta_{local,i} = 180^\circ$, so a time delay between a given signal

and actual execution is observed which is examined later in a succeeding section.

The same volumetric efficiency at two different $\theta_{cl,i}$ means that ratio of the theoretical output flow rate and the simulated output flow is identical. In addition, figure 3.8 shows that the corresponding simulated output flow rates are also nearly identical at the same $\theta_{cl,i}$'s. If the output flows are nearly identical at two closing angles, this unnecessarily increases the tasks complexity for a controller. For that reason, the input signal to the LP valve is constrained to be in the domain $\theta_{cl} \in [155 : 360]$. This reduces the complexity of the control strategy because one less decision needs to be taken.

3.2.3 Total system efficiency

The total efficiency of a hydraulic system is defined as the volumetric efficiency η_{vol} multiplied by the hydro mechanical efficiency η_{hm} . Another method to calculate the total efficiency is by using the ratio between output power P_{out} and input power P_{in} . The output power from the DDP is the product between load pressure P_{load} and output flow Q_{out} . The input power consist of the power to control the LP valve and the power to rotate the pump shaft. The following assumptions are made to simplify the calculations; there is no electro magnetic losses in the actuator and the pump speed is constant. The total system efficiency can be calculated as in equation 3.3 [Andersen and Hansen, 2007, Chap.2].

$$\begin{aligned} \eta_{total} &= \eta_{vol} \cdot \eta_{hm} = \frac{P_{out}}{P_{in}} \\ &= \frac{\int P_{load} \cdot Q_{out} dt}{\int M_{motor} \cdot \omega_{pump} + F_{act} \cdot \dot{x}_L dt} \end{aligned} \quad (3.3)$$

According to Andersen and Hansen [2007, Chap.2] the hydro mechanical efficiency decreases as the pump speed increases. A low pump speed gives a lower maximum output flow rate which is not desirable. A compromise is to keep the pump speed at 1500[RPM], as defined, to avoid reducing the hydro mechanical efficiency further and also to keep a large maximal output flow rate from the pump.

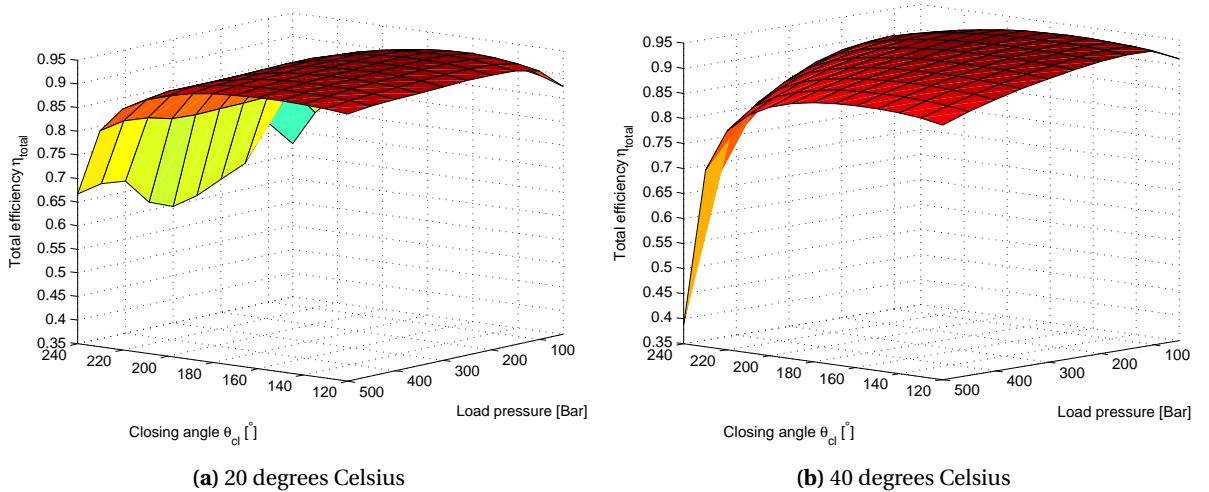


Figure 3.4: Total system efficiency at an oil temperature of (a) $T = 20^\circ C$ and (b) $T = 40^\circ C$.

Figure 3.4a shows the system efficiency at $T = 20^\circ C$. It is seen that, the efficiency is relatively high for closing angles $\theta_{cl} < 220$ where the efficiency is bounded by $\eta_{total} \in [0.85 : 0.95]$. The total efficiency of the system for a temperature of $T = 40^\circ$ is shown in figure 3.4b. Again, relatively high efficiency curves are obtained which is bounded by $\eta_{total} \in [0.85 : 0.95]$ for most of the operation points. The system efficiency again decreases for $\theta_{cl} < 220$ and most rapidly at higher load pressure levels.

Both plots shows that the most energy efficient control strategy to apply on a DDP is one that utilises a full-displacement operation mode as the partial displacement operation mode shows to be less energy efficient. However, in agreement with the problem formulation, the partial displacement operation mode is chosen. This is because it gives less output flow pulsations.

3.3 Time delay

This section analysis the time delays within the DDP. This delay comprise of the time it takes for an input signal to propagate to the output. Additionally, it comprise of the time-length that an input signal affects the output. Review section 1.4 for a thorough exposition of the time delays.

The analysis starts in a chronological order. First, the time it takes to fully close the LP valve $t_{lp,cl}$ is identified. Next, the time it takes to pressurise the fluid t_{pr} is analysed. Lastly, the time it takes to close the HP valve $t_{hp,cl}$ is examined.

The sum of the time delays $t_{lp,cl}$ and t_{pr} is equivalent to the time it takes before an input signal starts to affect the output flow. This is used to design a simplified model of the DDP for control purposes in chapter 5.

The time delay $t_{hp,cl}$ is used to identify the number of active cylinders within a time instant. This information is, also, used in the control strategy to adapt the DDPs input/output map $f(\cdot)$, explained in section 6.

3.3.1 LP closing time delay

The closing time of the LP valve is plotted in figure 3.5 for different oil temperatures. The load pressure is irrelevant for this study because the LP valve opens and closes at pressure levels near reservoir pressure P_t , which is assumed to be constant.

The closing time of the LP valve increases vaguely for decreasing temperatures. This is because the damping coefficient increases due to a higher dynamic viscosity μ .

The time delay is larger when $\theta_{cl} < 180^\circ$. This is due to the alternating expansion and contraction period of the working chamber volume. The volume expands during $\theta_{pump} \in [0 : 180[$ causing $P_{c,i}$ to decrease. Hence, the pressure drop over the LP valve forces the valve in open-direction, see equation 2.32. If the closing angle lies in this period, the actuator of the LP valve observes more resistance. Contrary, the closing time is lower when $\theta_{cl} > 180^\circ$. This is because $P_{c,i}$ increases as the volume contracts. It causes the pressure drop over the LP valve to work in the same direction as the actuator, i.e. the pressure drop helps the actuator to close the LP valve.

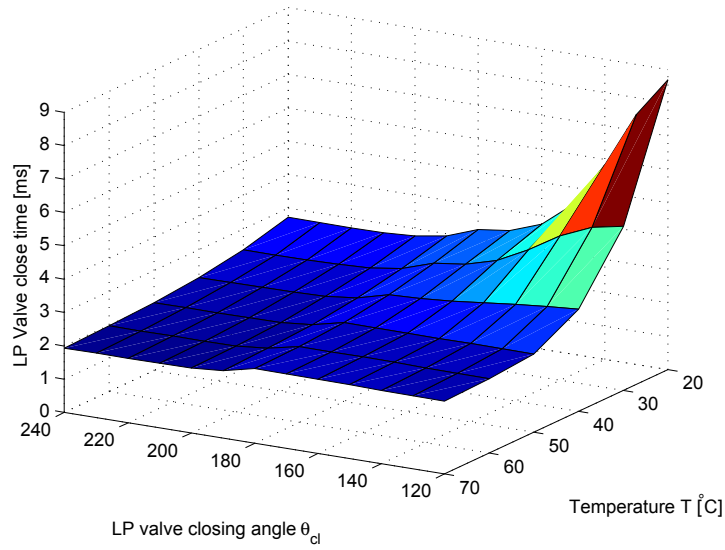


Figure 3.5: The time it takes to close the LP valve for various oil temperatures.

The peak at $\theta_{cl} = 120^\circ$ and $T_{oil} = 20^\circ$ is caused by the exponential damping coefficient defined in equation 2.34. The actuator force is not large enough to both overcome the exponential damping-force and the pressure-force. The exponential damping coefficient are determined based on trial-and-error and they are believed to be overestimated. However, this can not be concluded without a series of measurement on the DDP prototype. This is not carried out in this report due to limitations in the time frame.

3.3.2 Fluid pressurising time delay

The pressurising delay is shown in figure 3.6 where (a) is calculated for various load pressure levels at $T_{oil} = 20^\circ\text{C}$ and (b) is calculated for various temperatures at $P_{load} = 200[\text{Bar}]$.

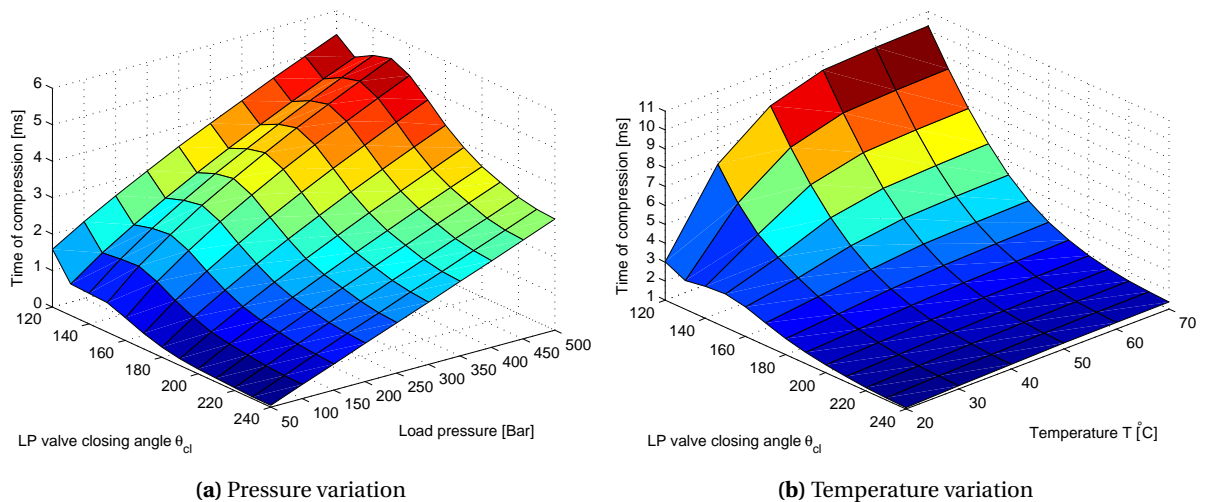


Figure 3.6: The time duration for compressing the fluid to reach load pressure for (a) various load pressure levels at 20°C and (b) various temperatures at $200[\text{Bar}]$ load pressure.

A peak in compression time is observed at approximately $\theta_{cl} = 155^\circ$. The compression time is expected to be largest when the working chamber contains most oil, i.e. when the LP valve actually closes at $\theta_{pump} = 180^\circ$ (piston at BDC). Considering the time it takes to close the LP valve, it is reasonable that the largest compression time is located prior to $\theta_{cl} = 180^\circ$.

When the working chamber contains less oil, the compression time decreases. In the figures, this is observed for $\theta_{cl} > 155^\circ$ and also for $130^\circ < \theta_{cl} < 155^\circ$. But at closing angles lower than $\theta_{cl} < 130^\circ$ the compression time increases unexpectedly. The reason for this is because the LP valves actuator force is not large enough to close the valve. The LP valve is attempted to close as the working chamber volume expands. The LP valve remains vaguely open due to an exponential damping coefficient explained in the previous subsection.

At some operation points, the compression delay is relatively large. The time delay $t_{pr} = 5[ms]$ is equivalent to a phase delay of 45° . This delay could be reduced by decreasing the dead volume. Utilising the continuity equation for the case when both the LP and HP valves are closed gives

$$\dot{P}_c = \frac{\beta}{V_{c,0} - A_{c,p} \cdot x_c} \cdot (\dot{V}_c - Q_{leak}) \quad (3.4)$$

Here it is seen that the chamber volume has a direct influence on the pressure gradient. Due to a large dead volume $V_{c,0}$, the value of the denominator fluctuates between $14.75[cm^3]$ and $17.9[cm^3]$. By decreasing the dead volume, larger volume fluctuates thus a larger pressure gradients could be obtained.

3.3.3 HP valve closing time delay

The back flow time is defined as the time difference between the piston reaching TDC and the HP valve closing. The duration of backflow is plotted in figure 3.7 as a function of the closing angle θ_{cl} and respectively for (a) load pressure variations at $T_{oil} = 20^\circ C$ and (b) oil temperature variations at $P_{load} = 200[Bar]$.

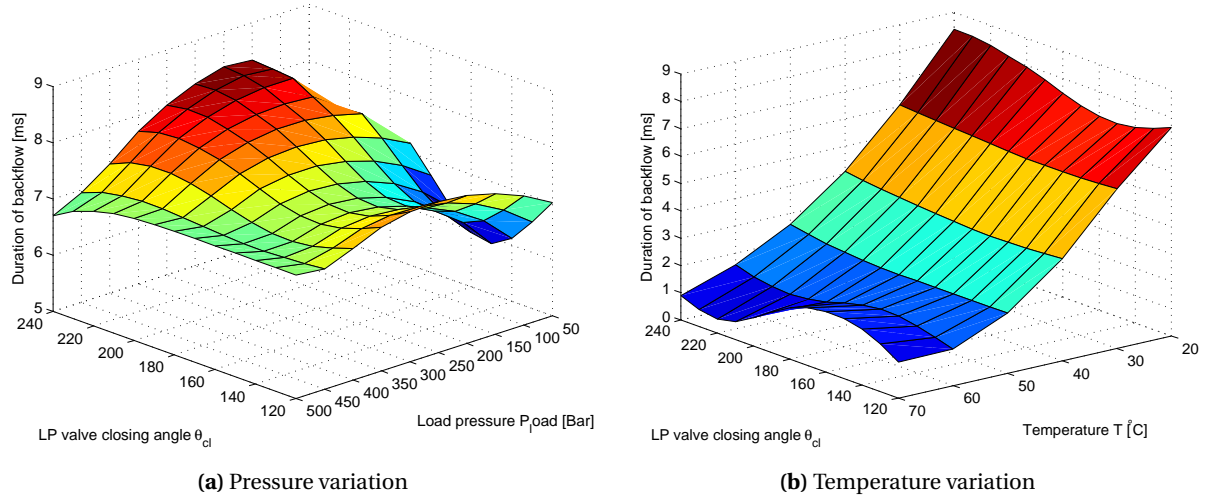


Figure 3.7: The time duration for back flow under (a) varies load pressures at 20°C and (b) various temperature at fixed load pressure of $200[\text{Bar}]$

First of all, a symmetric pattern is observed, once again, around $\theta_{cl} = 155^{\circ}$. See section 3.2.2 for more details.

The simulations indicates that a lower temperature causes a larger back flow time as evident from figure 3.7b. The damping coefficients increases proportionally with the viscosity. Accordingly, it takes a longer time to close the HP valve.

The largest back flow time is observed at approximately $150[\text{Bar}]$ in figure 3.7a. There are two conflicting reasons for this. First, higher pressure levels causes more leakage flow. This reduces the pressure gradient $\dot{P}_{c,i}$ which consequently increases the pressure drop over the HP valve. The pressure exerted on the HP valves surface, forces the HP valve to close faster. Contrary, at lower pressure levels the viscosity decreases. This is especially noticeable at low oil temperatures, see appendix A.4. As a consequence hereof, the HP valve closes faster.

3.4 System output

In this section the output flows sensitivity towards load pressure and oil temperature variations are studied. This is followed by an analysis of the instantaneous output flow from single and multiple cylinders.

3.4.1 Output flow sensitivity

The output flow from a DDP varies when the temperature of the oil changes or the load pressure P_{load} changes for fixed closing angles θ_{cl} . This is shown in figure 3.8a and 3.8b where the output flow from a single cylinder is measured for different θ_{cl} and P_{load} at $T_{oil} = 20^{\circ}\text{C}$ and $T_{oil} = 40^{\circ}\text{C}$ respectively.

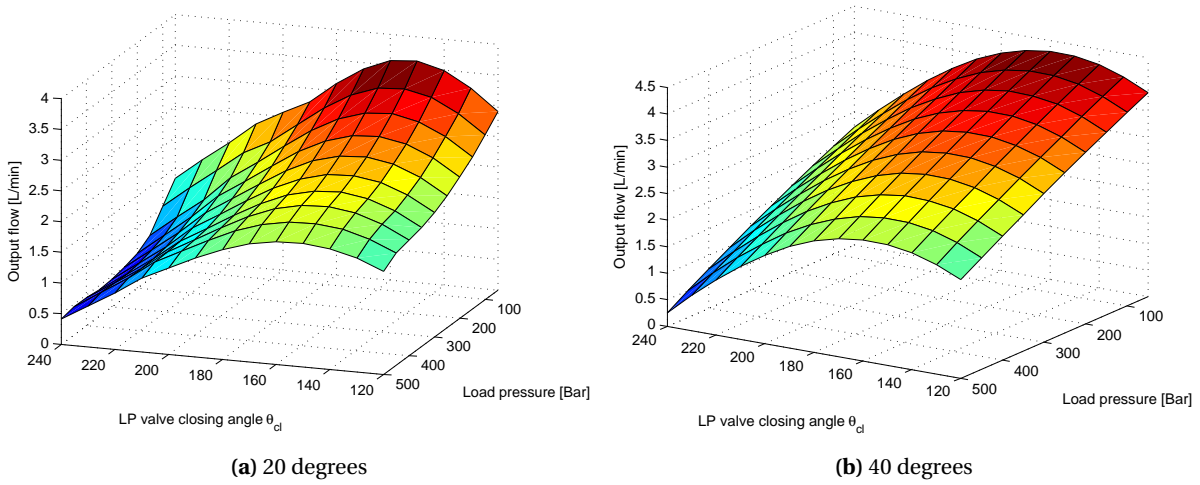


Figure 3.8: Output flow from a DDP as a function of θ_{cl} and P_{load} for the temperature (a) $20^{\circ}C$ and (b) $40^{\circ}C$

A nearly quadratic relation is observed between Q_{out} and θ_{cl} when the P_{load} and T_{oil} are constant. The quadratic behaviour is more obvious at higher temperatures as seen in figure 3.8b.

The reason why the output flow changes with the temperature and the load pressure is due to the changes in the oil parameters modelled in section 2.3.1. These parameters together affects the pressure build up inside the working chambers, the flow in/out of the working chamber and the dynamics of the valves.

The pressure gradient for the working chamber fluid decreases as a result of higher temperatures, due to more leakage flow, see equation 3.4.

The bulk modulus of the oil directly affects the pressure gradient in the chambers which is evident from the continuity equation. The β increases with the pressure of the oil and it saturates at pressure levels above $\approx 100[Bar]$. This is evident from figure A.4b in appendix A.4.

The output flow capability of a six cylindered DDP shows to be highly dependent on the load pressure and oil temperature. At $T = 20^{\circ}C$ the maximum output flow capability changes between $12.0[L/min]$ at $500[Bar]$ and $21.7[L/min]$ at $50[Bar]$. At $T = 40^{\circ}C$ the maximum output flow capability varies between $13.7[L/min]$ at $500[Bar]$ and $25.8[L/min]$ at $50[Bar]$. Fortunately, the oil temperature of a hydraulic system is often close to $T = 40^{\circ}C$ rather than $T = 20^{\circ}C$ which means that the maximum output flow capability of the pump increases.

3.4.2 Output flow shape from a single and multiple cylinders

The construction of a DDP is somehow inspired by pulse-width modulation (PWM) signals known from electronics. The flow from the cylinders is rather a pulsating stream than a steady and continuous one. As capacitors filters a PWM signal in electric circuits, the flow pulsations are filtered using a manifold and sometimes in addition an accumulator. The accumulator is not considered in this report as the manifold or load introduces sufficient filtering, which is explained later in section 4.4.

The output flow from a single cylindered and six cylindered DDP is shown in figure 3.9a and 3.9b respectively.

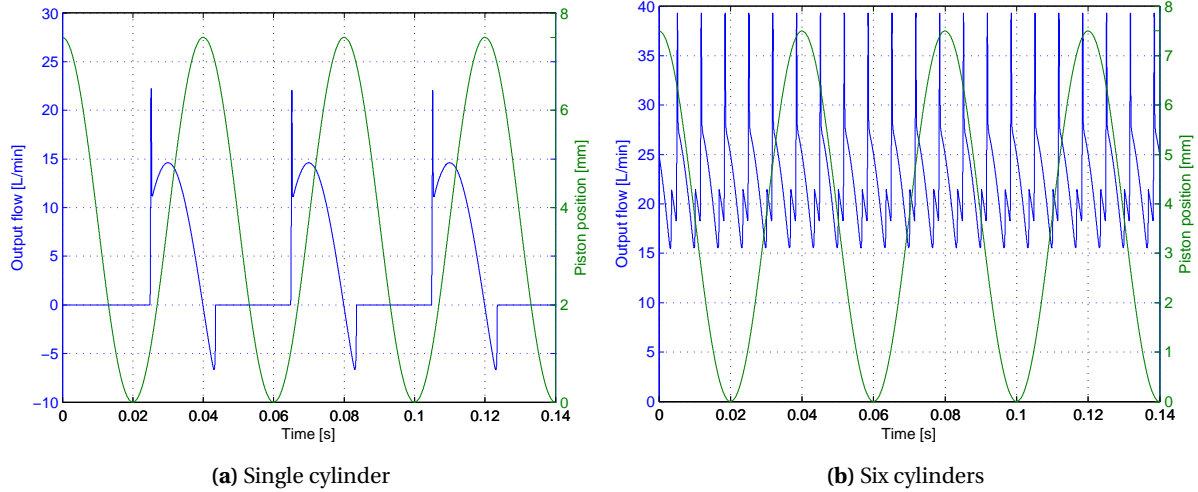


Figure 3.9: Output flow from (a) a single and (b) multiple cylinders given a closing angle $\theta_{cl} = 160$, load pressure $P_{load} = 200[Bar]$ and a temperature of $T = 40$

The instantaneous output flow rate from a single cylinder varies largely during a discharge stroke but it does not exactly resemble a PWM signal. First, the output flow rate creates a spike during the pressure build up phase. The overshoot in the flow is caused by an overshoot in working chamber pressure due to the dynamics of the HP valve. The flow rate becomes more steady when the pressure and the output flow stabilises. Obviously, the output flow is constantly reduced as the pressure inside the working chamber decreases. At some point approximately as the piston passes TDC, the flow direction reverses until the HP valve closes due to decreasing working chamber pressure.

A similar flow pattern is observed regardless of load pressure, oil temperature and closing angle. Especially, the peak flow is almost uniform. The starting point of the flow is determined by the closing angle θ_{cl} and the time of opening the LP valve and pressurising the oil as explained in section 3.3. The ending point of the flow is a function of the HP valves closing time. This is also explained in section 3.3.

The output flow from a six cylindered DDP, given in figure 3.9b, is in effect six flow curves from a single cylinder that is shifted by 60° which results in overlapping flow curves. The result is a periodic pattern with a frequency of $f_{pp} = 6 \cdot 25[Hz]$ because the pump speed is operated at $1500[RPM]$. The instantaneous output flow from each cylinder outlet, the total instantaneous output flow Q_{out} from all cylinders and the position of piston one $x_{p,1}$ is shown in figure 3.10 at an arbitrary operation point used only to identify overlapping flow pattern.

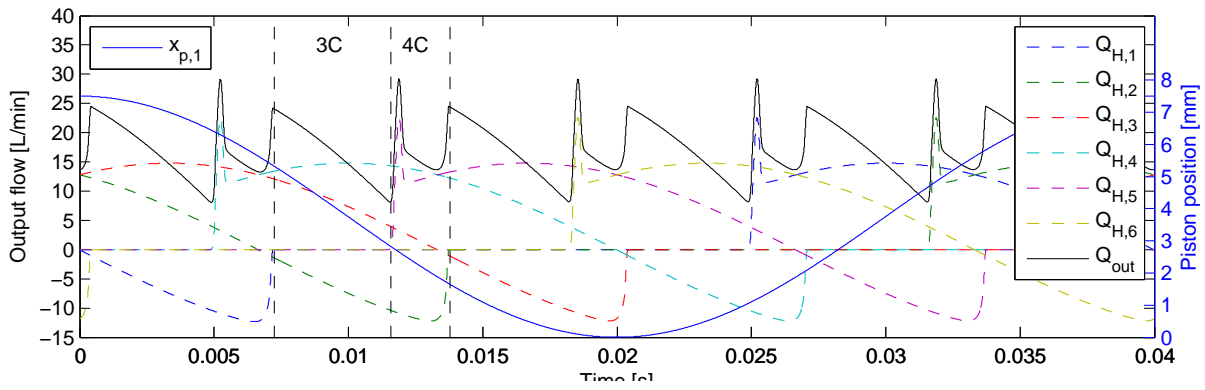


Figure 3.10: Output flow from each outlet of a six cylindered DDP and the total output flow. Data obtained for $T_{oil} = 20^{\circ}C$, a closing angle $\theta_{cl} = 160^{\circ}$ and a load pressure of $P_{load} = 200[Bar]$

The number of cylinders that either pumps or creates suction in any given time instant in the simulated time period switches between 3 and 4. To give an example of these areas, a region of 3 active cylinders is pointed out (3C) and a region of 4 active cylinders (C4). In region 3C, cylinder 3 and 4 contributes with positive discharge and cylinder 2 with negative discharge. In region 4C, cylinder 3,4 and 5 contributes with positive discharge and cylinder 2 with negative. The maximum number of active cylinder would only be 3, if the back-flow phenomena, explained in section 3.7a, did not occur. Obviously, the number of active cylinder is also dependent on the control signal. If every second cylinder receives an idle signal, the number of active cylinder decreases. Based on simulation of the nonlinear DDP model, the maximum recorded active cylinders showed to be 4 for $T_{oil} \in [20^{\circ}C : 70^{\circ}C]$, $\theta_{cl} \in [120^{\circ} : 240^{\circ}]$ and $P_{load} \in [50Bar : 500Bar]$.

Flow Measurement on a Digital Displacement Pump

The task in this chapter is to design a method to measure the output flow from the DDP to be used in control design. Firstly, the possible locations to place a flow transducer is identified and the properties of the available transducer are examined. Then, a frequency spectrum analysis is carried out of the output flow Q_{out} . The flow transducer has insufficient bandwidth to capture Q_{out} without creating aliasing artifacts. Thus, an estimator is introduced to predict the output flow. This is followed by an analysis of filtering methods that obtains the average output flow value. Finally, a flow filter is selected based on its damping ability of the flow ripples and its transient response.

4.1 System overview

There are six different outlets from the DDP. The fluid is directly pumped into a manifold that has a small volume V_M without the use of hoses. The manifold is a ring formed cavity, placed externally around the DDP's circular dimension, that acts as a buffer from which the load can subtract fluid, see illustration in figure 4.1.

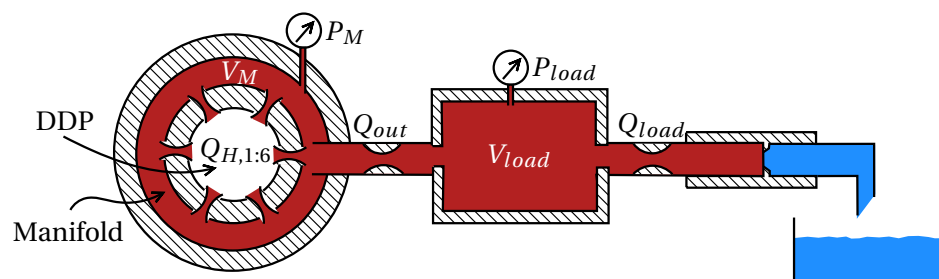


Figure 4.1: System configuration including the DDP, the manifold and the load.

Pressure transducer

A hose connects the manifold and the load. The cross sectional area of the hose is assumed to be large enough to neglect any significant pressure drop between the manifold pressure P_M and the load pressure P_L . Therefore, it is irrelevant whether the pressure transducer is placed at the manifold or the load. The load side is chosen as indicated in figure 4.1.

The pressure transducer together with a current amplifier acts as a bandpass filter with lower cutoff frequency at $1[Hz]$ and higher cutoff frequency at $100[kHz]$ [Johansen and Rømer, 2011, p.213]. The transducer is capable of measuring in the range $0 - 250[Bar]$ with a linearity deviation of less than 0.5% of full scale output [Kistler, 2010]. The confidential band is $\pm 1.25[Bar]$ at every reading. The pressure transducer is not capable of measuring DC values and therefore it is not qualified for the task. However, this transducer gives an idea of the what kind of properties a commercially available pressure transducer can have. Therefore, it is assumed that a pressure transducer is available with a bandwidth of $10[kHz]$ that is able to measure in the pressure range $0 - 500[Bar]$ and able to measure DC values. The bandwidth of the transducer is expected to be sufficient to measure the load pressure. In order to utilise the full bandwidth of the transducer, the sampling frequency of the load pressure is defined to be $f_{s,p} = 10000[Hz]$.

Flow meter

The flow from the DDP can be measured from two distinct locations as seen in figure 4.1; either before the actual load or after. The flow before the load refers to the output flow Q_{out} and the flow after the load refers to the load flow Q_{load} . The difference between the two flows depends on the volume of the cavities and the size of the orifices. Assuming that $V_M \ll V_{load}$, the ripples of the output flow Q_{out} remains intact because the filtering affects from the manifold volume becomes negligible. This is also because the cross sectional area of hoses are assumed to be large as stated previously. Notice, a cavity together with an orifice acts as a first order low pass filter. A large volume gives low bandwidth and vice versa. Contrary, a small orifice gives low bandwidth and vice versa. This is explained more thoroughly later in section 4.4.2. As a consequence of the larger load volume V_{load} , the load flow Q_{load} is a filtered flow with attenuated flow ripples. For that reason, the ideal location of the flow transducer is to measure Q_{out} in order to avoid the response time of the loads first order filtering effects.

The flow meter currently available at the DDP test-setup at Aalborg University is a spring/piston flow meter Parker SCQ-060-0-02 [Johansen and Rømer, 2011, p.210]. The range of the flow meter is $[-60 : 60][L/min]$ [Parker, 2006]. The response time of the spring/piston sensor is less than $2[ms]$. A rule of thumb says that the bandwidth of transducer is approximately $\frac{1}{4}$ th of the inverse of the response time, i.e. $B = \frac{1}{4} \cdot 500 = 125[Hz]$. This is because the response time refers to the time it takes before a flow change is reflected in the measurements. A sinusoidal flow curve roughly consist of four flow changes; from zero to maximum, maximum to zero, zero to minimum, minimum to zero. The sampling frequency of the flow measurement can be defined hereafter to be $f_{s,f} = 125[Hz]$. The fre-

quency response is not given in the datasheet, however the accuracy is stated to be $\pm 2\%$ of full scale. This gives a confidential band that is $\pm 1.2[L/min]$ at every reading.

The frequency spectrum of Q_{out} is analysed in the following section to determine if the flow meters bandwidth is sufficient to avoid aliasing. The data is obtained from simulations of the nonlinear model run with a pump speed of $1500[RPM]$ and an oil temperature of $T_{oil} = 30^\circ C$.

Selecting an oil temperature for the remainder of the report

The reason why the oil temperature is chosen as 30° is based on two arguments. Firstly, the model is validated at $T_{oil} = 20^\circ C$ and secondly the oil temperature during operation is assumed to be larger and probably near $T_{oil} = 50^\circ C$. However, it is not desirable to deviate too much from the validated operation point ($T_{oil} = 20^\circ C$), which is why $30^\circ C$ is considered as a good compromise.

4.2 Frequency spectrum

The output flow is a periodic curve as seen on figure 3.9b in section 3.4.2. In order to reveal the frequency content of the signal, the Discrete Fourier Transform (DFT) of Q_{out} is computed using the Fast Fourier Transform (FFT) algorithm that transforms a time-domain signal into the frequency domain. The DFT is symmetric around the DC value, which means that the amplitude content of the signal is divided into two distinct frequencies, $\pm f$. Since there is no such thing as negative frequencies, the amplitude at $-f$ should be added to the amplitude at $+f$ when reading the plots. The DFT is calculated based on simulation data with the sampling frequency $f_s = 1[MHz]$, see the frequency spectrum in figure 4.2.

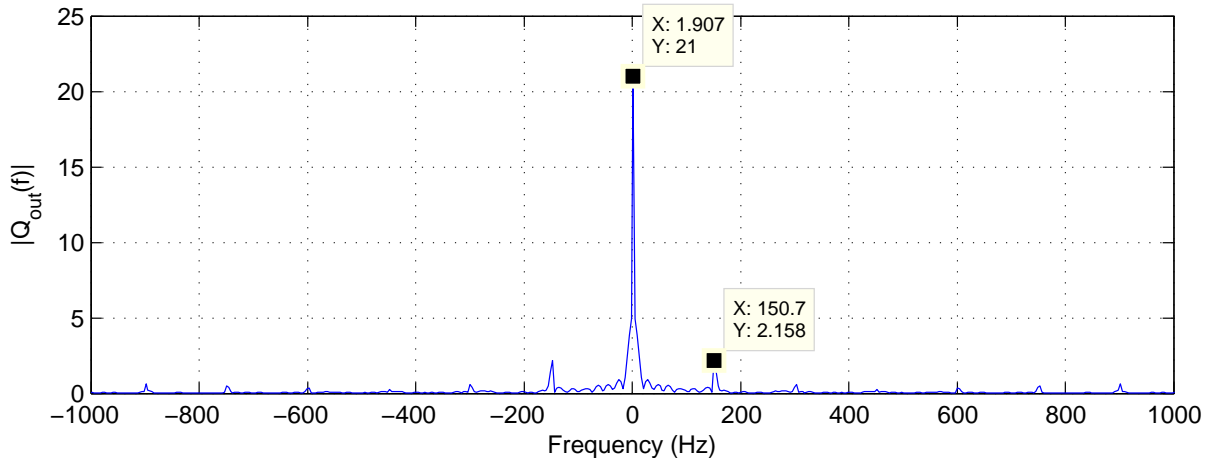


Figure 4.2: Frequency spectrum of the flow signal Q_{out} from simulation using a closing angle $\theta_{cl} = 160$, oil temperature $T = 30^\circ$ and step size $T_{step} = 1 \cdot 10^{-6}$.

The plot shows a peak at $f \approx 0[Hz]$ and several peaks located at $f = n \cdot 150[Hz]$ where $n \in \mathbb{Z}$ with decreasing amplitude for increasing n . The sampling frequency is well above the Nyquist rate of any significant frequency content. As a result, aliasing is avoided and this plot can be used as a reference.

To identify the distortion created by aliasing artifacts from a flow meter, the DFT is calculated using more realistic the sampling frequencies, i.e. $f_{s,f} = 125[Hz]$ and $f_{s,f} = 500[Hz]$. See the respective frequency spectrum in figure 4.3a and 4.3b.

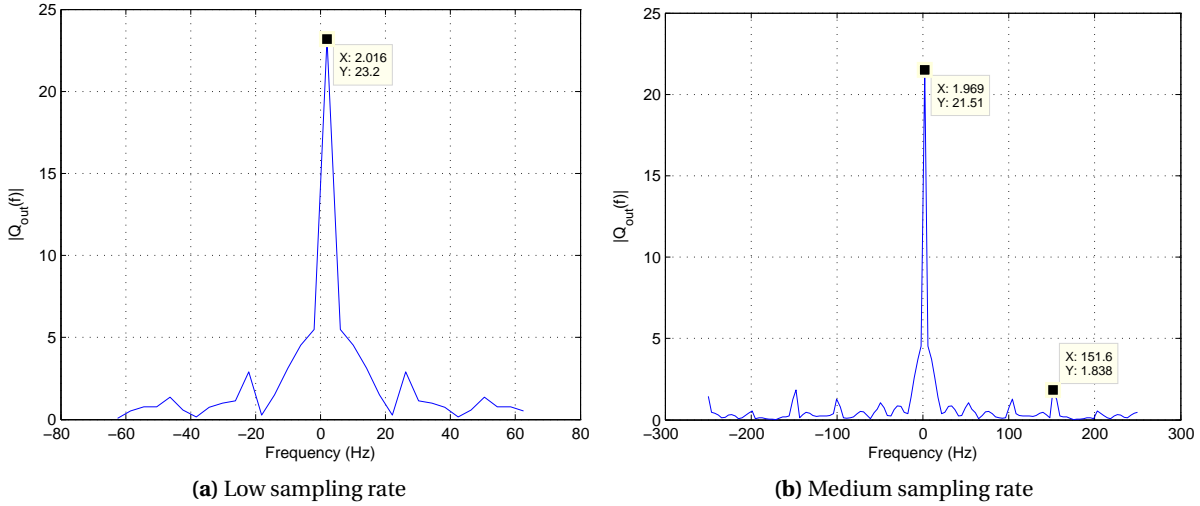


Figure 4.3: Frequency spectrum of the flow signal Q_{out} from simulation using a closing angle $\theta_{cl} = 160$ and sampling frequency of (a) $f_{s,f} = 125[Hz]$ and (b) $f_{s,f} = 500[Hz]$.

At a sampling frequency of $f_{s,f} = 500[Hz]$ the DC content deviates by less than 3% from the reference given in figure 4.2. At $f_{s,f} = 125[Hz]$ the error increases to more than 10%. The plot shows that a flow transducer of minimum $500[Hz]$ would be sufficient to measure Q_{out} when the flow ripples are a multiple of $150[Hz]$.

Based on the above analysis, the output flow Q_{out} can not be measured accurately by use of the available flow meter. Instead, the flow meter has to be used to measure the load flow Q_{load} and based on knowledge of the load, Q_{out} can be estimated. The DFT of the load flow is computed using a high sampling frequency of $f_s = 1[MHz]$ to avoid aliasing, see the spectrum in figure 4.4.

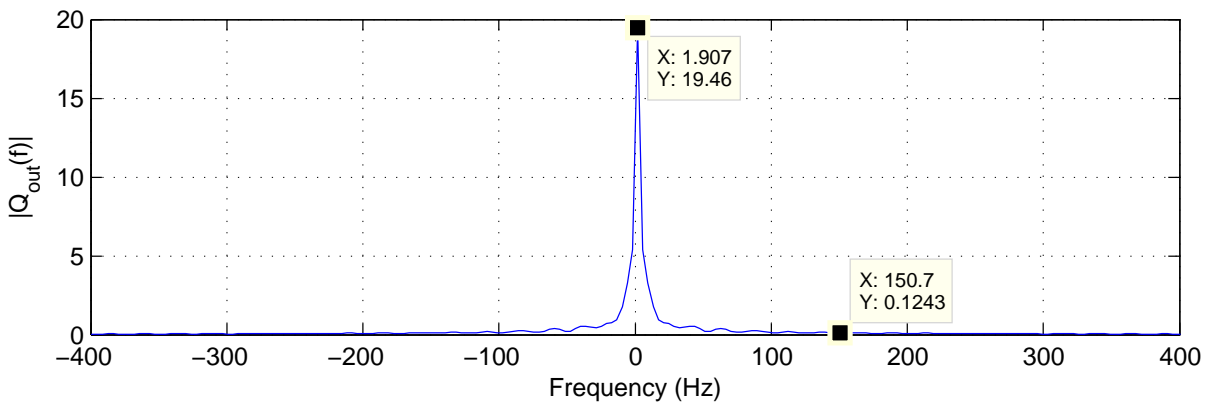


Figure 4.4: Frequency spectrum of the flow signal Q_{load} from simulation using a closing angle $\theta_{cl} = 160$ and a sampling frequency of $f_{s,f} = 1[MHz]$

Based on this plot, it is verified that the flow transducer is applicable to measure Q_{load} because the

load attenuates flow ripples sufficiently. In fact, the flow ripples at $f = 150[Hz]$ has been reduced by more than 94% compared to the reference in figure 4.3.

4.3 Flow estimator

The simplest approach to design an estimator for Q_{out} is to wait for the load pressure to reach a steady state value. When the load pressure remains relatively constant, the average input flow to the load \bar{Q}_{out} is equal the average load flow \bar{Q}_{load} . This can be seen by utilising the continuity equation where the output flow is replaced by its estimated average \hat{Q}_{out} .

$$\dot{P}_{load} = \frac{V_{load}}{\beta} (\hat{Q}_{out} - \bar{Q}_{load}) = 0 \quad (4.1)$$

$$\hat{Q}_{out} = \bar{Q}_{load} \quad (4.2)$$

This approach is relatively accurate when the load pressure stabilises. The disadvantage of using this method is that it is relatively slow, because a new measurement $\hat{Q}_{out} = \bar{Q}_{load}$ can only be taken accurately when the load pressure settles. This inevitably increases the settling time of a flow controller that uses a negative flow feedback, that is designed in chapter 5. It is therefore desirable to speed up the estimator using another approach. Again, by utilises the continuity equation a new estimator can be designed where the pressure gradient is approximated by a numerical differentiation. This method estimates the instantaneous output flow \hat{Q}_{out} , see equation 4.4.

$$\hat{Q}_{out} = \frac{\beta}{V_{load}} \cdot \dot{P}_{load} + Q_{load} \quad (4.3)$$

$$\hat{Q}_{out} = \frac{\beta}{V_{load}} \cdot \frac{P_{load}[n] - P_{load}[n-1]}{T_{sample}} + Q_{load} \quad (4.4)$$

The estimator requires both flow feedback of Q_{load} and pressure feedback of P_{load} . It is essential to have accurate knowledge about the loads volume size V_{load} , the effective bulk modulus of the oil β and a noise free sampling of P_{load} and Q_{load} .

The parameters that are relatively easy to obtain is the V_{load} and Q_{load} . The volume of the load chamber can be measured. Additionally, the load flow Q_{load} can be measured accurately because of its low frequency content as seen in figure 4.4. Any high frequency noise content in the signal can effectively be filtered by a low pass filter using a sampling frequency that was defined to be $f_{s,f} = 125[Hz]$ in section 4.5.

The parameters that are difficult to obtain accurately is β and the noise free measurement of P_{load} . The effective bulk modulus is assumed to be saturated at $10000[Bar]$ and the estimator is therefore sensitive to the accuracy of this value.

The pressure gradient is approximated by numerical differentiation based on two succeeding measurements of P_{load} . This requires a noise free signal from the pressure transducer. It also requires a high sampling frequency in order to capture pressure fluctuation so flow ripples can be replicated.

The bandwidth of the pressure transducer and the sampling rate was defined to be $f_{s,p} = 10[kHz]$ in section 4.1. Due to limitations in the time frame, the pressure samples are assumed to be noise free. The performance of the flow estimator is tested in simulations using a closing angle step input from $\theta_{cl} = 240^\circ$ to $\theta_{cl} = 160^\circ$ and the results are shown in figure 4.5 where the output flow Q_{out} , the estimated output flow \hat{Q}_{out} and the load flow Q_{load} is included. The load flow is included to emphasize that numerical differentiation contributes considerable.

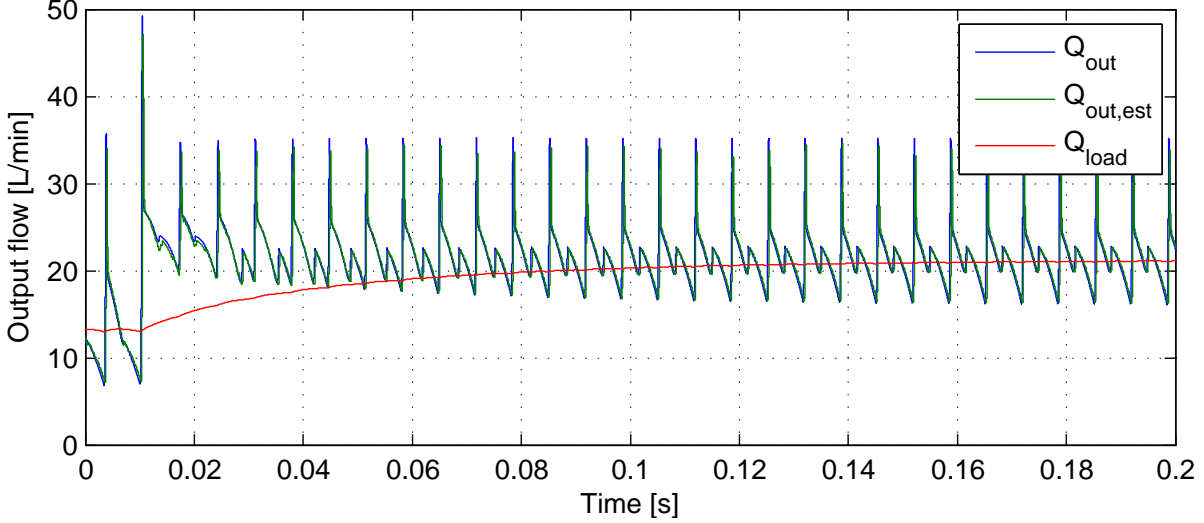


Figure 4.5: Flow estimator performance with a closing angle step from $\theta_{cl} = 240^\circ$ to $\theta_{cl} = 160^\circ$.

The performance of the estimator is relatively accurate both during the steady state and transient period of Q_{load} . The mean square error is computed for $t \in [0s : 0.2s]$ to be

$$MSE(\hat{Q}_{out}) = E[(Q_{out} - \hat{Q}_{out})^2] = 8.04 \quad (4.5)$$

It is worthwhile to notice that the estimator works even though the same flow samples are used multiple times in the flow estimator. The same flow samples is used because there is a difference between the flow sample rate and the pressure sample rate, i.e. $f_{s,p} > f_{s,f}$. In fact, the same flow sample is used 80 times for every time a new pressure sample is taken.

In real applications, noise and disturbances overlays the measured signal and precaution is necessary in order to attenuate the noise.

Sensitivity of the estimator

To test the sensitivity of the estimator for variation in the uncertain parameters, first the upper limit of the effective bulk modulus is over and under estimated by 20%, then the numerical differentiation of P_{load} is over and under estimated by 20%.

The over estimated effective bulk modulus is saturated at $\beta = 120000[Bar]$. The linear range is defined to be from $P \in [1Bar : 140Bar]$ where $\beta \in [275Bar : 12000Bar]$ based on data from appendix A.4 as previously. The result is given in figure 4.6a.

In case of under estimating β , the upper limit of the saturation changes to $\beta = 80000[\text{Bar}]$. This gives a linear range from $P \in [1\text{Bar} : 60\text{Bar}]$ where $\beta \in [275\text{Bar} : 8000\text{Bar}]$, see the results in figure 4.6b.

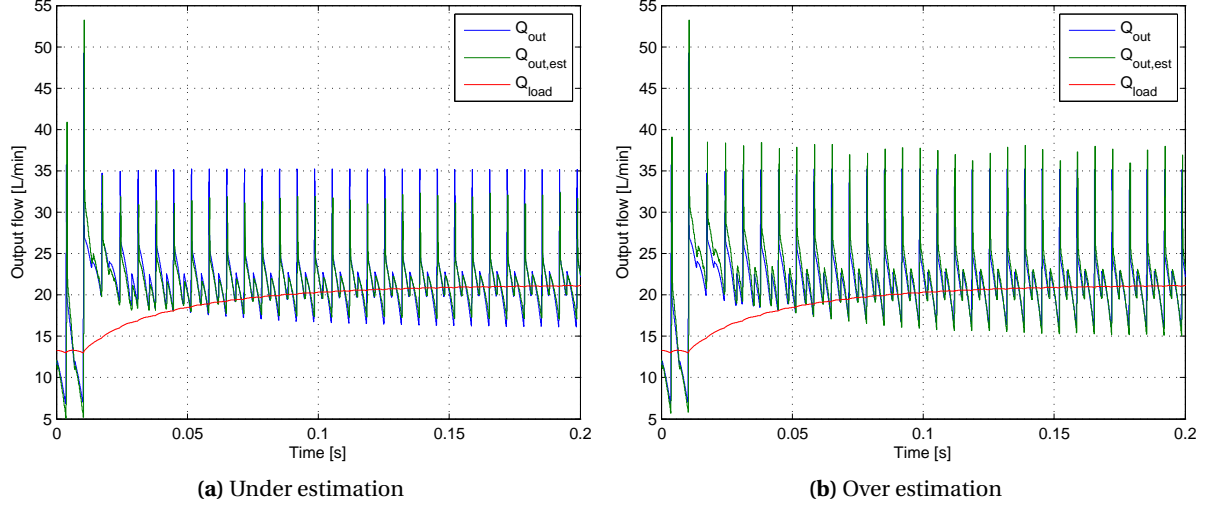


Figure 4.6: Flow estimators sensitivity towards the (a) under estimation and (b) over estimation of the saturation level of the effective bulk modulus by 20%

It is clear from the plots that an over estimation of β over estimates the flow ripples and vice versa both in the transient period of Q_{load} and the steady state period. The mean squared error for over estimation is only $MSE = 7.7656$ and for under estimation it is $MSE = 10.7499$ calculated over the time span $t \in [0s : 0.2s]$. The MSE values are relatively close to each other, which indicates that the error on average does not increase even though the flow ripples are not correctly estimated. The reasoning for this, is that the flow ripples are estimated wrong in both direction around an average value of Q_{out} . Its impact on the average value is therefore minimal. This is seen both in the transient response and the steady state response. Notice, this method requires a relatively good model of β as a function of P_{load} and T_{oil} as the linear approximations are based on this model.

The numerical differentiation is also a source of uncertainty if it is not possible to filter the noise level effectively. The sensitivity of the estimator towards under and over estimating the numerical differentiation showed similar deviations, see the figures in appendix B.1.1.

Based on the above observations, the estimator is deemed valid to be used in control strategies. Having the estimated output flow \hat{Q}_{out} , the task is now to calculate its average value $\hat{\bar{Q}}_{out}$ to use in control strategies.

4.4 Flow filter

The estimated output flow \hat{Q}_{out} contains a lot of ripples. The flow ripples are a natural part of a DDP which is caused by the radial displacement between the cylinders. The ripples could be reduced by implementing more cylinders. In case of a low number of cylinder as 6 in this report, some kind of filtering is necessary to disregard the flow ripples and obtain the average output flow rate. The

average value is equivalent to the DC value, hence filter theory could be applied to obtain the value. The volume of the load V_{load} together with an orifice acts as an analogue filter and therefore the filtering effects from the load is analysed initially, to see if the filtering is sufficient to attenuate flow ripples.

4.4.1 Analogue filtering

The filtering effects can be determined by analysing a linearised pump model. It is not a trivial task to design a linear DDP since it consists of six working chambers and six orifices. The following derivations is therefore build on strongly simplified assumptions. The density of the oil, the discharge coefficients and the effective bulk modulus of the oil β are assumed to be constant.

Figure 2.10a shows that the pressure difference between the working chamber P_c and the load P_{load} is approximately constant during the discharge period of a single cylinder. Assuming that the same observation is valid for six cylinders that contains overlapping discharge period, the DDP can be modelled as a pressure source. As a result of this, the simplified model can be described by two chambers; the load chamber and a single fictitious working chamber. See figure 4.7.

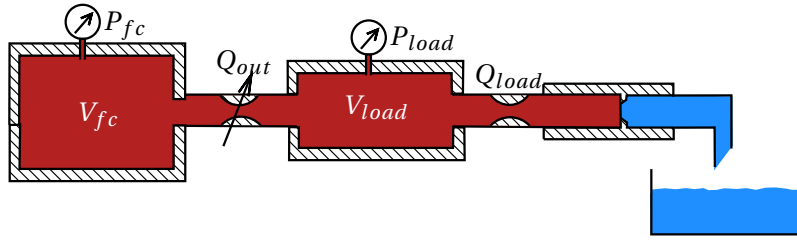


Figure 4.7: System configuration including the DDP, the manifold and the load.

The fictitious working chamber volume V_{fc} is infinitely large, which indicates that there is no pressure variation in the fictitious working chamber, i.e. $\dot{P}_{fc} = 0$. The model simplifies to a continuity equation for the load pressure with orifice equation to model the flow in/out of the chamber.

$$\dot{P}_{load} = \frac{\beta}{V_{load}} (Q_{out} - Q_{load}) \quad (4.6)$$

The variable parameters in the model are P_{load} , Q_{out} and Q_{load} . In fact, Q_{load} only is a function of P_{load} . This is because the load orifice area is constant and it is directly connected to a reservoir with constant pressure, $P_t = 1[Bar]$, see equation 2.29. The Q_{out} consists of flow through the six HP valves that opens/closes during a revolution of the pump shaft. With the above assumptions, Q_{out} becomes a function of P_{load} and an average position of the active HP valves x_{fH} .

The linearisation around the operation point $(x_{fH,0}, P_{load,0})$ is carried out by utilising the Taylor approximation and neglecting higher order terms.

$$\begin{aligned}\frac{V_{load}}{\beta}\Delta\dot{P}_{load} &= \left.\frac{\delta Q_{out}}{\delta x_{fH}}\right|_0 \Delta x_{fH} - \left.\frac{\delta Q_{out}}{\delta P_{load}}\right|_0 \Delta P_{load} - \left.\frac{\delta Q_{load}}{\delta P_{load}}\right|_0 \Delta P_{load} \\ \frac{V_{load}}{\beta}\Delta\dot{P}_{load} &= K_{QX}\Delta x_{fH} - K_{QP}\Delta P_{load} - K_{load}\Delta P_{load}\end{aligned}\quad (4.7)$$

where $\Delta x_H = x_{fH} - x_{fH,0}$ and $\Delta P_{load} = P_{load} - P_{load,0}$. Notice that $\Delta\dot{P}_{load} = \dot{P}_{load}$ due to the constant operating point. The equation is transformed from the time domain into s-domain using the Laplace Transform.

$$\Delta P_{load}(s) \left(\frac{V_{load}}{\beta} s + K_{QP} + K_{load} \right) - \frac{V_{load}}{\beta} \Delta P_{load}(0) = K_{QX} \Delta X_{fH}(s) \quad (4.8)$$

The system is initially at rest and therefore $\Delta P_{load}(0) = 0$ at $t = 0$. Rearranging the equation, the first order SISO transfer function is obtained which relates the HP valve position x_{fH} to the load pressure P_{load} .

$$\frac{\Delta P_{load}(s)}{\Delta x_{fH}(s)} = \frac{K_{QX} \frac{\beta}{V_{load}}}{s + (K_{QP} + K_{load}) \frac{\beta}{V_{load}}} \quad (4.9)$$

where

$$K_{QX} = C_{D,H0} D_H \pi \sqrt{\frac{2}{\rho_0} |P_{c,0} - P_{load,0}|} \cdot \text{sign}(P_{c,0} - P_{load,0}) \quad (4.10)$$

$$K_{QP} = \frac{C_{D,H0} A_{H,0}}{\sqrt{2\rho_0 |P_{c,0} - P_{load,0}|}} \text{sign}(P_{c,0} - P_{load,0}) \quad (4.11)$$

$$K_{load} = \frac{Q_{nom}}{2\sqrt{P_{nom} P_{load,0}}} \quad (4.12)$$

The 0-subscript denotes the initial condition of the respective parameters. It is seen that the transfer function is a first order system with a pole location that depends on several parameters. The pole location is highly dependent on the operation point.

Additionally, the pole location can be affected by changing V_{load} and K_{load} that indirectly contains the load orifice area. The location of the pole both determines the damping but also the settling time, i.e. the time it takes for the filter to obtain a signals DC-value.

In figure 4.5 sufficient damping was obtained when $V_{load} = 0.5[L]$ and K_{load} was a function of $P_{nom} = 200[Bar]$ and $Q_{nom} = 20[L/min]$. However, the settling time showed to be too large. These parameters could be tuned further to obtain faster response time on behalf of less damping, if this is acceptable for a given application. The intention of this report is to build a controller that can be applied for various applications. As a consequence of this, it is not desirable to restrict the demands for load that the designed controller can be applied on.

With the above analysis in mind, it is now necessary to apply digital filtering in order to obtain the average of the estimated output flow \hat{Q}_{out} .

4.4.2 Digital filtering

A low pas filter can be utilised to dampen flow ripples and therefore obtain the average output flow \bar{Q}_{out} . Low pas filtering can be obtained in several ways. The ones that will be examined in this section is a first order low pass filter, a second order Butterworth filter and a moving average filter. It is desirable to have a filter that attenuates the flow ripples sufficiently while keeping a fast settling time. The first and second order filters are derived in appendix and the results are given succeedingly using a sample time of $T_{sdf} = 1/f_{s,p} = 0.1[ms]$. The reason why $f_{s,p}$ is chosen is because the numerical differentiation in the flow estimator uses this sampling rate. In order to keep the naming convention, the sampling frequency in this section is defined as $f_{sdf} = f_{s,p} = 10[kHz]$.

First order low pas filter

The flow ripples are located at $150[Hz]$. Placing the cutoff frequency of the filter one decade before $\omega_{cut} = 2\pi \cdot 15[rad/s]$, the damping will be $20[dB]$ at the flow ripples or in nominal values it is a 90% reduction of the amplitude. A continuous-time first order filter is converted to a discrete-time filter using a bilinear transformation.

$$\begin{aligned} H_{f,1}(z) &= \frac{\omega_c(z+1)}{z\left(\frac{2}{T_{sdf}} + \omega_c\right) + \left(\omega_c - \frac{2}{T_{sdf}}\right)} \\ &= \frac{0.0046903(z+1)}{(z-0.9906)} \end{aligned} \quad (4.13)$$

Second order Butterworth filter

The Butterworth filter is also known for its flat passband region. A second order Butterworth filter gives $40[dB/dec]$ damping after the cutoff frequency. Additionally, it introduces more phase delay than a first order filter. The filter can be tuned in order to obtain a faster response time. The downside of increasing the bandwidth of the filter is that the flow ripples becomes less damped. With this in mind, the cutoff frequency is chosen to be $\omega_c = 2\pi \cdot 25[rad/s]$ which gives $31.1[dB]$ damping at $150[Hz]$ and in nominal values its a 96.8% reduction. The second order Butterworth filter is equivalent to a second order transfer function with a damping coefficient of $\zeta = \sqrt{0.5}$ and natural frequency equal to the cutoff frequency $\omega_n = \omega_c$. The filter is derived in appendix B.1, and the result is given in equation 4.14.

$$\begin{aligned} H_{f,2}(z) &= \frac{\left(\frac{\omega_c \cdot T_{sdf}}{2}\right)^2 (z^2 + 2z + 1)}{z^2 \left(1 + \frac{2\sqrt{0.5}\omega_c T_{sdf}}{2} + \left(\frac{\omega_c \cdot T_{sdf}}{2}\right)^2\right) + z \left(-2 + \frac{(\omega_c \cdot T_{sdf})^2}{2}\right) + \left(1 - \frac{2\sqrt{0.5}\omega_c T_{sdf}}{2} + \left(\frac{\omega_c \cdot T_{sdf}}{2}\right)^2\right)} \\ &= \frac{6.1004 \cdot 10^{-5} (z+1)^2}{(z^2 - 1.978z + 0.978)} \end{aligned} \quad (4.14)$$

Moving average filter

The moving average filter should at least have a window length that covers the discharge stroke between two decision instants. At a sampling rate of $10[kHz]$ there are 400 samples per period when the pump speed is $1500[RPM]$. The distance between two decision instants is 60° . Thus, the number of samples the moving average filter should be applied over is $\frac{60}{360} \cdot 400$ which is approximately 66 – 67 samples. The moving average filter is less sensitive to noise if more samples are included but this also introduces more phase delay.

$$H_{f,mvg}(z) = \frac{1}{67} \sum_{i=0}^{66} z^{-i} \quad (4.15)$$

Filter performance

The frequency response of the filters are showed in figure 4.8

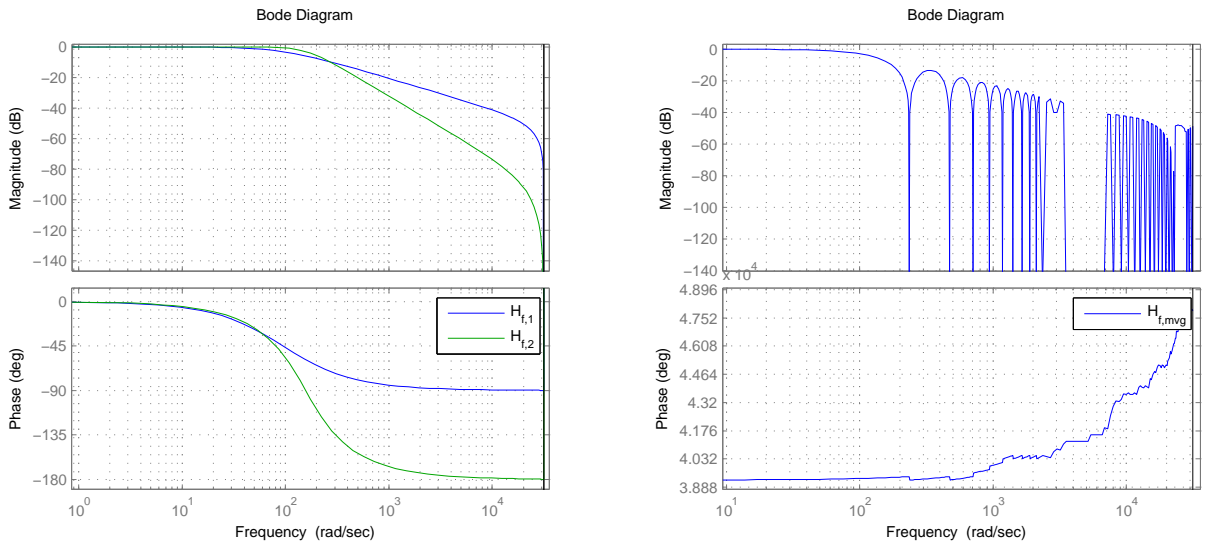


Figure 4.8: Bode plot of a first order filter $H_{f,1}(z)$, second order Butterworth filter $H_{f,2}(z)$ and a moving average filter $H_{f,mvg}(z)$ with a window size of 67 samples. The sample time is $f_{sdf} = 10[kHz]$

The three filters have low pass characteristic with a flat passband and amplitude attenuation of frequencies higher than the cutoff frequency ω_c . The moving average filter shows an extremely large phase-delay which is irrelevant in this connection because the filter is not used in the traditional sense. Here, it is only used to calculate an average value between two decision instants (input signals). If the filter was used with a window size that covered more decision instants, the phase-delay could be of interest to examine. After the cut-off frequency, the first order low pass filter dampens with $20[dB/dec]$ while the second order filter dampens with $40[dB/dec]$.

The filters are tested in simulations with various closing angles steps and applied on the estimated flow \hat{Q}_{out} . Section showed that the system response is faster for larger orifice areas. Additionally, the

analogue-filtering effects are insignificant for larger orifice areas. As a result of this, a large orifice area is chosen where $P_{nom} = 80[Bar]$ and $Q_{nom} = 16[L/min]$.

The response of the filters and the reference output Q_{out} are shown in figure 4.9. The reference value Q_{out} is obtained using a moving average filter on the actual output flow and not the predicted. A high sampling frequency of $1[MHz]$ is utilised for the reference flow and a window size is chosen that covers the period between two decision instants, i.e. 60° . See the results in figure 4.9

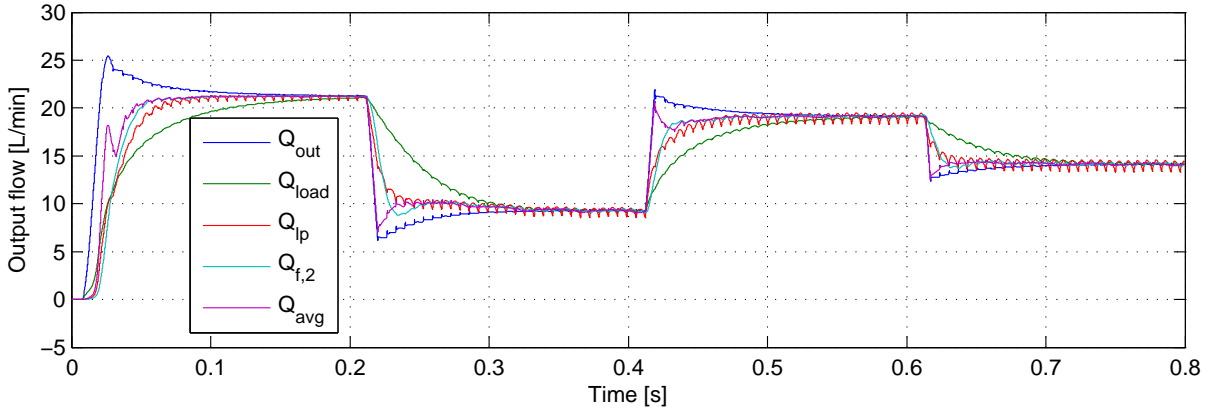


Figure 4.9: Flow filter test in simulation where the orifice area is determined based on $Q_{nom} = 16[L/min]$ and $P_{nom} = 50[Bar]$. The tested filters includes a first order and second order low pass filter and also a moving average filter along with the original output flow.

The moving average filter output \hat{Q}_{avg} gives the most accurate steady state flow response, however the transient response show oscillating behaviour compared to the other filters. The fastest transient response is observed at the moving average filter followed by the second order Butterworth filter output $\hat{Q}_{f,2}$. All filters estimates the correct output with an error margin of $2.5[L/min]$ after $0.05[s]$ after a step is applied. In the plot, it is seen that the filters converges to Q_{out} before the load flow Q_{load} . The first order low pass filter output $\hat{Q}_{f,1}$ also shows great transient and steady state response but the flow ripples are not well damped. Similar results are also obtained at other oil temperatures and orifice areas. The second order Butterworth filter is chosen as this shows well damped behavior and it shows less oscillations than the moving average filter.

In agreement with section 4.3, the filter and the estimator together are tested for variation in uncertain parameters. Again, the bulk modulus of the oil and the numerical differentiation are both over and under estimated by 20%. The results are given in figure 4.10a for deviation in β and in figure 4.10b for deviation in numerical differentiation.

The load flow is also plotted in the figures in order to compare the performance of the estimator. It is seen that the estimator shows superior performance in transient response. However, the estimator output only converges vaguely before the load flow. The best performance is observed when bulk modulus is under estimated $Q_{f,2,\beta L}$ and the numerical differentiation is over estimated $Q_{f,2,dPH}$. The reason for this is due to a constant bulk modulus value. At pressure levels below $\approx 100[Bar]$ the bulk modulus decreases, see appendix A.4. In order to compensate for this a simple approximation is utilised of the bulk modulus curve given in figure A.4b. The bulk modulus can be approximated by

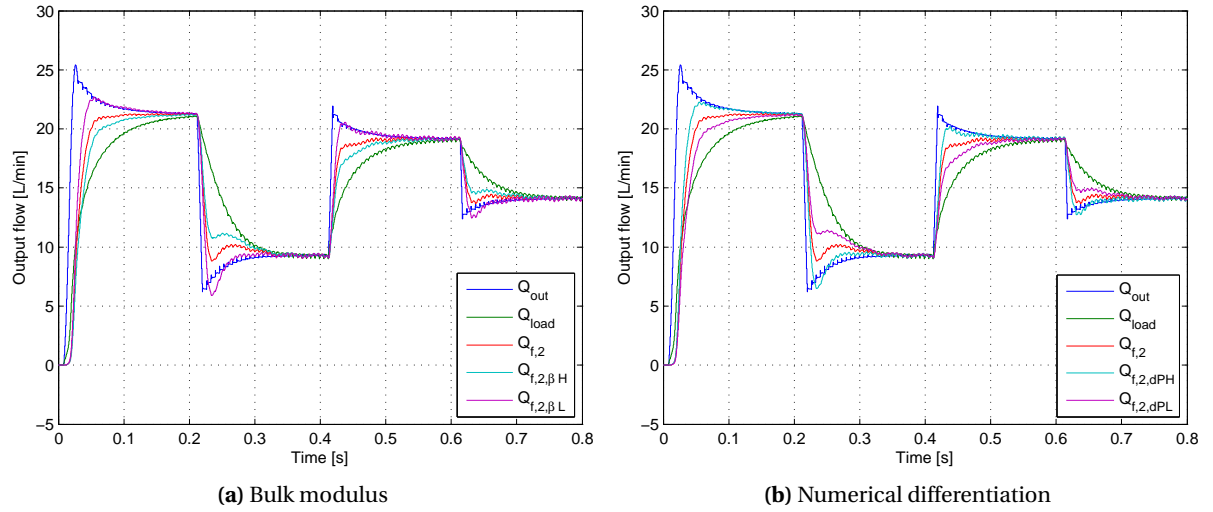


Figure 4.10: The performance of the estimator and filter (a) when bulk modulus is 20% over and under estimated and (b) when numerical differentiation is over and under estimated by 20%.

a linear increase with load pressure when $P_{load} < 100[Bar]$. The lower limit is iteratively defined as $50[Bar]$ in order to avoid under estimation of bulk modulus which causes excessive pressure spikes in the numerical differentiation. The results are shown in figure 4.11.

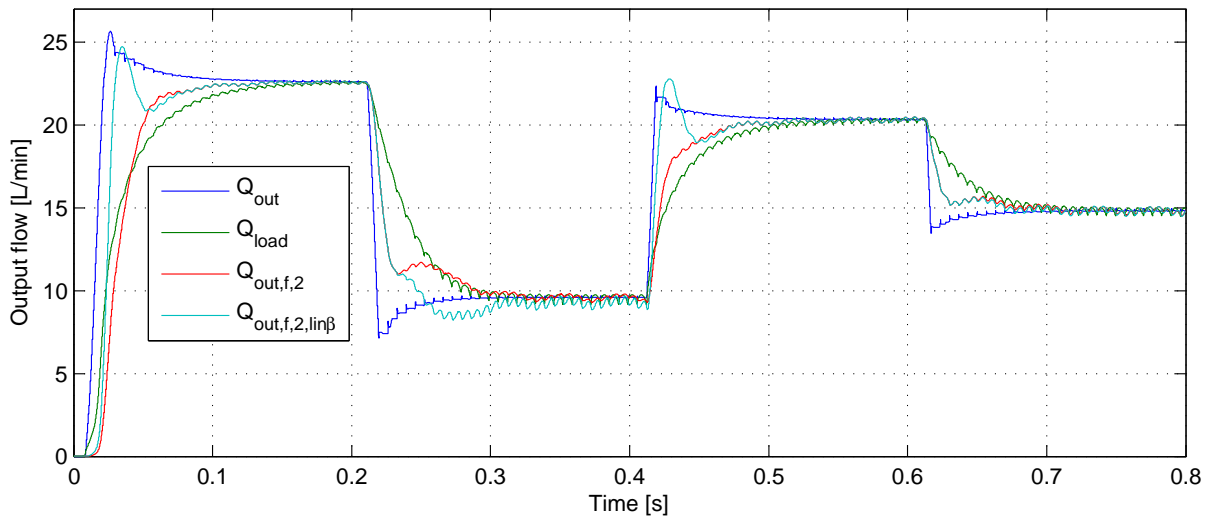


Figure 4.11: A flow filter test to compare the performance of linearly varying bulk modulus. The orifice area is determined based on $Q_{nom} = 16[L/min]$ and $P_{nom} = 50[Bar]$.

The transient response of the estimator is clearly superior when β varies linearly with P_{load} ($Q_{out,f,2,lin\beta}$). The downside of this approach is that the method introduces a new source of uncertainty, i.e. the model of the bulk modulus which is plotted in appendix A.4. However, this estimator is chosen for control design purposes due to its better transient performance. The control design can be initiated using the designed flow filter and the flow estimator in order to obtain Q_{out} .

Control of a Digital Displacement Pump

This chapter documents the design process of a flow controller for a Digital Displacement Pump. The overall task is to design a linear and closed loop flow controller that accounts for the DDP's time-delay. The designed controller is tested on the nonlinear pump model described in section 2. There exists a wide range of options to tackle the control paradigm and therefore an outline is given to describe the methods that is used in this report in order to construct the flow controller.

5.1 Method outline

The DDP is a nonlinear system that contains state saturation. Therefore, the nonlinear model is simplified by use of a linear time-invariant SISO transfer function. The linear system approximates the average output flow from six cylinders given a closing angle input θ_{cl} and a specific operation point, i.e. oil temperature T_{oil} and load pressure P_{load} . This gives access to apply linear control theory on the simplified DDP model. The closed loop controller is designed based on worst-case-damping-scenario in order to account for nonlinearities in the DDP's response.

A linear closed loop feedback controller is designed based on analysis of the DDP's transfer function by utilising partial displacement operation-mode. It is possible to identify the poles and zeros in order to analyse the stability of the system. The system is converted from continuous to discrete time to include the effects of sample and hold. Moreover, the controllers are directly designed in the z-domain using a root locus plot. The closed loop controller is designed based on worst-case-damping-scenario because DDP actually is nonlinear. As a consequence hereof, a single linear transfer function can not capture the DDP response for all operation points.

A necessity to fulfill before linear control theory can be applied is to obtain an input-output map $f(\cdot)$. This map is described in chapter 6 and used in this chapter without further remarks. Notice, the controllers loses their performance when the map deteriorates due to for instance changing oil temperatures. For instance, the map might predict a closing angle input $\theta_{cl,i} = 160^\circ$ where in fact it should have been $\theta_{cl,i} = 190^\circ$.

5.2 Simplified DDP model

The simplified DDP model is derived based on the analysis conducted in section 3. The analysis identified the following characteristics of the DDP:

- Four active cylinders was identified at a given time instant. This means that four cylinders are affecting the output flow. Giving the same θ_{cl} to four cylinders in a row, results in an instantaneous output flow Q_{out} that is solely a function of the given θ_{cl} . See more details in section 3.4.2.
- The output flow is a time variant signal for fixed θ_{cl} , T_{oil} and P_{load} . However, the average output flow is constant. This is explained in section 4.
- There is a time delay between the input/output relation for the DDP. This time delay varies nonlinearly with the θ_{cl} as well as the operation condition. See section 3.3.
- The maximum output flow rate is observed at $\theta_{cl} \approx 155^\circ$ regardless of load pressure P_{load} and oil temperature T_{oil} . The output flow is nearly identical at $\theta_{cl} \approx 160^\circ$, hence in this section the maximum output flow is defined for $\theta_{cl} = 160^\circ$. An output flow rate of $Q_{out} = 0[L/min]$ is observed for $\theta_{cl} > 220^\circ$ depending on the operation point, see appendix C for details.

5.2.1 Continuous time transfer function

A simplified DDP model can be designed based on step response analysis on the nonlinear model. The average output flow is obtained using the flow estimator and flow filter designed in chapter 4.4. In the same chapter, it was shown that a larger orifice area yielded faster system response. Since a faster system response challenges the controller more a large orifice area is chosen, i.e. $Q_{nom} = 16[L/min]$ and $P_{nom} = 80[Bar]$. This way, a worst-case-scenario principle is somehow utilised. The step responses are performed at $T_{oil} = 30^\circ C$, see the results in figure 5.1. The time-delay in the DDP results in step responses starting at different times. In order to avoid this, the time scale is offset for each step response so the flow step response start at the same time. This makes it easier to compare the performed steps inputs.

In figure 5.1a a second order transfer function fit is carried out with basis in the smallest step size. In figure 5.1b the transfer function fit is based on the largest step size. A similar test is conducted for a larger orifice area that showed to similar results, see appendix C.2 for more details.

Above analysis shows that the simplified DDP model can be designed using a delayed second order transfer function. The continuous-time transfer function of the simplified DDP is given in equation 5.1.

$$G_p(s) = G(s) \cdot e^{-s \cdot T_d} = \frac{\omega_n^2}{s^2 + \zeta \cdot \omega_n \cdot s + \omega_n^2} \cdot e^{-s \cdot T_d} \quad (5.1)$$

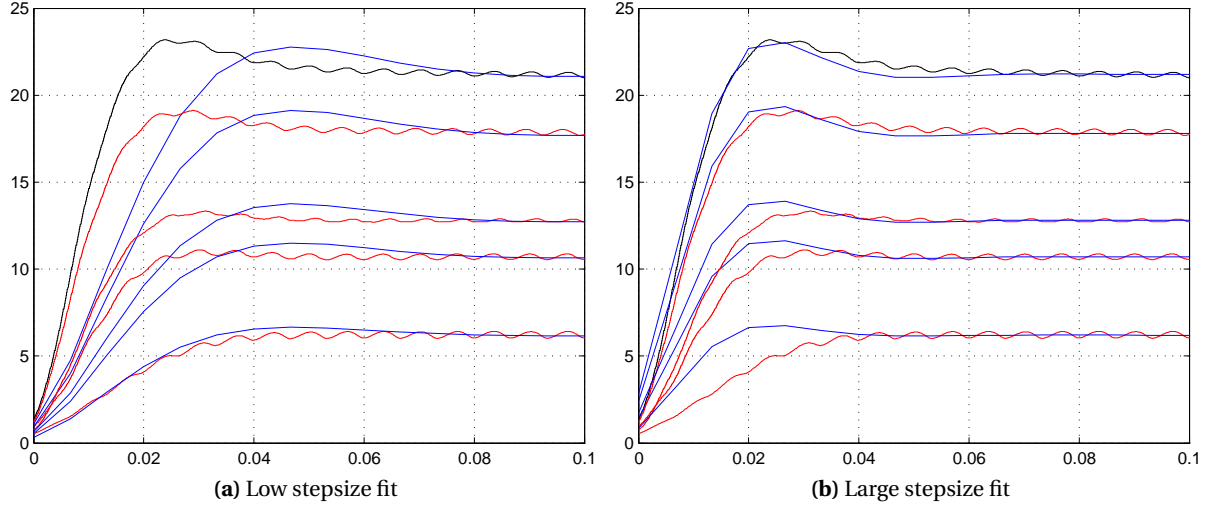


Figure 5.1: Simplified (blue) and nonlinear (red/black) pump flow response for $Q_{nom} = 16[L/min]$ and $P_{nom} = 80[Bar]$.

where T_d is the time delay that is explained in section 3.3. The transfer function is a linear time invariant SISO system. The input to the system is a desired average output flow $\bar{Q}_{out,d}$ and the output is an average output flow rate \bar{Q}_{out} . In fact, the actual input signal to the DDP is a closing angle θ_{cl} which is obtained utilising a function $f : (Q_{out,d}, P_{load}) \rightarrow \theta_{cl}$ that is derived in chapter 6. Assuming the map $f(\cdot)$ is accurate, the input to the transfer function can be considered as the desired output flow rate $Q_{out,d}$.

The input to the transfer function is bounded by $0 \leq \bar{Q}_{d,out} \leq \bar{Q}_{out,max}$ where $\bar{Q}_{out,max}$ is defined to be a function of P_{load} and $\theta_{cl} = 160^\circ$. The relation is approximately linear and the fit is given in equation 5.2, see more details in appendix C.1.

$$\bar{Q}_{out,max} = K_{qom1} \cdot P_{load} + K_{qom2} \quad (5.2)$$

where

$$\begin{array}{ll} K_{qom1} & \text{Coefficient } K_{qom1} = -0.031975 \quad [m^3/(Pa \cdot s)] \\ K_{qom2} & \text{Coefficient } K_{qom2} = 25.06 \quad [m^3/(Pa \cdot s)] \end{array}$$

Damping ratio and natural frequency

The second order transfer function is defined based on observation of the nonlinear pump models output flow response. The model is constructed based on the settling time and overshoot of the step response from which the systems natural frequency ω_n and the damping coefficient ζ is obtained. The settling time T_s and the overshoot differs for inputs with large and small flow steps. In figure 5.1, it was seen that the overshoot and T_s is larger for a larger step input. This indicates an operation point that is less damped. If the system is stable for at operation points with low damping ratio ζ ,

the system is also stable at operation points with high ζ . As a result herof, the second order transfer function is designed based on the flow response from a large step input. The natural frequency ω_n is obtained by first measuring the settling time $T_s \approx 0.04[s]$ without considering the time delay. Next, the time constant is computed based on the relation $T_s \approx 4 \cdot \tau_p$. The natural frequency can be obtained from a second order systems equivalent time constant $\tau_p = \frac{1}{\zeta \cdot \omega_n}$. Moreover, the damping ratio can be obtained by inspecting step response plots of a standard second order system Phillips and Harbor [2000, p.123]. The damping ratio and the natural frequency of the second order system is defined as

$$\omega_n = 153[rad/s] \quad (5.3)$$

$$\zeta = 0.65[.] \quad (5.4)$$

Time delay

The time delay is the time that elapses before the DDP's output flow reacts to a closing angle. The time delay T_d changes nonlinearly as a function of the oil temperature, load pressure and closing angle. In agreement with previous decision, the time-delay is defined based on a worst-case-scenario. This means that the largest observed time delay is chosen at $T = 30^\circ C$.

The time delay consist of the closing time of the LP valve and the pressurising time of the oil in the working chamber as identified in section 3.3. Additionally, the delay also consists of the length of the idle period illustrated in figure 2.8.

The LP-valve introduces approximately a constant time-delay regardless of oil temperature. The closing delay is $\approx 2.5[ms]$, see figure 3.5. This corresponds to a phase delay of $\theta_{lp,close} = 22.5^\circ$ because the pump speed is $1500[RPM]$.

As the idle period increases the output flow decreases. At some point, the output flow is barely existing, i.e. $Q_{out} > 0[L/min]$. In this case, the pressurising-time is not relevant as there is no output flow. Considering a shorter idle period results in more output flow, thus the pressurising-time starts to have an impact. Nevertheless, since the idle period decreases and the pressure delay increases the changes are assumed to be equal. A more comprehensive study could have been carried out but the implications of doing so are deemed to be insignificant.

In figure C.2, the idle period that gives $Q_{out} > 0[L/min]$ is identified as $\theta_{cl} = 280^\circ$ for $T = 30^\circ C$.

If the decision instant is defined as $\theta_{local,i} = 160^\circ$, the largest time delay becomes

$$T_d = \frac{2\pi}{\omega_{pump}} \cdot \frac{(280 + 22.5 - 160)}{360} = 15.8[ms] \quad (5.5)$$

5.2.2 Discrete time transfer function

The discrete time version of the continuous time transfer function includes a sample and hold device. This device keeps a signal steady between two sampling instants. It is used to replicate the effects of a digital filter on a continuous time system. The sampled data system of the pump along with a digital controller is shown in figure 5.2.

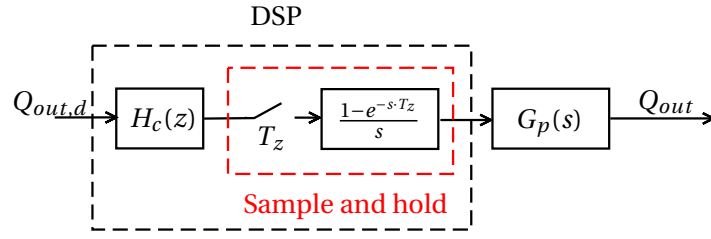


Figure 5.2: Discrete time effects on the pump system

A control signal is given every $\theta_{pump} = 60^\circ$ which is equivalent to a time delay of $T_z = 6.67[ms]$. This is defined to be the sampling time of the digital controller.

The sample and hold device is modelled using the Zero-Order-Hold (ZOH) method. The ZOH in s-domain is modelled as $G_{zoh} = \frac{1-e^{-sT_z}}{s}$ and the equivalent model in z-domain is given in equation 5.6.

$$H_{zoh}(z) = (1 - z^{-1}) \cdot \mathcal{Z} \left\{ \frac{1}{s} \right\} \quad (5.6)$$

The transfer function of the DDP needs to be discretised in order to design a controller in the z-domain. The discrete time approximation of the continuous transfer function given in equation 5.1, is derived in the following parts. Notice, the time delay is not included in the derivations as this is simply just a multiplicatoin by z^{-k} . The overall task is to perform the z-transform of equation 5.7

$$H_p(z) = (1 - z^{-1}) \cdot \mathcal{Z} \left\{ \frac{\omega_n^2}{s(s^2 + \zeta \cdot 2\omega_n \cdot s + \omega_n^2)} \right\} \quad (5.7)$$

Using a table of z-transforms from Phillips and Harbor [2000, p.652] shows that the z-transform of the following transfer function

$$\frac{a^2 + b^2}{s(s^2 + 2as + a^2 + b^2)} \quad (5.8)$$

is given by

$$\frac{z(Az + B)}{(z - 1)(z^2 - 2ze^{-aT_z} \cos(bT_z) + e^{-2aT_z})} \quad (5.9)$$

where

$$A = 1 - e^{-aT_z} \left(\cos(bT_z) + \frac{a}{b} \sin(bT_z) \right) \quad (5.10)$$

$$B = e^{-2aT_z} + e^{-aT_z} \left(\frac{a}{b} \sin(bT_z) - \cos(bT_z) \right) \quad (5.11)$$

The coefficients a and b is calculated using ζ , T_z and ω_n .

$$T = 6.7[ms] \quad (5.12)$$

$$a = \zeta \cdot \omega_n = 0.65 \cdot 153.8462 = 100 \quad (5.13)$$

$$b = \sqrt{\omega_n^2 - a^2} = \sqrt{153.8462^2 - 100^2} = 116.9 \quad (5.14)$$

Inserting the constants defined in equation 5.12-5.14 in to equation 5.10 and 5.11 gives the the following results; $A = 0.3256$ and $B = 0.2068$. Inserting all the obtained coefficient in equation 5.9 results in

$$\frac{z(0.3256z + 0.2068)}{(z-1)(z^2 - 0.7315z + 0.2639)} \quad (5.15)$$

Applying the ZOH-effects $1 - z^{-1}$ to the obtained z-transform, the final expression for the discrete DDP transfer function is obtained as

$$H_p(z) = \frac{(0.3256z + 0.2068)}{(z^2 - 0.7315z + 0.2639)} \quad (5.16)$$

5.3 Controller Structure

The chosen control structure is a combination of a feedback and feedforward controller. The feedforward controller $H_f(z)$ predict the input that is required to obtain a desired output flow by using a nonlinear input-output map $f(\cdot)$ given in equation 6.1. The feedback controller $H_c(z)$ is used to suppress modelling uncertainties and disturbances while driving the system state to a desired set-point. Traditional closed loop feedback controllers used on a system with time delay can have destabilising effects on the system. This is seen in the closed loop transfer function, see equation 5.17.

$$H_{cl}(z) = \frac{Q_{out}(z)}{Q_{out,d}(z)} = \frac{H_c(z) \cdot H_p(z) \cdot z^{-k}}{1 + H_c(z) \cdot H_p(z) \cdot z^{-k}} \quad (5.17)$$

The closed loop systems characteristic equation, given in the denominator of equation 5.17, includes the pump systems time delay. Using a Smith Predictor, this time delay can be avoided. Hereby, under ideal circumstances the Smith Predictor can improve the phase response of the system [Massimiliano, 2003].

A smith predictor is used in the feedback control loop because of the time delay of k samples in the pump system $H_p(z) \cdot z^{-k}$. The Smith Predictor is an Internal Model Controller that contains two feedback loops, see figure 5.3.

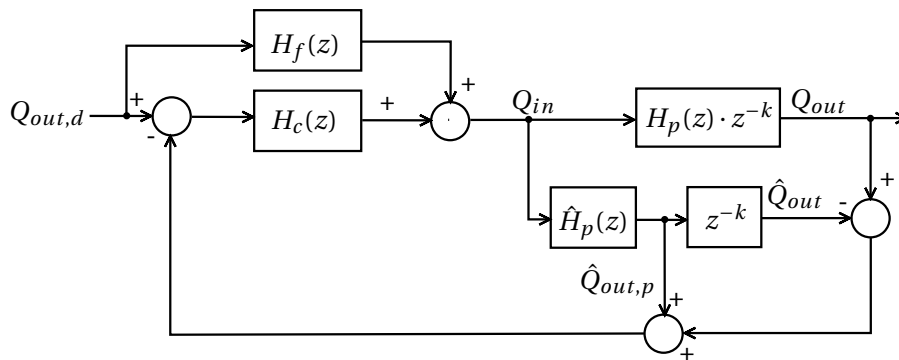


Figure 5.3: Internal Model Control utilising a Smith Predictor to adjust the closed loop feedback through predicted model output [Massimiliano, 2003].

The error signal applied to the controller $H_c(z)$ is defined as

$$e[n] = Q_{out,d}[n] - \hat{Q}_{out,p}[n] - Q_{out}[n-k] + \hat{Q}_{out}[n-k] \quad (5.18)$$

The inner loop uses a model of the pump to predict the immediate response $\hat{Q}_{out,p}$ for a given control input by disregarding the time delay z^{-k} . This is used to adjust the error signal given to the controller $H_c(z)$ before the actual response takes place. The outer loop uses the difference between the measured system response Q_{out} and the predicted system response \hat{Q}_{out} inclusive the time delay to adjust the error signal. If the predicted response and the actual response is equal, the error signal is zero and the controller does not take further actions. This is more evident when block diagram reduction is applied to figure 5.3. The inner loop is closed which results in the Internal Model Controller given in figure 5.4.

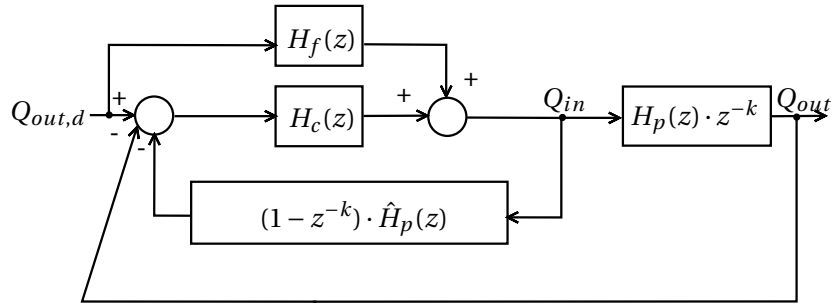


Figure 5.4: Equivalent block diagram of the Smith predictor.

The closed loop transfer function for the inner loop is given by

$$H_{cl,i}(z) = \frac{Q_{in}(z)}{Q_{out,d}(z)} = \frac{H_c(z)}{1 + H_c(z)\hat{H}_p(z)(1 - z^{-k})} \quad (5.19)$$

Applying $H_{cl,i}(z)$ as the control input to the outer closed loop by neglecting the feedforward gain, results in the following transfer function (see a detailed derivation in appendix B.2.1).

$$H_{cl}(z) = \frac{H_c(z) \cdot H_p(z) \cdot z^{-k}}{1 + H_c(z)\hat{H}_p(z) + H_c(z) \cdot (H_p(z) \cdot z^{-k} - \hat{H}_p(z) \cdot z^{-k})} \quad (5.20)$$

Here, it is seen that if the predicted model response $z^{-k}\hat{H}_p(z)$ is equal to the actual system response $z^{-k}H_p(z)$, the closed loop transfer function reduces to the following

$$H_{cl}(z) = \frac{Q_{out}(z)}{Q_{out,d}(z)} = \frac{H_c(z) \cdot H_p(z) \cdot z^{-k}}{1 + H_c(z) \cdot H_p(z)} \quad (5.21)$$

With the structure of the DDP control system defined, it is possible to design the controller.

5.4 Controller design

The design of the linear controller is based on the simplified pump model using root locus analysis in z -domain. The controller utilises the partial displacement capability of the DDP in order to minimise the flow ripples. The designed controller is validated after it has been designed and tested on the nonlinear DDP model described in chapter 2.

5.4.1 Proportional integral controller

The requirements for the controller is to obtain a fast, damped and accurate flow response. The accuracy of the flow response is measured for a step input to the linear pump system $H_p(z)$. The first step in designing a controller is to analyse the open loop transfer function of $H_p(z)$ without the time delay due to using a Smith predictor. The open loop root locus plot of $H_p(z)$ is shown in figure 5.5a. The proportional controller K_p can be defined to guarantee stable control for the simplified DDP model by using the root locus plot. In the plot, it is seen that the root locus starts from a complex conjugated pole pair at $z \approx 0.36 \pm j \cdot 36$. As K_p increases one of the poles moves towards a zero at $z \approx -0.63$ and the other towards a zero at $z \rightarrow -\infty$. For a gain up to $K_p = 3.3$, the poles remains inside the unit circle, which indicates that the system is stable. The root locus extracting from the complex conjugated pole pair indicates a system that gets more under damped for high gain. Additionally, $H_p(z)$ does not have a free integrator at $z = 1$ and can consequently be classified as a type 0 system. Notice, a free integrator $s = 0$ is mapped into $z = 1$ in the z -domain. According to the final value theorem, the lack of free integrators gives a steady state error for a step input [Phillips and Harbor, 2000, p.170]. Using a P-controller is therefore not sufficient in order to control $H_p(z)$ as it does not fulfill the requirements given initially in this discussion.

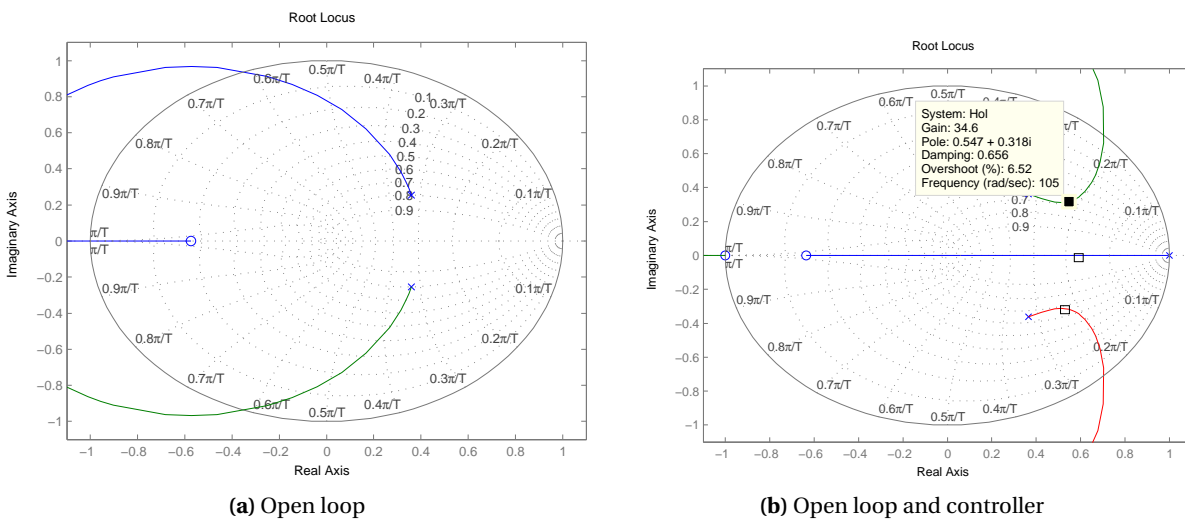


Figure 5.5: Root locus plot of the open loop discrete time system where (a) shows the open loop root loci of the pump $H_p(z)$ and (b) shows it including a PI-controller $H_p(z) \cdot H_c(z)$

A free integrator is necessary in the controller $H_c(z)$ in order to remove the steady state error for

a step input to $H_p(z)$. The free integrator introduces infinite dc gain, hence ideally it removes the steady state error for a step input. The PI-controller is tuned by using the MATLAB toolbox sisotool, which immediately shows the effects of adjusting the open loop gain. The root locus of the open loop system containing a PI-controller is shown in figure 5.5b. The gain is chosen with the intend of increasing the bandwidth of the closed loop system while keeping the system damped. This means that the dominating pole located at $z = 1$ is dragged away from the low frequency region towards $z = 0$ while keeping the complex conjugated pole pair within the region of the well damped area. Notice, this area is the elliptic shaped grid lines near the positive real axis. This results in a proportional gain of $K_p = 34$ and utilising a bilinear transform of the continuous time PI-controller $G_c = \frac{K_p}{s}$ gives

$$H_c(z) = \frac{0.1132z + 0.1132}{z - 1} \quad (5.22)$$

Usually, a PI-controller is not applied for systems where fast response is a requirement. However, in the case of the simplified DDP model the PI-controller shows to fulfill the task sufficiently. In continuation hearof, the closed loop controller is not further improvement with to instance a PID-controller. It is also possible to determine whether the PI-controller stabilises the system by looking at the bode plot of the open loop transfer function. This is given in figure 5.6a and it shows that the open loop system has a phase margin of 66.7° and a gain margin of $12.1[dB]$. As a result, the system is stable and well damped in its closed loop response. The closed loop bode plot shows that the bandwidth of the system is relatively high compared to the sampling frequency, see figure 5.6b.

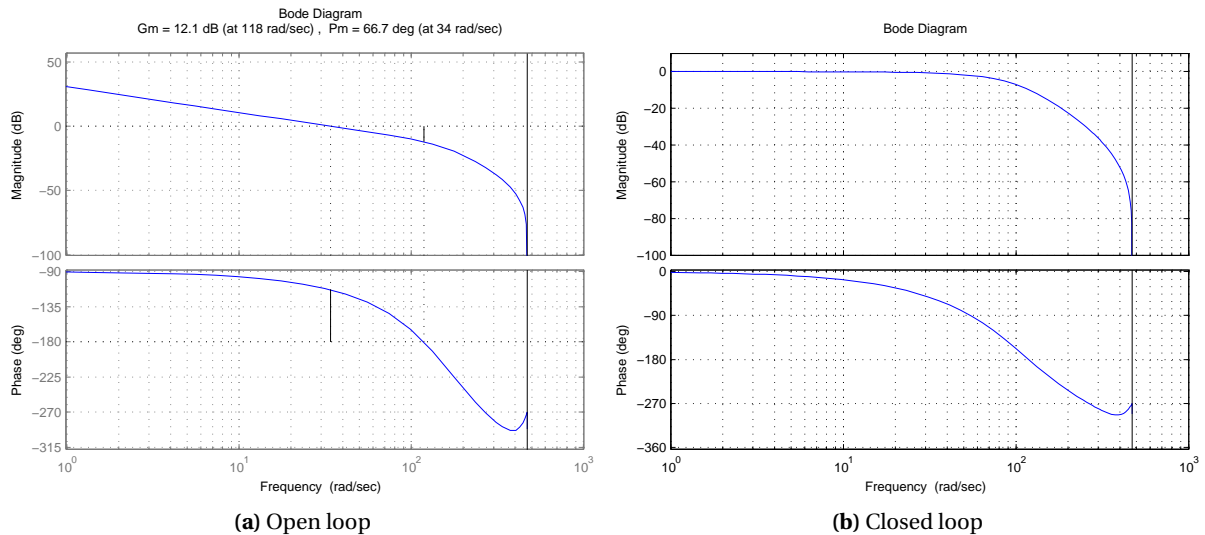


Figure 5.6: Bode plot of open loop and closed loop system of the controller $H_c(z)$ and the system $H_p(z)$

The performance of the designed controller can be examined by looking at the step response of the closed loop system that is given in equation 5.21. The step response reveals information about the rise time, settling time and the overshoot. Figure 5.7a show the step response and figure 5.7b shows the input signal to the system. The mapping function $f(\cdot)$ given in equation 6.1 is utilised to show the actual input signal. From the plot, it can be seen that the input signal stays within the $\theta_{cl} \in [160^\circ :$

$\theta_{min,flow}]$ where $\theta_{min,flow} = f(0, P_{load}) = f(0, 200[Bar]) = 313^\circ$. From the step response, it can be seen that the overshoot is less than 4%, the rise time is less than 46[ms] and the settling time is less than 90[ms].

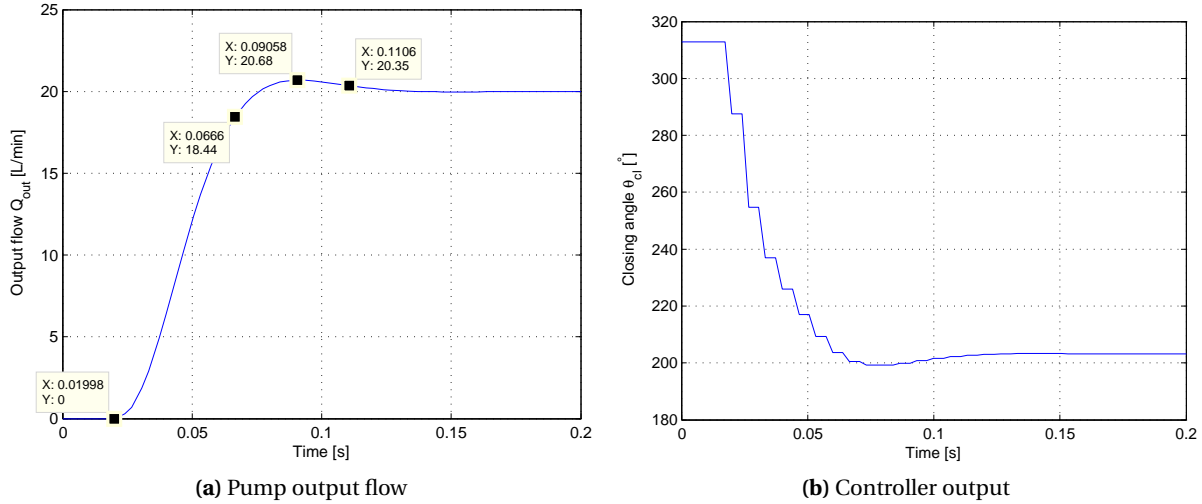


Figure 5.7: Plod of (a) step response of the linear model inclusive time-delay and ZOH effects and (b) the corresponding controller output.

From the above analysis, it is concluded that the designed controller should be able to satisfying control of the output flow when applied to the nonlinear model.

The Smith Predictor is implemented utilising equation 5.19 with $k = 3$. The results is given in equation 5.23.

$$H_{smith}(z) = \frac{0.1132z^6 + 0.0304z^5 - 0.05293z^4 + 0.02988z^3}{z^6 - 1.695z^5 + 1.056z^4 - 0.2405z^3 - 0.03687z^2 - 0.06029z - 0.02342} \quad (5.23)$$

In addition, the smith predictor can draw benefit of a feedforward gain by utilising the mapping function $f(\cdot)$. In this case, a closed-loop description can not be obtained. Instead, the controller defined in equation 5.22 is utilised along with a negative feedback gain given in equation 5.24.

$$H_{smith,fb}(z) = \frac{0.3256z^4 + 0.2068z^3 - 0.3256z - 0.2068}{z^5 - 0.7315z^4 + 0.2639z^3} \quad (5.24)$$

The closed loop controllers with and without the feedforward gains are tested on the nonlinear model, see respectively $Q_{out,ff}$ and Q_{out} in figure 5.8 for a comparison. The test consist of a flow reference step at $t = 0.5[s]$, $t = 1[s]$ and $t = 2[s]$. Additionally the step consist of a decrease in orifice area at $t = 1.5[s]$ of 75% from $Q_{nom} = 20[L/min]$ to $Q_{nom} = 5[L/min]$ at $P_{nom} = 50[Bar]$. The operation points deviates from which linear control is designed and therefore figure 5.8 and 5.7a can not be compared directly.

The step at $t = 1.5[s]$ is essentially a step that changes the load pressure. It is seen that the flow controller is capable of correcting the output flow within 100[ms]. It is seen that the controller with feedforward gain generally performs better. However, the step at $t = 1[s]$ shows more overshoot than

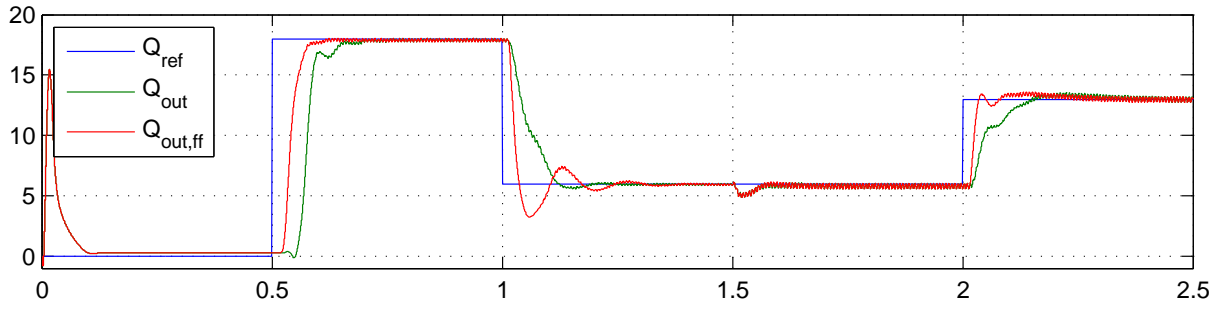


Figure 5.8: Comparison of smith predictor with ($Q_{out,ff}$) and without (Q_{out}) a feedforward gain applied on nonlinear pump model.

expected. This indicates that either the mapping function $f(\cdot)$ is not sufficiently accurate or operation point where the damping is lower than the ones indicates in appendix C.2. This uncertainty in parameters results in over design of the gains for the PI controller. Decreasing the proportional gain K_p would lower the bandwidth of the closed loop system and most likely increase the damping. The controller will not be tuned further, instead focus is pointed towards increasing the accuracy of the map $f(\cdot)$. The map is known to change with the oil temperature (see section 3.4.1) and this is another reason for pointing focus towards the map. To illustrate how the changing temperatures affects the mapping function, thus also the performance of the controller, a test is conducted where $T_{oil} = 20^\circ C$, $T_{oil} = 30^\circ C$ and $T_{oil} = 70^\circ C$. See figure 5.9.

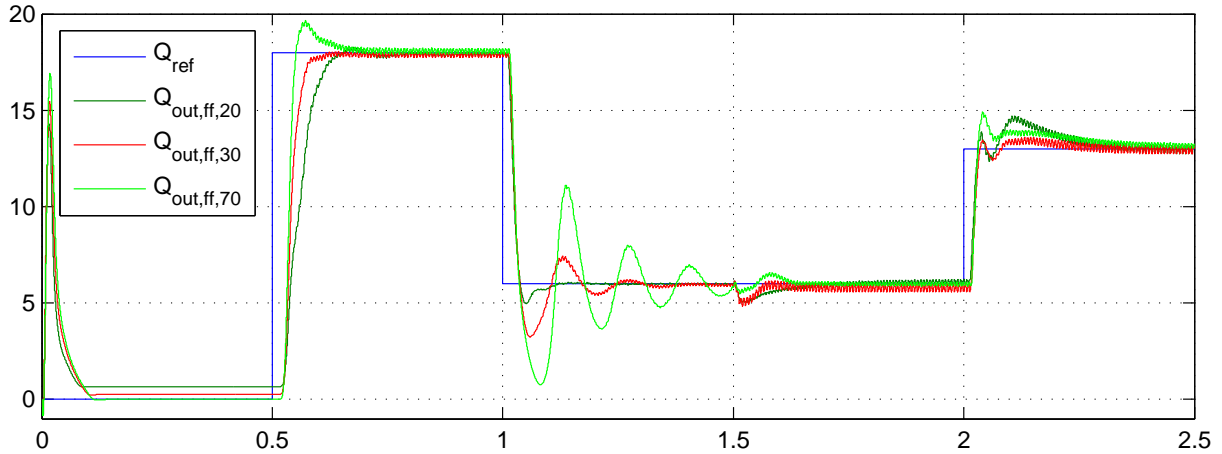


Figure 5.9: The performance of the smith predictor with feedforward gain for different oil temperatures. The controller is tested with the $T = 20^\circ C$, $T = 30^\circ C$ and $T = 70^\circ C$. Test conducted on nonlinear pump model.

Notice, both the mapping function $f(\cdot)$ and the controller is designed for $T = 30^\circ C$. The performance is clearly superior at $T = 30^\circ$ depicted in $Q_{out,ff,30}$ for most step inputs except at the step at $t = 1[s]$ for reasons explained previously. From the above analysis, it can be concluded that it is necessary to make the controller less sensitive towards temperature changes by increasing the accuracy of the mapping function.

Mapping function

The mapping function describes the input-output relation for the DDP which is sensitive towards changing oil temperatures. Initially, an input-output map is designed based on simulation of the nonlinear model. Hereupon, several polynomial regressions are applied and a polynomial chosen by considering a high accuracy and a low number of coefficients. The map is only accurate if the model captures the actual pump response precisely. Since this can not be expected in reality, possible methods to adapt the map are explored and developed in this chapter. Finally, the developed algorithms are tested and compared on the nonlinear model DDP.

6.1 Polynomial regression

A multivariate polynomial regression of the input-output data obtained from simulation is performed using the Matlab toolbox Surface Fitting Tool. Regression is applied on polynomials of different order and the polynomials are compared on their coefficient of determination r^2 (an r^2 value close to 1 indicates a better fit).

The data is obtained for an oil temperatures of $T_{oil} = 30^\circ$. The map utilises the following variables; the closing angle θ_{cl} , the output flow Q_{out} and the load pressure P_{load} .

The most accurate fit is observed when polynomial regression is applied on Q_{out} as a function of the other variables. Despite the great accuracy this approach is not chosen, as it is more practical to obtain θ_{cl} as a function of the other variables. The reason for this is due to θ_{cl} being the input signal to the DDP.

Figure 6.1a shows the resulting coefficient of determination r^2 for a range of polynomials where regression is applied. The name *Poly52* indicate a 5th order polynomial in P_{load} and a 2nd order polynomial in Q_{out} .

In the plots of figure 6.1a it is seen, that a higher order polynomial gives a better r^2 . This can indicate that the data is over fitted, but inspecting a plot of the polynomials reveals a smooth surface fit. The best fit on average considering all the temperatures $T_{oil} \in [20^\circ C : 70^\circ C]$ is the Poly55 polynomial. The disadvantage of using Poly55, is that it has 21 coefficients. This gives 21 degrees of freedom in an

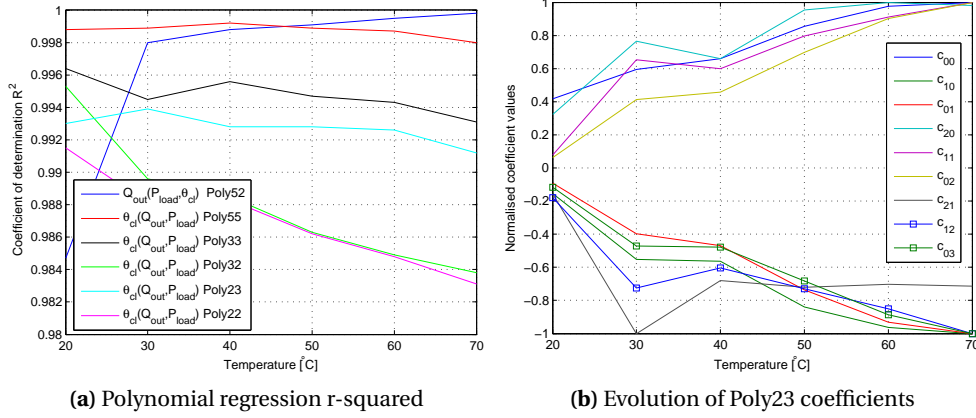


Figure 6.1: The results of the polynomial regression where (a) shows the coefficient of determination as a function of oil temperature for multiple polynomial fits and (b) the evolution of the coefficient for a single polynomial fit

optimisation problem. Another good fit is Poly23 that only has 9 coefficients and still an accuracy above $r^2 > 0.99$.

A plot of how the coefficient in Poly23 evolves for changing oil temperatures is shown in figure 6.1b. The coefficients are normalised by their respective maximum absolute values because some values are above hundreds and others below one. The coefficients follows a smooth path for $T \in [30^\circ : 70^\circ]$. The pattern is interrupted in the temperature range $T \in [20^\circ : 30^\circ]$.

A Poly23 regression that is valid for $T = 30$ is given in equation 6.1 for a single cylinder output flow. This means that a flow reference of for instance $20[L/min]$ is divided into $20/6[L/min]$. Thus, each cylinder contributes with their part to generate a flow of $20[L/min]$ with minimum flow ripples. This is also known as the partial displacement operation mode.

$$\begin{aligned}
 \theta_{cl} &= f(P_{load}, Q_{out}) \\
 f(P_{load}, Q_{out}) &= c_{00} + c_{10} \cdot P_{load} + c_{01} \cdot Q_{out} + c_{20} \cdot P_{load}^2 + c_{11} \cdot P_{load} \cdot Q_{out} \\
 &\quad + c_{02} \cdot Q_{out}^2 + c_{21} \cdot P_{load}^2 \cdot Q_{out} + c_{12} \cdot P_{load} \cdot Q_{out}^2 + c_{03} \cdot Q_{out}^3 \quad (6.1)
 \end{aligned}$$

where the values of the coefficients are given in table 6.1.

c_{00}	c_{10}	c_{01}	c_{20}	c_{11}	c_{02}	c_{21}	c_{12}	c_{03}
286.7	-0.1388	-37.58	$4.684e-005$	0.1119	10.89	-0.0001786	-0.03304	-2.131

Table 6.1: Polynomial coefficients

Even though the polynomial shows promising accuracy, in figure 5.9 it was seen that the flow response resulted in an unexpected overshoot at some operation points ($Q_{out,ff,30}$). The results indicate that a higher order fit is necessary in order to increase the accuracy of the map. Nevertheless, Poly23 is a

starting point from which adaptation of the mapping function can be performed. Possible methods to perform adaptation is examined in the following part.

6.2 Adaptation of the mapping function

Correct sample data from the DDP is a necessity in order to perform adaptation of the mapping function. This means that a sample can only be taken in steady state, i.e. when the set-point reference and the output flow is equal. A sample can most often be taken every 250[ms] when considering the response in figure 5.9. Consequently, there is not an abundance of sample data to utilise in the adaptation algorithms. The developed approaches aims to takes this into consideration in order to obtain acceptable convergence rates.

Initially, an offset method is introduced as the simplest approach to perform adaptation. This is followed by an approach that utilises optimisation theory. Finally, both methods are tested on the non-linear model and their results are compared.

6.2.1 Adaptation by offset

The simplest approach is to take basis in the map already defined in equation 6.1. The entire map can simple be offset if it is assumed that the characteristics captured at $T_{oil} = 30^{\circ}C$ is preserved for all temperatures. Previous simulations showed that this was not the case, see for instance figure 3.8 in chapter 3. However, it is believed that the error is reduced by applying the offset. The offset method is illustrated in figure 6.2

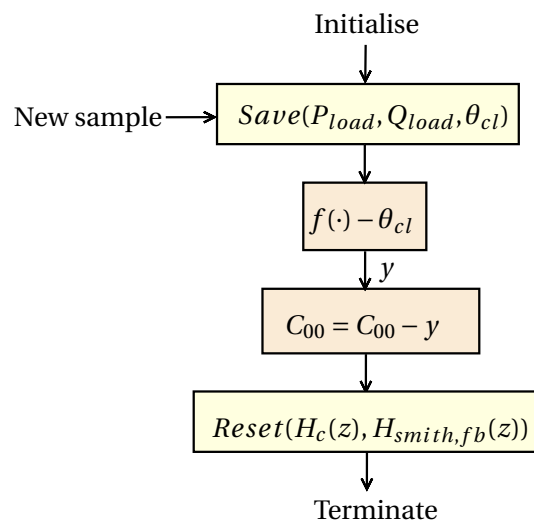


Figure 6.2: Offset algorithm to adapt the polynomial mapping function.

First, a sample of θ_{cl} , Q_{out} and P_{load} is taken when the output flow reaches a steady state value. Next, the mapping function is utilised in order to obtain the estimated $\hat{\theta}_{cl} = f(\cdot)$ at the operation point

where the measurement is taken. The difference between the estimated and the actual θ_{cl} is defined as an error. The error is used to offset coefficient c_{00} in the mapping function. finally, the controller $H_c(z)$ and the negative feedback gain from the smith predictor $H_{smith,fb}(z)$ is reset.

The feedforward gain predicts the correct θ_{cl} for the specified operation points after the adaptation method has been performed. This is the reason why a rest of the controller and feedback gain is necessary.

6.2.2 Adaptation by convex optimisation

A convex optimisation problem is formulated in order to adapt the mapping function $f(\cdot)$ given in equation 6.1. The general form of the optimization problem can be presented as

$$\underset{\vec{c}}{\operatorname{argmin}} \sum_{i=0}^n (f(\vec{x}_i, \vec{c}) - \theta_{cl,i})^2 \quad (6.2)$$

where $\vec{x}_i = [P_{load,i} \ Q_{out,i}]^T$, n is the number of samples and \vec{c} is the coefficient of the mapping function. The idea is to minimise a convex cost function $\epsilon = \sum_{i=0}^n (f(\vec{x}_i, \vec{c}) - \theta_{cl,i})^2$ based on measurement data by adjusting the argument \vec{c} . Ultimately, when the optimisation problem is solve, the set of measured values $\theta_{cl,i}$ is in coherence with the set of predicted output $f(\cdot)$ values.

The steepest descent algorithm can be used to solve the optimisation problem. However, the steepest descent algorithm is a local-minimum solver. If the steepest descent algorithm guides the coefficients towards a local minimum, the algorithm does not include any features to move away from this minimum and search for a global minimum.

In order to reach the global minimum, it is essential to have a rich set of samples. This means that it is necessary to excite a wide range of operation points. In case this is not possible, the accuracy of the mapping function $f(\cdot)$ most likely becomes biased towards a small domain containing the sample points.

The number of samples that can be obtained from the DDP depends on how often a step input is given to the pump. This depends largely on the application where the pump is utilised. Assuming a step input is given every $t = 0.5[s]$ as in the test of figure 5.9, the number of samples are 5 in a time span of 2.5[s]. The cost function is defined based on these samples which indicates that $n = 4$ in equation 6.2.

To initialise the optimisation algorithm, five samples are obtained from the polynomial map given in equation 6.1 with the intention of exciting a wide range of operation points. The collected data points are given in table 6.2.

	$P_{load,i}[Bar]$	$Q_{out,i}[\frac{L}{min}]$	$\theta_{cl,i}[^\circ]$
1	100	3.33	185
2	400	2.08	164
3	200	2.5	198
4	300	1.33	219
5	250	0.83	238

Table 6.2: Samples points from mapping function based on $T_{oil} = 30^\circ C$

The algorithm to perform optimisation is illustrated in figure 6.3.

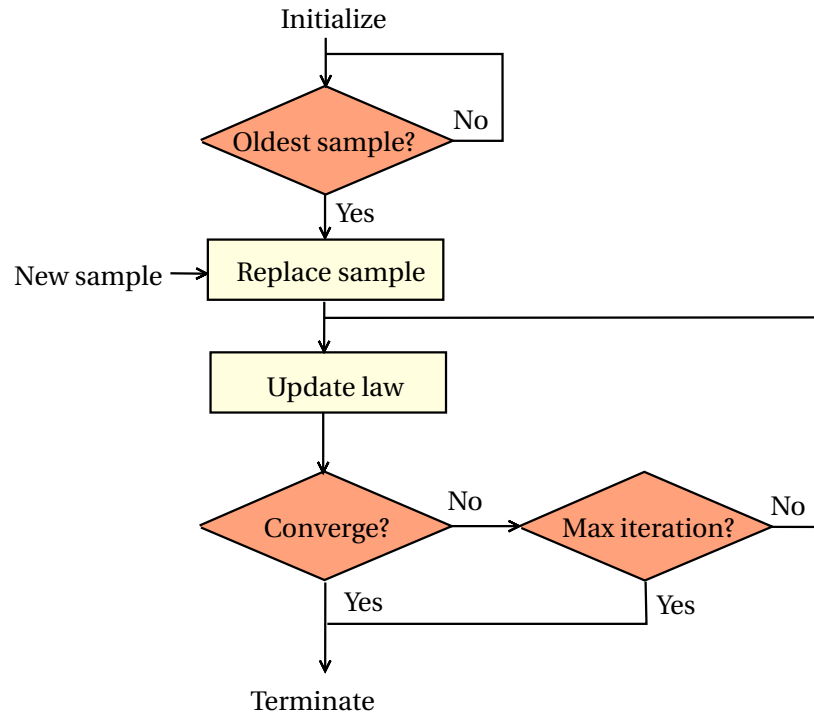


Figure 6.3: Optimisation algorithm to adapt the polynomial mapping function.

First, a sample data is taken when the output flow reaches a steady state value. Next, the oldest sample among the five is identified. The new sample replaces the oldest sample. The steepest descent algorithm is initiated in the update law that iterates until convergence is reached or an iteration-limit is exceeded.

A reset of the controller and feedback gain is not utilised in this algorithm because an exact solution most likely does not occur. The steepest descent algorithm to be implemented on the DDP is given as

$$\vec{c}^{n+1} = \vec{c}^n - \mu \nabla_{\vec{c}} \epsilon \quad (6.3)$$

where μ is the learning rate. The interpretation of this algorithm is that by moving in small steps in the opposite direction of the gradient of the error, eventually the minimum error value is reached.

In order to evaluate the algorithm, first the gradient must be found. Taking the gradient of the cost function ϵ with respect to \vec{c} gives,

$$\nabla_{\vec{c}[j]} \epsilon = 2 \sum_{i=0}^n \{(f(\vec{x}_i, \vec{c}) - \theta_{cl,i}) \cdot \vec{u}_i[j]\} \quad (6.4)$$

where $\vec{u}_i = [1 \ P_{load,i} \ Q_{out,i} \ P_{load,i}^2 \ P_{load,i} \cdot Q_{out,i} \ \dots \ Q_{out,i}^3]^T$ which is defined based on the mapping function, see equation 6.1. Inserting the gradient into equation 6.3 gives the final update law of the coefficients.

$$\vec{c}^{n+1} = \vec{c}^n - 2\mu \sum_{i=0}^n \{(f(\vec{x}_i, \vec{c}) - \theta_{cl,i}) \cdot \vec{u}_i\} \quad (6.5)$$

Since the power of some of the element in \vec{u} differs by more than a factor 100, the normalised version of the update law is utilised. This update law normalises by the power of the signal which gives

$$\vec{c}^{n+1}[j] = \vec{c}^n[j] + \frac{2\mu \sum_{i=0}^4 \{(f(\vec{x}_i, \vec{c}) - \theta_{cl,i}) \cdot \vec{u}_i[j]\}}{u_0[j]^2 + u_1[j]^2 + u_2[j]^2 + u_3[j]^2 + u_4[j]^2} \quad (6.6)$$

The normalisation is inspired from the Normalised Least Mean Square algorithm that applies to linear filters [Valin and Collings, 2007]. The convergence rate heavily depends on the learning rate μ . The learning rate is chosen iteratively based on convergence speed considerations. A Poly23 fit at $T_{oil} = 30^\circ\text{C}$ is used as the initial polynomial. Five arbitrary samples are chosen from a Poly23 fit at $T_{oil} = 70^\circ\text{C}$ to test the update law. A learning rate of $\mu = 0.1$ gave the convergence results shown in figure 6.4.

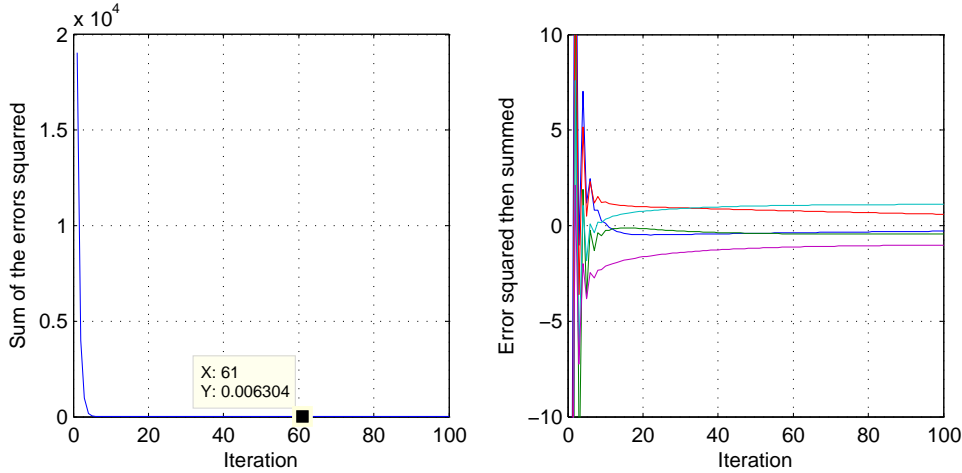


Figure 6.4: Convergence of the optimisation method where the mapping function is initialised at $T_{oil} = 30^\circ$ and data is obtained from $T_{oil} 70^\circ$. (a) shows the convergence rate for the sum of the errors and (b) shows the evolution of the errors for each of the 5 data points.

In the figure 6.4a, it is seen that the sum of the errors squared, which is equivalent to ϵ , is minimised after approximately 10 iterations. However, the coefficient are still tuning vaguely after 50 iterations. The errors does not converge towards zero, and some errors in fact increases after reaching the zero

error line. This indicates that a local minimum is reached and not a global minimum. Since, the optimisation method is carried out every time a new sample is taken it is plausible that Poly23 will converge towards a new local minimum at the next sample.

Due to the convergence of the coefficients, the algorithm is deemed valid to be tested on the nonlinear model with the specified learning rate.

6.3 Comparison of adaptation methods

A test is conducted in order to compare the proposed adaptation methods of the mapping function. Before the proposed algorithms are tested, a Poly23 fit is initially tested on the nonlinear model where the coefficients are tuned for 30°C and 70°C. See the results in figure 6.6. Notice that the oil temperature is defined as $T_{oil} = 70^\circ$ in the simulations.

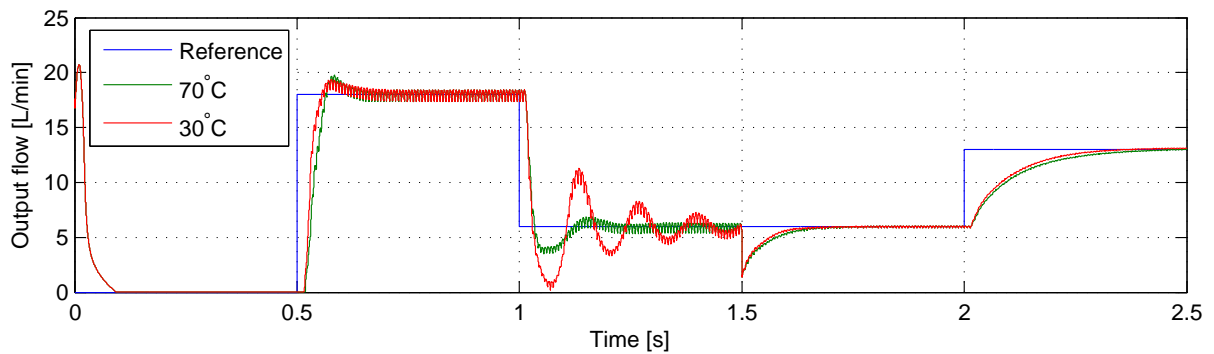


Figure 6.5: In the simulations the oil temperature is $T_{oil} = 70^\circ$. A poly23 fit is utilised where the coefficients are tuned for respectively a temperature of $T_{oil} = 30^\circ$ and $T_{oil} = 70^\circ$.

In the plot, it is seen that by tuning the coefficient of a Poly23, it is possible to obtain good response at $T_{oil} = 70^\circ C$. It is therefore deemed acceptable to test the algorithms in the nonlinear model. In order to do so, the same input signals are used as in figure 5.9. The results from the offset method and the optimisation method is given in figure 6.6.

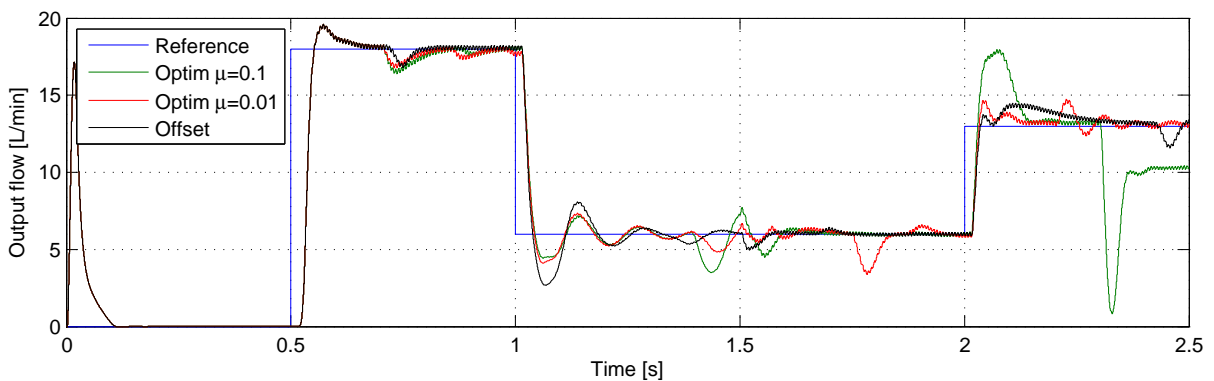


Figure 6.6: Adaptation of the mapping function that is initialised for $T_{oil} = 30^\circ$ but the simulations are carried out for an oil temperature of $T_{oil} = 70^\circ$. The offset-method and the optimisation-method is illustrated, where the later learning rate of optimisation-method is tuned to $\mu = 0.01$.

The offset-method shows promising results but with relatively large oscillations at the $t = 1[s]$ step input. Additionally, the offset method clearly overestimates the input signal at the $t = 2[s]$ step input. The output flow is offset from the steady state value for a longer period.

The solution of the optimisation-method with $\mu = 0.1$ diverges after $\approx 2[s]$. This shows that it is important to tune the learning rate correctly. By gradually decreasing the learning rate, a value was found to be $\mu = 0.01$ that gave satisfying results. The lower learning rate attenuates the large oscillations compared to the offset method. Considered the step at $t = 1[s]$ and $t = 2[s]$. However, the method introduces more flow ripples which could indicate that the map is biased towards recent sample data.

Some of the flow ripples can be explained by the way the optimisation algorithm is constructed. Each time a steady state value is approached, the optimisation algorithm is initiated. This causes the coefficient to change as well as the feedforward input. The immediate effect of this, is that the output flow makes a sudden decline or incline in its flow response. It is therefore necessary to revise the algorithm in order to avoid excessive adaptation.

The evolutions of the Poly23 coefficients during adaptation are plotted in figure 6.7.

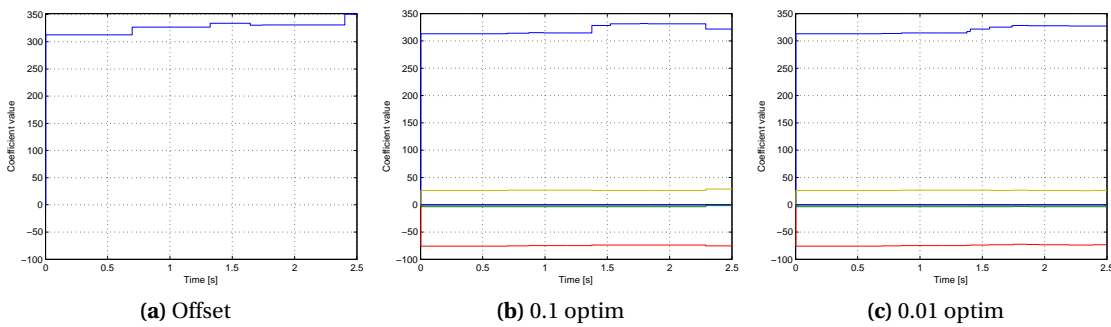


Figure 6.7: Evolution of the coefficients as a result of the step response given in figure 6.6. (a) The offset-method, (b) the $\mu = 0.1$ optimisation method and (c) the $\mu = 0.01$ optimisation method is illustrated.

The only evident coefficient is $c_{00} > 300$ in all three plots. Comparing this coefficient between the adaptation methods, it is seen that the coefficient follows a smooth path in both the offset method and the optimisation method where $\mu = 0.01$. This is not the case for the overly tuned optimisation method, see the evolution of the coefficients in figure 6.8b. Here the jumps are more rapid and sudden, clearly a new local minimum is found that causes instability and divergence.

The evolution of the remaining coefficients can be revealed by looking at the normalised plots which is given in figure 6.8

This figure shows that the coefficient c_{20} evolves mostly during the adaptation process, while the other coefficient does not change more than 20%.

In overall, the optimisation method shows most promising results but the offset method does also give acceptable results. However, there is mostly room for improvement in the optimisation method. The benefits of using such an approach is the large set of tools that can be adjusted in order to make the algorithm more efficient. To mention some of the possibilities, the number of sample points

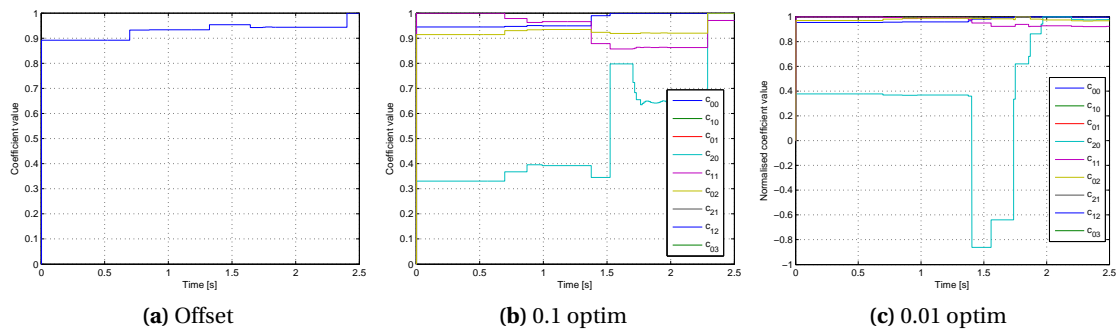


Figure 6.8: Normalised evolution of coefficients as a result of adaptation based on figure 6.6. (a) The offset-method, (b) the $\mu = 0.1$ optimisation method and (c) the $\mu = 0.01$ optimisation method is illustrated.

could be increased, the learning rate tuned and the cost function could even be defined differently. The limited time frame of the project did not permit time to tune the optimisation algorithm further.

Conclusion

7

The aim of this project has been to design a flow controller for the Digital Displacement Pump (DDP) that is stable regardless the oil temperature and load pressure.

In order to fulfil this goal, a nonlinear model of the DDP was developed and verified by using measurement data from an existing prototype. The model showed to be in good agreement with the flow characteristics measured from the prototype. To further improve the model, oil parameter variations were included to determine the impact of the temperature changes. This gave access to test the performance of the designed controller at different oil temperatures.

Furthermore, the nonlinear model was intensively analysed in order to determine the input signal to the DDP. This was carried out by considering the DDP's energy efficiency and the DDP's output power. Even though the full-displacement operation mode showed to be most energy efficient, the partial-displacement operation mode was selected because it reduces the output flow ripples. In that way, the output flow from the DDP could be controlled more accurately. Moreover, it gave access to identify an input-output map of the DDP during online operation. The pump has been operated at 1500[RPM] based on the DDP's volumetric efficiency. At this speed the maximum output power has been documented to be 11.4[kW] at 500[Bar] load pressure and 13.7[L/min] output flow.

Based on the analysis, it was shown that the output flow from the DDP contains high frequency flow ripples. Limitations in the flow-sensor bandwidth entailed a development of output flow estimator. Even though the estimator is sensitive towards uncertainty in parameters such as the oil bulk modulus, the benefits from using it were noticeable. A second order Butterworth Filter has been designed to obtain the average value of the estimated output flow. This gave access to apply negative flow feedback in the control design.

The time delays in the DDP were explored from which a simplified, linear DDP model was built. The model approximates the average output flow originating from multiple cylinder outlets. By using this, an Internal Model Controller has been designed that uses a PI-controller and a Smith Predictor. The PI-controller has been used to remove the steady-state error completely for a flow reference step-input. The Smith Predictor has been utilised to improve the phase response of the DDP by accounting for its time-delay. Furthermore, the flow controller has been shown to be able to compensate for load pressure variations. The closed loop response showed large rise time. To increase the rise time,

without destabilising the closed loop system, a feedforward gain has been utilised. This initiative improved the performance of the controller.

A requisite that gave access to apply linear control theory was the development of an input-output map that predicts the behaviour of the DDP. This map has been developed based on the nonlinear model for the oil temperature of 30°C using polynomial regression. Unfortunately, when the temperature changes the accuracy of the map degrades to the point where the linear controller is oscillating heavily. To compensate for the temperature changes, adaptation methods has been applied on the map. The first method that was developed, applies an offset to the polynomial based on the prediction error. The results from this approach was acceptable but the approach was not capable of reducing the oscillations sufficiently. For that reason, a second method has been developed using optimisation theory. A normalised version of the steepest descent algorithm is applied on a cost function that minimises the prediction error by adjusting the coefficients of the polynomial. This method showed promising results for a learning rate of $\mu = 0.01$. However, it was deemed necessary to revise the algorithm in order to avoid excessive adaptation.

7.1 Future Work

The aim of this section is to point out the initiatives that could further improve the research conducted in this report. Four main subjects has been treated in this report: modelling, estimation, control and optimisation. The modelling and prototype development is used interchangeably because prototype development would be based on a model. Each subject will be examined succeedingly.

The nonlinear model of the DDP showed large back-flow through the passive HP valve. This could be improved by utilising an active HP valve to close the valve at optimal points. This way, the DDP's output power capability could be improved further.

The estimator was highly sensitive towards the accuracy of bulk modulus and numerical differentiation. The estimator could be further improved by making it less sensitive towards these uncertain parameters. This could for instance be applied by using adaptive control theory to tune the parameters or nonlinear state observer.

The controller was designed considering the worst-case-damping-scenario. However, the worst-case was not identified and therefore research on identifying this could be conducted. Based on this knowledge, a robust controller could be designed to guaranteed stability naturally on the expense of the flow performance. Gain-scheduling is another interesting controller that could be explored in order to avoid a decrease in performance and design optimal gains for different operation points.

The most obvious area of research is exploring different optimisation algorithms to be applied on the mapping function. Especially, global optimisation techniques could make the coefficients converge to their optimal values. This technique could also be applied on a more accurate mapping function, i.e. by increasing the order of the polynomial. Finally, another obvious research subject is Neural Network which is an universal function approximator that can estimate a map with arbitrary precision.

Model Theories



A.1 Orifice Equation

An orifice is a decrease of area along a fluid path that alters the potential and kinetic energy of the fluid, see figure A.1 as a reference. The flow is separated into laminar and turbulent regions. The laminar flow is streamline, parallel and in-order paths, while turbulent flow is circular, un-ordered and swirly paths. The upstream particles are accelerated into the narrow path of the orifice with the area A_0 past the smallest stream area, *vena contracta* A_2 , to the downstream flow where the effects of the orifice is no longer present.

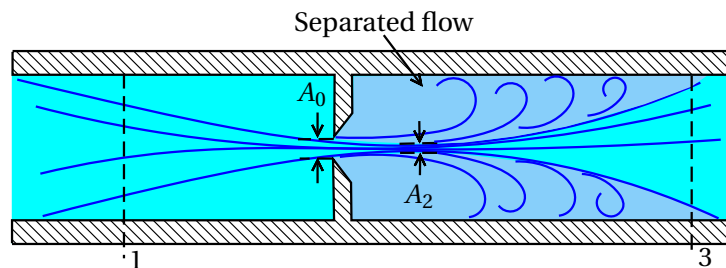


Figure A.1: An illustration of an orifice restriction along a fluid path. [Andersen, 2003, p.21]

To analyse the relation between the upstream flow at point 1 and the flow at vena contracta at point 2 Bernoulli's Equation is introduced which is valid along a streamline of a steady, incompressible and inviscid fluid. This equation states that the sum of the kinetic, potential and pressure energies is constant at any arbitrary point along a streamline.

$$\frac{u_1^2}{2} + Gz_1 + \frac{P_1}{\rho} = \frac{u_2^2}{2} + Gz_2 + \frac{P_2}{\rho} \quad (\text{A.1})$$

where

$u_{1/2}$	Fluid velocity at point 1 or 2	$[m/s]$
G	Gravitational acceleration	$[m^2/s]$
ρ	Fluid density at all points along the streamline	$[kg/m^3]$
$P_{1/2}$	Pressure at point 1 or 2	$[Pa]$
$z_{1/2}$	Pizometric head at point 1 or 2	$[m]$

Assuming the streamline is horizontal, the potential energy on both sides of the equation becomes equal. Therefore, the gravitational forces are neglected in the following deriviations. Using this assumption on equation A.1 and solving for the fluid velocities gives the following result. [?, p.99-101]

$$u_2^2 - u_1^2 = \frac{2}{\rho} (P_1 - P_2) \quad (A.2)$$

The principle of mass conservation is used to isolate the fluid velocity u_2 in equation A.2, see figure A.2.

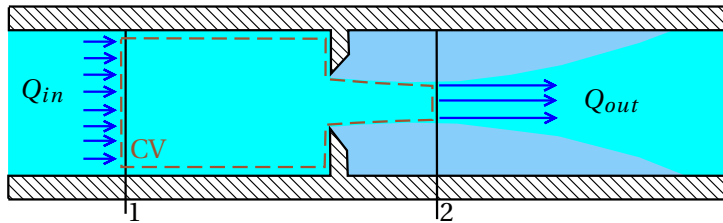


Figure A.2: Conservation of mass for an incompressible fluid in an orifice [Fox et al., 2010, p.359]

Under the previous assumptions, the inlet mass in a given control volume is equal to the outlet mass.

$$\sum_{CS} \vec{V} \cdot \vec{A} = 0 \quad (A.3)$$

$$A_1 u_1 = A_2 u_2 \quad (A.4)$$

Combining equation A.4, equation A.2 and the fact that flow is given as $Q = Au$ results in a *theoretical orifice equation*. [Munson et al., 2010, p.118-120]

$$u_2^2 - \left(\frac{A_2}{A_1} u_2\right)^2 = \frac{2}{\rho} (P_1 - P_2)$$

$$u_2^2 \left(1 - \left(\frac{A_2}{A_1}\right)^2\right) = \frac{2}{\rho} (P_1 - P_2)$$

$$u_2 = \frac{1}{\sqrt{1 - \left(\frac{A_2}{A_1}\right)^2}} \sqrt{\frac{2}{\rho} (P_1 - P_2)}$$

$$Q_2 = \frac{A_2}{\sqrt{1 - \left(\frac{A_2}{A_1}\right)^2}} \sqrt{\frac{2}{\rho} (P_1 - P_2)} \quad (A.5)$$

where

Q_2 Fluid flow through vena contracta $[m^3/s]$

The contraction coefficient is defined as the ratio between the opening area at vena contracta and the orifice $C_c = A_2/A_0$. To account for losses such as viscous friction and deviation from the assumptions behind the Bernoulli Equation an empirical coefficient C_v is applied to obtain a practical orifice equation.

$$Q_2 = \frac{C_v A_2}{\sqrt{1 - \left(\frac{A_2}{A_1}\right)^2}} \sqrt{\frac{2}{\rho} (P_1 - P_2)}$$

$$Q_2 = \frac{C_v C_c A_0}{\sqrt{1 - \left(\frac{C_c A_0}{A_1}\right)^2}} \sqrt{\frac{2}{\rho} (P_1 - P_2)}$$

where

C_v Empirical correction coefficient $[\cdot]$

C_c Contraction coefficient $[\cdot]$

Due to difficulties in determining C_c a unitless discharge coefficient C_d is defined that accounts for all losses.

$$Q_2 = C_d A_0 \sqrt{\frac{2}{\rho} (P_1 - P_2)} \quad (\text{A.6})$$

[Andersen, 2003, p.21-23]

A.2 Euler Lagrange Derivations

The partial derivative within the Euler-Lagrange equation is carried out in the following parts. First the position vector is defined and the time-derivatives taken for the pistons \vec{x}_p and the nut \vec{x}_n .

$$\vec{x}_p = \begin{pmatrix} x_{p,1} \\ x_{p,2} \\ x_{p,3} \\ x_{p,4} \\ x_{p,5} \\ x_{p,6} \end{pmatrix} = r_e \begin{pmatrix} \cos(\theta) \\ \cos\left(\theta - \frac{\pi}{3}\right) \\ \cos\left(\theta - \frac{2\pi}{3}\right) \\ \cos(\theta - \pi) \\ \cos\left(\theta - \frac{4\pi}{3}\right) \\ \cos\left(\theta - \frac{5\pi}{3}\right) \end{pmatrix} + r_e \vec{1} \quad \dot{\vec{x}}_p = -r_e \begin{pmatrix} \sin(\theta) \\ \sin\left(\theta - \frac{\pi}{3}\right) \\ \sin\left(\theta - \frac{2\pi}{3}\right) \\ \sin(\theta - \pi) \\ \sin\left(\theta - \frac{4\pi}{3}\right) \\ \sin\left(\theta - \frac{5\pi}{3}\right) \end{pmatrix} \dot{\theta} \quad (\text{A.7})$$

$$\vec{x}_n = r_e \begin{pmatrix} -\sin(\theta) \\ \cos(\theta) \end{pmatrix} \quad \dot{\vec{x}}_n = -r_e \begin{pmatrix} \cos(\theta) \\ \sin(\theta) \end{pmatrix} \dot{\theta} \quad (\text{A.8})$$

where $\vec{1}$ is a vector in R^6 and $\vec{x}_{p,init} \in R^6$ is the initial conditions of each piston. The kinetic and potential energies of the system is given as:

$$\mathcal{T} = \frac{1}{2}J\dot{\theta}^2 + \frac{1}{2}m_n\dot{\vec{x}}_n^T\dot{\vec{x}}_n + \frac{1}{2}m_p\dot{\vec{x}}_p^T\dot{\vec{x}}_p \quad (\text{A.9})$$

$$\mathcal{V} = \frac{1}{2}k_p\vec{x}_p^T\vec{x}_p + \frac{1}{2}k_p\vec{x}_{p,init}^T\vec{x}_{p,init} + k_p\vec{x}_p^T\vec{x}_{p,init} \quad (\text{A.10})$$

where

J	Moment of inertia of shaft and eccentric mass, $J = 4.49 \cdot 10^{-4}$	$[kgm^2]$
m_n	Mass of nut, $m_n = 0.33$	$[kg]$
m_p	Mass of piston, $m_p = 0.08$	$[kg]$
k_p	Spring constant at piston, $k_p = 5830$	$[N/m]$
x_{p0}	Initial spring displacement, $x_{p0} = 0.0125$	$[m]$
\vec{x}_p	Vector containing the position of each piston	$[m]$
\vec{x}_n	Vector containing x- and y- position of the nut	$[m]$

The Langrangian L is defined as the difference between the kinetic \mathcal{T} and potential \mathcal{V} energies of the system.

$$L = \left(\frac{1}{2}J\dot{\theta}^2 + \frac{1}{2}m_n\dot{\vec{x}}_n^T\dot{\vec{x}}_n + \frac{1}{2}m_p\dot{\vec{x}}_p^T\dot{\vec{x}}_p \right) - \left(\frac{1}{2}k_p\vec{x}_p^T\vec{x}_p + \frac{1}{2}k_p\vec{x}_{p,init}^T\vec{x}_{p,init} + k_p\vec{x}_p^T\vec{x}_{p,init} \right) \quad (\text{A.11})$$

The derivative of the lagrangian w.r.t. the generalized coordinate θ is carried as follows.

$$\begin{aligned} \frac{\partial L}{\partial \theta} &= \frac{\partial}{\partial \theta} \left(\frac{1}{2}m_n\dot{\vec{x}}_n^T\dot{\vec{x}}_n + \frac{1}{2}m_p\dot{\vec{x}}_p^T\dot{\vec{x}}_p - \frac{1}{2}k_p\vec{x}_p^T\vec{x}_p - k_p\vec{x}_p^T\vec{x}_{p,init} \right) \\ &= \frac{\partial}{\partial \theta} \left(\frac{1}{2}m_n r_e^2 \underbrace{(\sin^2(\theta) + \cos^2(\theta))}_{=1} \dot{\theta}^2 + \frac{1}{2}m_p\dot{\vec{x}}_p^T\dot{\vec{x}}_p - \frac{1}{2}k_p\vec{x}_p^T\vec{x}_p - k_p\vec{x}_p^T\vec{x}_{p,init} \right) \\ &= \frac{\partial}{\partial \theta} \left(\frac{1}{2}m_p\dot{\vec{x}}_p^T\dot{\vec{x}}_p - \frac{1}{2}k_p\vec{x}_p^T\vec{x}_p - k_p\vec{x}_p^T\vec{x}_{p,init} \right) \end{aligned} \quad (\text{A.12})$$

An expansion of the three terms results in the following expression when the initial spring displacement $x_{p,init}$ is the same for all pistons.

$$\frac{1}{2}m_p\dot{\vec{x}}_p^T\dot{\vec{x}}_p = \frac{1}{2}m_p r_e^2 \dot{\theta}^2 \left[\sum_{i=1}^6 \sin^2 \left(\theta - \frac{(i-1)\pi}{3} \right) \right] \quad (\text{A.13})$$

$$\begin{aligned} \frac{1}{2}k_p\vec{x}_p^T\vec{x}_p &= \frac{1}{2}k_p r_e^2 \left[\sum_{i=1}^6 \cos^2 \left(\theta - \frac{(i-1)\pi}{3} \right) \right] + \frac{6}{2}k_p r_e^2 \\ &\quad + k_p r_e^2 \left[\sum_{i=1}^6 \cos \left(\theta - \frac{(i-1)\pi}{3} \right) \right] \end{aligned} \quad (\text{A.14})$$

$$k_p\vec{x}_p^T\vec{x}_{p,init} = k_p r_e x_{p,init} \left[\sum_{i=1}^6 \cos \left(\theta - \frac{(i-1)\pi}{3} \right) \right] + 6k_p r_e x_{p,init} \quad (\text{A.15})$$

Taking the derivative of the expanded terms yields the following.

$$\frac{\partial}{\partial \theta} \left(\frac{1}{2} m_p \dot{\vec{x}}_p^T \dot{\vec{x}}_p \right) = m_p r_e^2 \dot{\theta}^2 \left[\sum_{i=1}^6 \sin \left(\theta - \frac{(i-1)\pi}{3} \right) \cos \left(\theta - \frac{(i-1)\pi}{3} \right) \right] \quad (\text{A.16})$$

$$\begin{aligned} \frac{\partial}{\partial \theta} \left(\frac{1}{2} k_p \vec{x}_p^T \vec{x}_p \right) &= -k_p r_e^2 \left[\sum_{i=1}^6 \sin \left(\theta - \frac{(i-1)\pi}{3} \right) \cos \left(\theta - \frac{(i-1)\pi}{3} \right) \right] \\ &\quad - k_p r_e^2 \left[\sum_{i=1}^6 \sin \left(\theta - \frac{(i-1)\pi}{3} \right) \right] \end{aligned} \quad (\text{A.17})$$

$$\frac{\partial}{\partial \theta} (k_p \vec{x}_p^T \vec{x}_{p,init}) = -k_p r_e x_{p,init} \left[\sum_{i=1}^6 \sin \left(\theta - \frac{(i-1)\pi}{3} \right) \right] \quad (\text{A.18})$$

Collecting all the terms yields the final result of the derivative w.r.t the generalized coordinate.

$$\begin{aligned} \frac{\partial L}{\partial \theta} &= m_p r_e^2 \dot{\theta}^2 \left[\sum_{i=1}^6 \sin \left(\theta - \frac{(i-1)\pi}{3} \right) \cos \left(\theta - \frac{(i-1)\pi}{3} \right) \right] \\ &\quad - k_p r_e^2 \left[\sum_{i=1}^6 \sin \left(\theta - \frac{(i-1)\pi}{3} \right) \cos \left(\theta - \frac{(i-1)\pi}{3} \right) \right] \\ &\quad - k_p r_e^2 \left[\sum_{i=1}^6 \sin \left(\theta - \frac{(i-1)\pi}{3} \right) \right] \\ &\quad - k_p r_e x_{p,init} \left[\sum_{i=1}^6 \sin \left(\theta - \frac{(i-1)\pi}{3} \right) \right] \end{aligned} \quad (\text{A.19})$$

The derivative of the lagrangian w.r.t. the time-derived generalized coordinate $\dot{\theta}$ is carried in the following maner.

$$\begin{aligned} \frac{\partial L}{\partial \dot{\theta}} &= \frac{\partial}{\partial \dot{\theta}} \left(\frac{1}{2} J \dot{\theta}^2 + \frac{1}{2} m_n \dot{\vec{x}}_n^T \dot{\vec{x}}_n + \frac{1}{2} m_p \dot{\vec{x}}_p^T \dot{\vec{x}}_p \right) \\ &= \frac{\partial}{\partial \dot{\theta}} \left(\frac{1}{2} J \dot{\theta}^2 + \frac{1}{2} m_n r_e^2 \underbrace{(\sin^2(\theta) + \cos^2(\theta))}_{=1} \dot{\theta}^2 + \frac{1}{2} m_p \dot{\vec{x}}_p^T \dot{\vec{x}}_p \right) \\ &= J \dot{\theta} + m_n r_e^2 \dot{\theta} + m_p r_e^2 \left[\sum_{i=1}^6 \sin^2 \left(\theta - \frac{(i-1)\pi}{3} \right) \right] \dot{\theta} \end{aligned} \quad (\text{A.20})$$

The time derivative becomes

$$\frac{d}{dt} \left(\frac{\partial L}{\partial \dot{\theta}} \right) = J \ddot{\theta} + m_n r_e^2 \ddot{\theta} + m_p r_e^2 \left[\sum_{i=1}^6 \sin^2 \left(\theta - \frac{(i-1)\pi}{3} \right) \right] \ddot{\theta} \quad (\text{A.21})$$

A.3 Fluid viscosity

The used oil is a Shell Tellus Oil 46. It complies with the ISO VG 46 standard. The kinematic viscosity for a number of different temperatures is determined from figure A.3. The kinematic ν and dynamic viscosity μ relates through the following equation:

$$\mu = \nu \cdot \rho \tag{A.22}$$

The density of the oil at the specified temperatures is needed in order to find the dynamic viscosity. The data is collected in table A.1.

Temperature [°]	Kinematic viscosity ν	Oil density [kg/m^3]	Dynamic viscosity [$Pa \cdot s$]
10	300	910.86	0.2733
20	145	849.25	0.1231
40	46	748.07	0.0344
44	40	730.65	0.0292
60	22	668.42	0.0147
80	11	604.11	0.0066

Table A.1: Kinematic viscosity data for a typical ISO VG 46 mineral oil and density estimations for Shell Tellus Oil 46 at different temperatures.

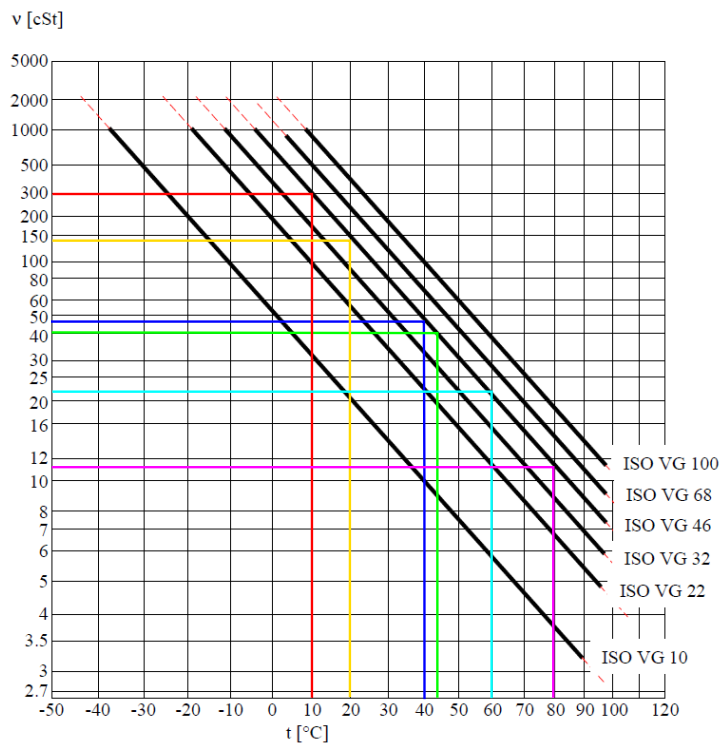


Figure A.3: Viscosity-temperature plot for mineral oils that comply with different ISO VG standards [Andersen, 2003, Chap.2]

A.4 Oil parameter variation

The variation in oil parameters in the range $T \in [0 : 100]^{\circ}\text{C}$ and $P \in [1 : 400]\text{Bar}$ is calculated by use of the models given in the report. The change in oil viscosity, oil stiffness and oil density is given in figure A.4a, A.4b and A.5.

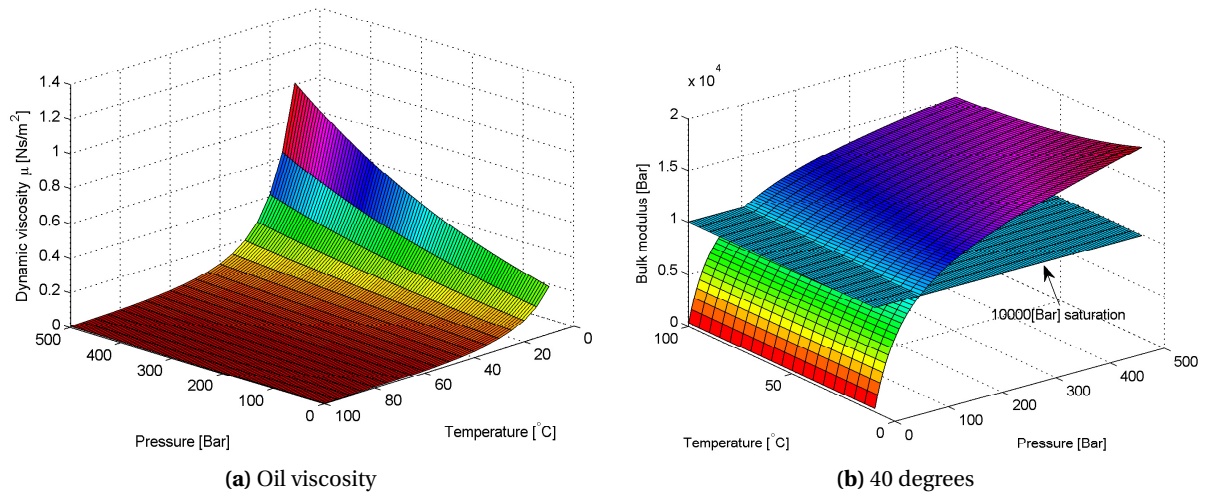


Figure A.4: (a) Oil viscosity as a function of pressure and temperature, (b) Oil stiffness (bulk modulus) as a function of pressure and temperature

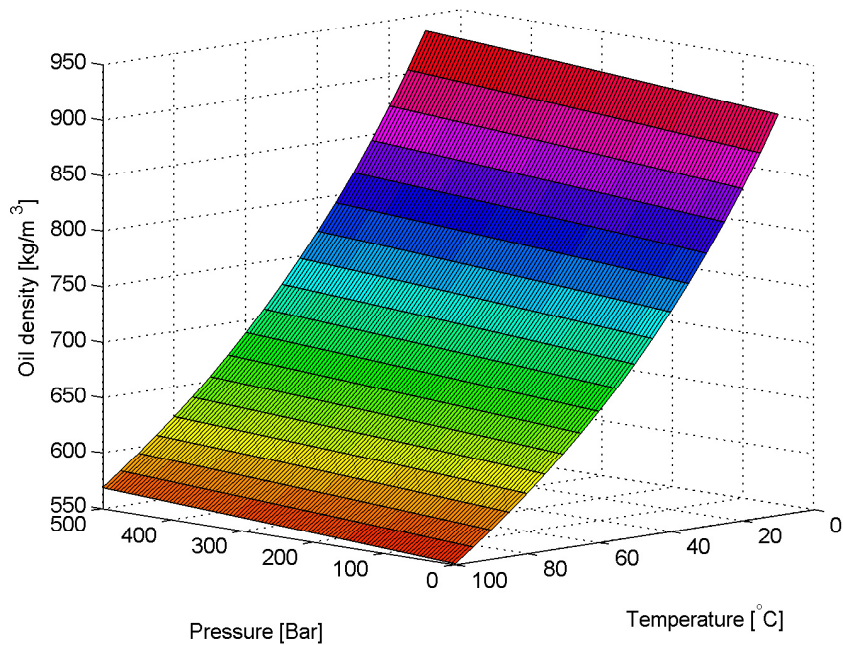


Figure A.5: Oil density as a function of pressure and temperature

A.5 Optimal coefficients for the vogel equation

The optimal coefficient values for the vogel equation is solved using an optimisation problem. The problem is defined as

$$\underset{K_{vo,a}, K_{vo,b}, K_{vo,c} \in \mathbb{R}}{\operatorname{argmin}} C(K_{vo,a}, K_{vo,b}, K_{vo,c}) \quad (\text{A.23})$$

where

$$C = (\mu_{0,1} - \mu_0(T_1))^2 \cdot s_1^2 + \dots + (\mu_{0,5} - \mu_0(T_5))^2 \cdot s_3^2 \quad (\text{A.24})$$

The values $(\mu_{0,i}, T_i)$ for $i \in \{1, 2, 3, 4, 5, 6\}$ consists of datapoints obtained from figure A.3. The scaling coefficients s_i normalises the coefficients so each term is equally weighted. In practice, this is achieved by finding the maximum viscosity reading. Let this be $\mu_{0,1}$ without loss of generality. The scaling coefficients are then determined by

$$s_i = \frac{\mu_{0,1}}{\mu_{0,i}} \quad (\text{A.25})$$

The problem is solved in MATLAB using the simplex method and the obtained values are

$$\begin{aligned} K_{vo,a} &= 0.000020096463 & [kg/(m \cdot s)] \\ K_{vo,b} &= 1050.325917381536 & [K] \\ K_{vo,c} &= 172.732548744080 & [K] \end{aligned}$$

Filters and Controllers



B.1 Filters

A derivation of the filter used in this report is given below. The moving average filter is derived in the report as it only contains a number of samples. The first order low pass filter and the second order butterworth filter is given below.

First order low pas filter

$$H_{f,1}(z) = \frac{\omega_c}{\frac{2}{T} \frac{z-1}{z+1} + \omega_c} \Big|_{s=\frac{2}{T} \frac{z-1}{z+1}} \quad (\text{B.1})$$

$$= \frac{\omega_c(z+1)}{\frac{2}{T}(z-1) + \omega_c(z+1)} \quad (\text{B.2})$$

$$= \frac{\omega_c(z+1)}{z\left(\frac{2}{T} + \omega_c\right) + \left(\omega_c - \frac{2}{T}\right)} \quad (\text{B.3})$$

$$= \frac{0.00469Z^{-1} + 0.00469}{z^{-1} - 0.9906} \quad (\text{B.4})$$

Second order butterworth filter

$$H_{f,2}(z) = \frac{\omega_c^2}{s + 2\sqrt{0.5}\omega_c s + \omega_c^2} \Big|_{s=\frac{2}{T} \frac{z-1}{z+1}} \quad (\text{B.5})$$

$$= \frac{\omega_c^2}{\left(\frac{2}{T} \frac{z-1}{z+1}\right)^2 + 2\sqrt{0.5}\omega_c \left(\frac{2}{T} \frac{z-1}{z+1}\right) + \omega_c^2} \quad (\text{B.6})$$

$$= \frac{\omega_c^2 \left(\frac{T}{2}(z+1)\right)^2}{(z-1)^2 + 2\sqrt{0.5}\omega_c \left(\frac{2}{T} \frac{z-1}{z+1}\right) \cdot \left(\frac{T}{2}(z+1)\right)^2 + \omega_c^2 \cdot \left(\frac{T}{2}(z+1)\right)^2} \quad (\text{B.7})$$

$$= \frac{\left(\frac{\omega_c \cdot T}{2}\right)^2 (z^2 + 2z + 1)}{(z^2 - 2z + 1) + \frac{2\sqrt{0.5}\omega_c T}{2} (z^2 - 1) + \left(\frac{\omega_c \cdot T}{2}\right)^2 \cdot (z^2 + 2z + 1)} \quad (\text{B.8})$$

$$H_{f,2}(z) = \frac{\left(\frac{\omega_c \cdot T}{2}\right)^2 (z^2 + 2z + 1)}{z^2 \left(1 + \frac{2\sqrt{0.5}\omega_c T}{2} + \left(\frac{\omega_c \cdot T}{2}\right)^2\right) + z \left(-2 + \frac{(\omega_c \cdot T)^2}{2}\right) + \left(1 - \frac{2\sqrt{0.5}\omega_c T}{2} + \left(\frac{\omega_c \cdot T}{2}\right)^2\right)} \quad (\text{B.9})$$

$$= \frac{6.1 \cdot 10^{-5} z^{-2} + 0.000122 z^{-1} + 6.1 \cdot 10^{-5}}{z^{-2} - 1.978 z^{-1} + 0.978} \quad (\text{B.10})$$

B.1.1 Flow estimator response for deviation in numerical differentiation

A deviation of 20% is assumed and the results for under estimating is given in figure B.1a and over estimating in figure B.1b.

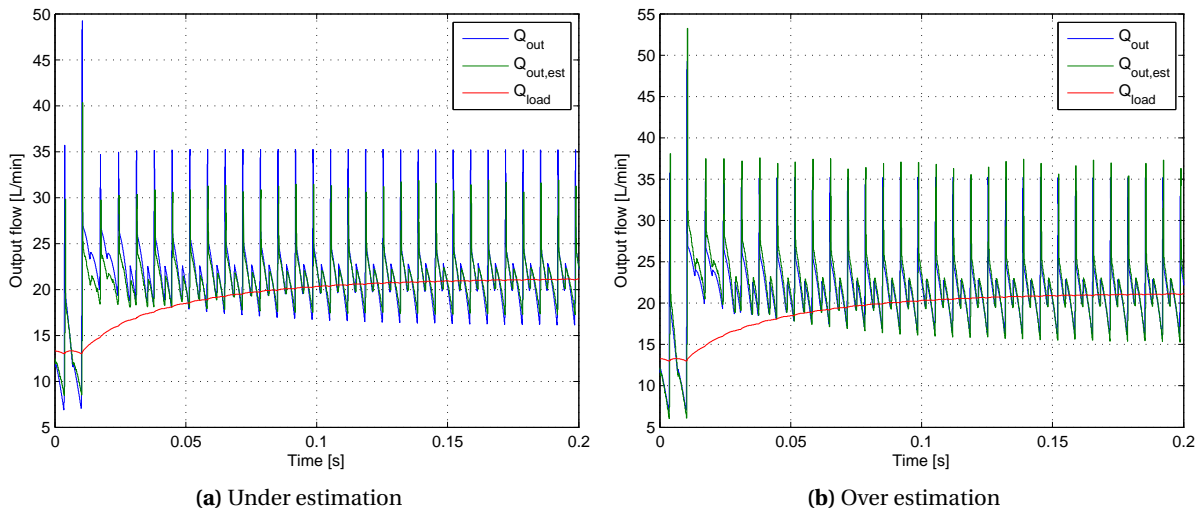


Figure B.1: Flow estimators sensitivity towards the (a) under estimation and (b) over estimation of the numerical differentiation of the load pressure of by 20%

Again, the estimator performs very well with a $MSE = 7.3342$ for under estimation and a $MSE = 10.0634$ for over estimation.

B.2 Controllers

B.2.1 Smith predictor

Derivation of closed loop transfer function including inner and outler loop excluding a feedforward gain is derived to be

$$H_{cl}(z) = \frac{Q_{out}(z)}{Q_{out,d}(z)} = \frac{H_{cl,i}(z) \cdot H_p(z) \cdot z^{-k}}{1 + H_{cl,i}(z) \cdot z^{-k} \cdot H_p(z)} \quad (\text{B.11})$$

$$= \frac{\frac{H_c(z)}{1 + H_c(z) \hat{H}_p(z)(1 - z^{-k})} \cdot H_p(z) \cdot z^{-k}}{1 + \frac{H_c(z)}{1 + H_c(z) \hat{H}_p(z)(1 - z^{-k})} \cdot H_p(z) \cdot z^{-k}} \quad (\text{B.12})$$

$$= \frac{H_c(z) \cdot H_p(z) \cdot z^{-k}}{1 + H_c(z) \hat{H}_p(z)(1 - z^{-k}) + H_c(z) \cdot H_p(z) \cdot z^{-k}} \quad (\text{B.13})$$

$$= \frac{H_c(z) \cdot H_p(z) \cdot z^{-k}}{1 + H_c(z) \hat{H}_p(z) + H_c(z) \cdot (H_p(z) \cdot z^{-k} - \hat{H}_p(z) \cdot z^{-k})} \quad (\text{B.14})$$

$$= \frac{H_c(z) \cdot H_p(z) \cdot z^{-k}}{1 + H_c(z) \hat{H}_p(z)} \quad (\text{B.15})$$

DDP Flow Response



The output flow response from the DDP given input signals $\theta_{cl} \in [160 : 280]$ for load pressure variation at $P_{load} \in [50Bar : 500Bar]$ and oil temperature variation of $T \in [15^\circ : 70^\circ]$ is showed in figure C.1

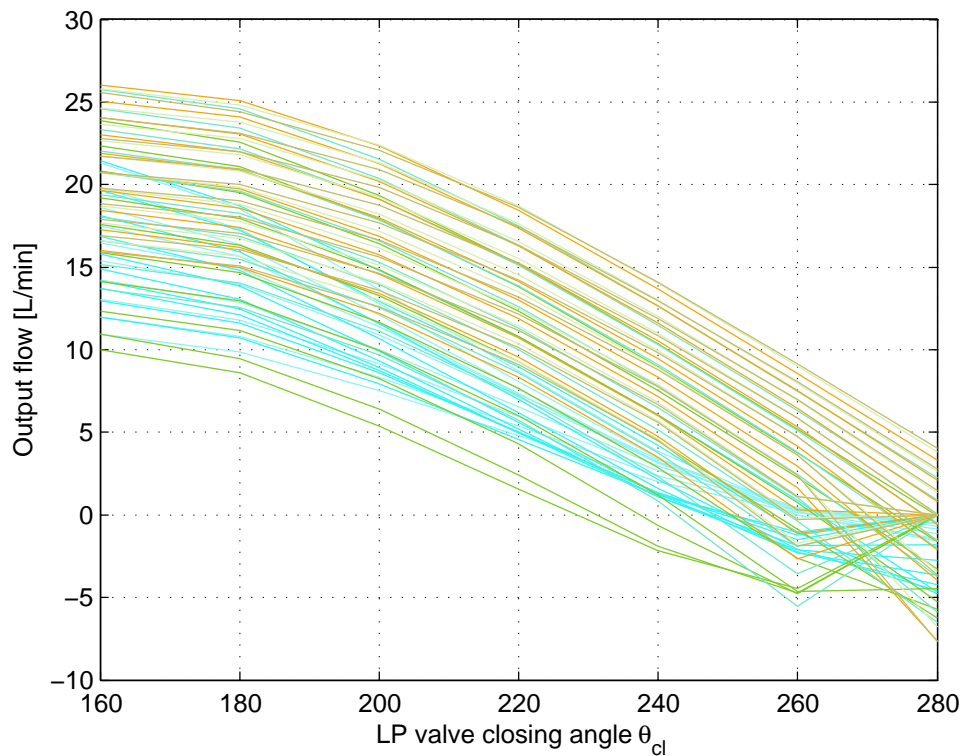


Figure C.1: Output flow as a function of the closing angle from 6 cylinders given different operation conditions.

When the temperature is fixed at $T = 30^\circ$ the flow response given the input signals $\theta_{cl} \in [160 : 280]$ for load pressure variation at $P_{load} \in [50Bar : 500Bar]$ is showed in figure C.2

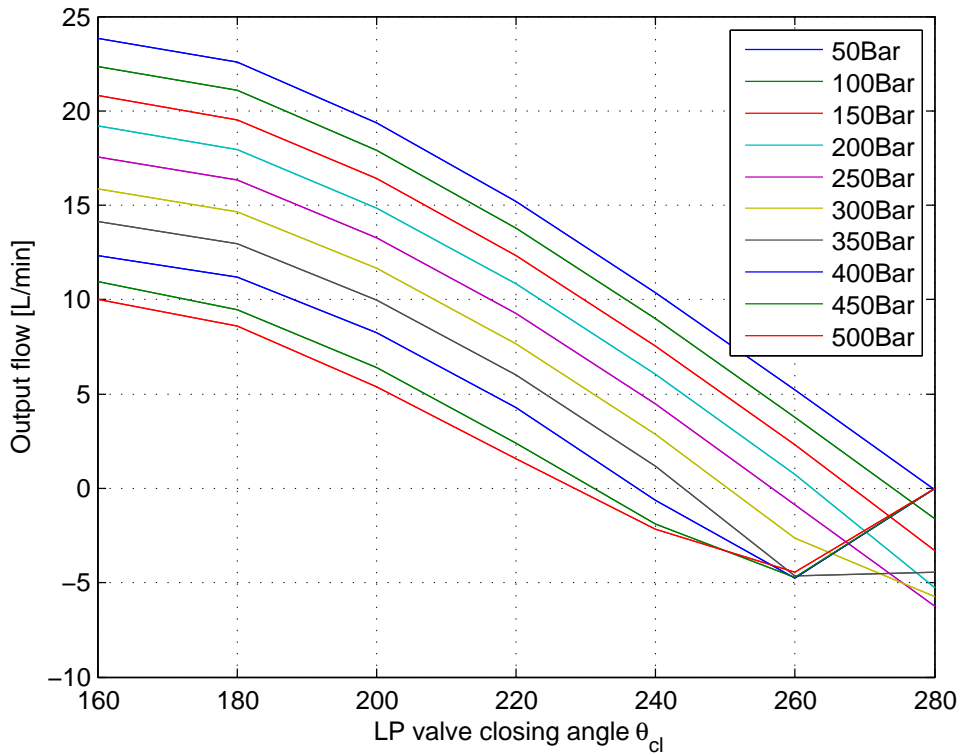


Figure C.2: Output flow as a function of the closing angle from 6 cylinders given different operation conditions for fixed oil temperature at $T=30$.

C.1 Maximum flow rate

The maximum output flow rate is a function of the load pressure and $\theta_{cl} = 160^\circ$. The relation is approximately linear as seen in figure C.3 and the linear fit is

$$\bar{Q}_{out,max} = -0.031975 \cdot P_{load} + 25.06 \quad (C.1)$$

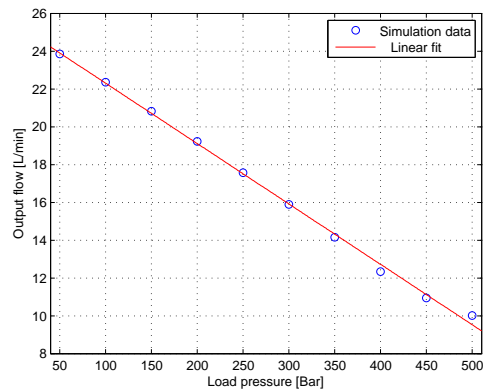


Figure C.3: Linear approximation of data obtained from simulation that shows \bar{Q}_{out} as a function of P_{load} for $\theta_{cl} = 160^\circ$

C.2 Simplified pump response

Reducing the orifice size so that $Q_{nom} = 20[L/min]$ and $P_{nom} = 200[Bar]$ does not alter the response drastically, see figure C.4.

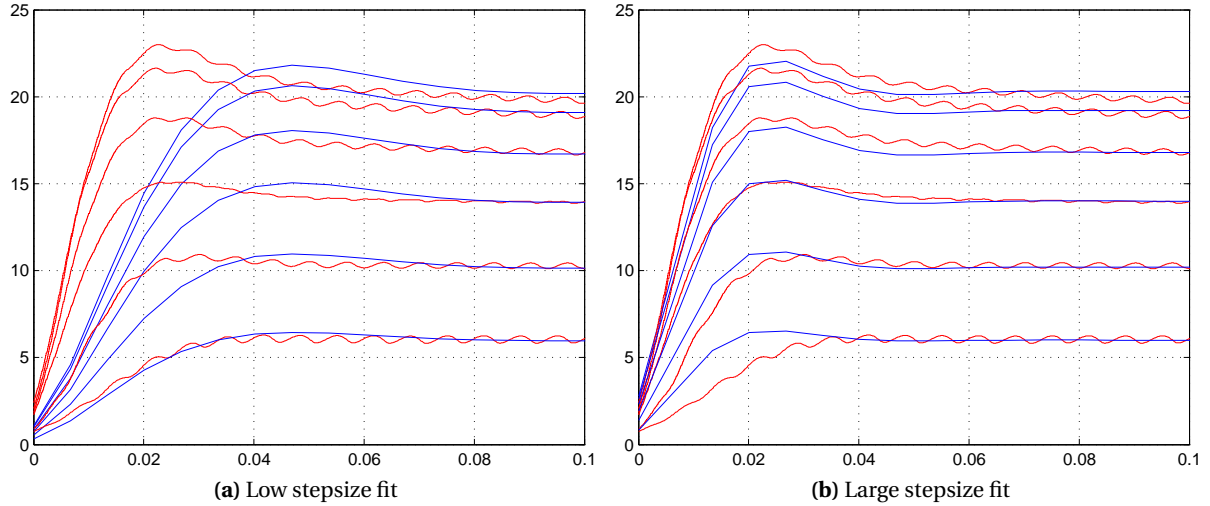


Figure C.4: Simplified pump flow response and nonlinear pump flow response with $Q_{nom} = 20[L/min]$ and $P_{nom} = 200[Bar]$.

It is observed that the response deviates largely for different step sizes. The transfer function that is accurate for large step sizes is chosen because the gain of the system is large in this case. If the designed controller is stable for large gain, it will also be stable for small gain systems.

The simplified pump model is based on a standard second order system

$$G_p(s) = \frac{\omega_n^2}{s^2 + 2 \cdot \zeta \cdot \omega_n \cdot s + \omega_n^2} \quad (C.2)$$

where the damping factor $\zeta = 0.65$ and natural frequency $\omega_n = 82[rad/s]$ for the low step size. For the large stepsize $\zeta = 0.65$ and $\omega_n = 153[rad/s]$.

Bibliography

- T. O. Andersen. *Fluid Power Systems - Modelling and Analysis*. Institute of Energy Technology, Aalborg University, 2. edition, 2003.
- T. O. Andersen and M. R. Hansen. *Fluid Power Circuits - System Design and Analysis*. Aalborg University, 2007.
- B. S. Armstrong and Q. Yuan. Multi-level control of hydraulic gerotor motors and pumps. page 8, 2006.
- .Artemis Intelligent Power LTD. URL <http://www.artemisip.com/>.
- M. Ehsan, W. H. S. Rampen, and S. H. Salter. Modelling of digital-displacement pump motors and their application as hydraulic drives for nonuniform loads. *Project B3 - Power Take-off Systems*, vol. 122, no. 1:p. 210–215, 2000.
- R. W. Fox, P. J. Pritchard, and A. T. McDonald. *Introduction to Fluid Mechanics*. John Wiley & Sons, 7. edition, 2010. ISBN: 9780471742999.
- N. Gilani. Hydraulic fluid classifications. *eHow*. URL http://www.ehow.com/list_6298949_hydraulic-fluid-classifications.html.
- M. Heikkilä, J. Tammisto, M. Huova, K. Huhtala, and M. Linjama. Experimental evaluation of a piston-type digital pump-motor-transformer with two independent outlets. *Fluid Power and Motion Control (FPMC 2010)*, pages p. 83–97, September 2010.
- P. Johansen and D. B. Rømer. Design of a high efficiency valve for use in a digital displacement hydraulic pump. *Aalborg University*, 2011.
- Kistler. Quartz high-pressure sensor type 601a,601h. *Kistler*, 2010.
- D. Knezevic and V. Savic. Mathematical modeling of changing of dynamic viscosity, as a function of temperature and pressure, of mineral oils for hydraulic systems. *FACTA UNIVERSITATIS, Series: Mechanical Engineering*, vol.4 no.1:27–34, April 2006.

V. Massimiliano. Performance improvement of smith predictor through automatic computation of dead time. 2003.

B. R. Munson, D. F. Young, T. H. Okiishi, and W. W. Huebsch. *Fundamentals of Fluid Mechanics : Internatioal Student Version*. John Wiley & Sons, 6. edition, 2010. ISBN: 9780470398814.

NewScientist. Technology innovation / power. winner: Artemis intelligent power. December 2009.
URL <http://www.newscientist.com/art/cleantechrevolution/view?id=dn18284>.

Parker. Messen, steuern, regeln und automatisieren. *Katalog 4083-2/DE*, 2006.

C. L. Phillips and R. D. Harbor. *Feedback Control Systems*. 4th edition, 2000.

Shell. Shell tellus oil 46 - material safety data sheet. 2008.

J.-M. Valin and I. B. Collings. Interference-normalized least mean square algorithm. *IEEE*, 2007.